UNIVERSITÀ
DEGLI STUDI
DI PADOVA

TESI DI DOTTORATO DI RICERCA IN FISICA

Università degli Studi di Padova

Dipartimento di Fisica e Astronomia

SCUOLA DI DOTTORATO IN FISICA
INDIRIZZO COMUNE
CICLO XXXI

Plasmonic Nanostructures for Biosensing Applications

Vice coordinatore della Scuola: Ch.ma Prof. Cinzia SADA
Supervisore: Ch.mo Prof. Giovanni MATTEI

Dottorando: Ionuț Gabriel BALAȘA

To Illi and my family

Life does not conclude. And life knows nothing of names. This tree, tremulous pulse of new leaves. I am this tree. Tree, cloud; tomorrow book or wind: the book I read, the wind I drink. All outside, wandering.

Vitangelo Moscarda in One, No One and One Hundred Thousand, L. Pirandello

La vita non conclude. E non sa di nomi, la vita. Quest'albero, respiro tremulo di foglie nuove. Sono quest'albero. Albero, nuvola, domani libro o vento: il libro che leggo, il vento che bevo. Tutto fuori, vagabondo.

Vitangelo Moscarda in Uno, nessuno e centomila, L. Pirandello

Abstract

The aim of this work is the study, the design and the nanofabrication of innovative plasmonic nanostructured materials to develop label-free optical biosensors. Noble metal-based nanostructures have gained interest in the last years due to their extraordinary optical properties, which allow to develop optical biosensors able to detect very low concentrations of specific biomolecules, called analyte, down to the picomolar range. Such biosensors rely on the Surface Plasmon Resonance (SPR) excitation which occurs under specific conditions that depend both on the morphology of the nanostructure and on the adjacent dielectric medium. Therefore, the binding of the biomolecules to metal surfaces is revealed as a change in the SPR condition. Four kinds of nanostructures are investigated in this work: ordered and disordered nanohole array (o-NHA, d-NHA), nanoprism array (NPA) and nanodisk array (NDA). The o-NHA and d-NHA consist of a thin metallic film (50 - 100 nm) patterned with, respectively, a hexagonal and a disordered array of circular holes. The NPA consists of a honeycomb lattice of triangle shaped nanoprisms with edges of about 100 - 200 nm and height of 40 - 80 nm. Finally, the NDA consists of a disordered array of non-interacting disks with 100 - 300 nm diameter and 40 - 80 nm height. The first two support the Extended-SPR whereas the last two, due to their three-dimensional confinement, present Localized-SPR property. Two colloidal techniques are employed for the scalable and cost-effective synthesis of wide areas of nanostructures that allow a fine control of the morphology: NanoSphere Lithography (NSL) and Sparse Colloidal Lithography (SCL). Ordered arrays were nanofabricated by NSL (i.e., NPA and o-NHA) whereas disordered nanostructures were synthesized by the SCL (i.e., NDA and d-NHA). Firstly, the nanostructures are simulated by Finite Element Method (FEM) computations and their performances in revealing small variations of the dielectric medium at the interface is evaluated as a function of their geometrical parameters. Simulated local sensitivities range from 3.1 nm/RIU of the o-NHA up to 13.6 nm/RIU of the NPA. Afterwards, the sensing performances are evaluated experimentally with nanofabricated samples and comparable but slightly smaller sensitivities are obtained. Secondly, a proof-of-concept protocol for the detection assay, that relies on the binding of streptavidin protein to the biotinylated gold surfaces, is exploited to test the nanostructures as biosensors. A 4.4 nM limit of detection is reached with the best performing biosensor (NPA) and picomolar ones are expected for NPA and NDA with a suitable improvement of the functionalization protocol. Finally, complementary single stranded RNA molecules were used, respectively, as bioreceptor and analyte. Revealing short sequences of non-coding RNA, called microRNA, is fundamental for the medical research since these oligonucleotides act as biomarkers for specific diseases, like tumors. Signals of about 13 nm are obtained from the binding of bioreceptor to the nanostructure and from the hybridization of the analyte oligonucleotide at saturation concentrations ($\sim 1\,\mu$M), indicating that for the moment the developed protocol is quite effective down to the 100 nM range. Of course, for reading the nm or even sub-nM range further optimizations are needed.

Estratto

Lo scopo di questo lavoro è lo studio, il design e la nanofabricazione di nanomateriali plasmonici innovativi per sviluppare biosensori ottici label-free. L'interesse nei confronti delle nanostrutture basate su metalli nobili è aumentato recentemente grazie alle loro straordinarie proprietà ottiche che permettono di sviluppare biosensori ottici capaci di rilevare concentrazioni molto basse, fino al picomolare, di biomolecole specifiche, dette analita. Tali biosensori si basano sull'eccitazione della Risonanza Plasmonica di Superficie (SPR), che si attiva sotto specifiche condizioni che dipendono sia dalla morfologia della nanostruttura che dal mezzo dielettrico adiacente. Dunque, l'aggancio di biomolecole sulla superficie metallica è rivelata in quanto cambio della condizione di risonanza. In questo lavoro vengono studiate quattro tipogie di nanostrutture: nanohole array ordinati e disordinati (o-NHA, d-NHA), nanoprism array (NPA) e nanodisk array (NDA). I NHA consistono in un sottile film metallico (50 - 100 nm) con un insieme, rispettivamente, ordinato e disordinato di fori nanometrici circolari. I NPA consistono in un insieme di nanoprismi triangolari distribuiti a nido d'api con lato tra 100 - 200 nm e altezza tra 40 - 80 nm. Infine, i NDA rappresentano un insieme disordinato di nanodischi non interagenti con diametri tra 100 - 300 nm e altezza tra 40 - 80 nm. Le prime due nanostrutture presentano la risonanza plasmonica estesa mentre, le ultime due, grazie al loro confinamento nelle tre dimensioni, mostrano la risonanza plasmonica localizzata. Due tecniche colloidali sono impiegate per la sintesi a basso costo di ampie aree di nanostrutture con la possibilità di controllare finemente la morfologia: la NanoSphere Lithography (NSL) e la Sparse Colloidal Lithography (SCL). Con la prima, sono stati fabbricati le nanostrutture ordinate (NPA e o-NHA) mentre per quelle disordinate (NDA e d-NHA) è stata sfruttata la SCL. In primo luogo, le nanostrutture sono simulate mediante metodi computazionali agli elementi finiti (FEM) e vengono valutate le loro prestazioni nel rivelare minimi cambiamenti del mezzo dielettrico all'intefaccia in funzione e dei loro parametri geometrici. Si stimano sensibilità locali da 3.1 nm/RIU del o-NHA fino a 13.6 nm/RIU del NPA. In seguito, tali prestazioni vengono valutate anche mediante misure sperimentali con le nanostrutture sintetizzate e si ottengono risultati confrontabili ma leggermente inferiori. In secodo luogo, un protocollo standard viene sfruttato per testare le nanostrutture come biosensori e si basa sul legame della streptavidina con le superfici d'oro biotinilate. Impiegando la nanostruttura più performante, NPA, si raggiunge un limite di rivelabilità di 4.4 nM, ma sensibilità nel picomolare si potrebbero raggiungere perfezionando opportunatamente in protocollo di funzionalizzazione. Infine, vengono impiegati come, rispettivamente, recettore e analita le sequenze complementari di molecole di RNA. La possibilità di rivelare sequenze corte di RNA non codificanti è fondamentale per la ricerca medica poiché tali oligonucleotidi possono essere dei biomarker per certe malatie, tra cui tumori. Segnali attorno a 13 nm si ottengono sia dal legame del recettore con la nanostruttura che dall'ibridizzazione del oligonucleotide analita a concentrazioni di saturazione ($\sim 1\,\mu$M), indicando che il protocollo sviluppato sinora è efficace fino a concentrazioni dell'ordine dei 100 nM. Per rivelare cocentrazioni dell'ordine del nM o anche sub-nM sono necessarie ulteriori ottimizzazioni.

Contents

List of Acronyms

11-MUA 11-Mercaptoundecanoic Acid

1-OCT 1-Octanethiol

ACH Aluminum Chlorohydrate

AFM Atomic Force Microscope

ATR Attenuated Total Reflectance

BSA Bovine Serum Albumine

d-NHA disordered NanoHole Array

EBL Electron Beam Lithography

EDC 1-Ethyl-3-[3-Dimethylaminopropyl]Carbodiimide hydrochloride

EOT extraordinary optical transmission

E-SP Extended Surface Plasmons

ESPR Extended Surface Plasmon Resonance

FDFD Finite Difference Frequency Domain

FDTD Finite Difference Time Domain

FEM Finite Elements Method

FET Field-Effect Transistor

FIB Focused Ion Beam

HCL Hole-mask Colloidal Lithography

LoD limit of detection

L-SP Localized Surface Plasmons

LSPR Localized Surface Plasmon Resonance

MES 2-(N-Morpholino)EthaneSulfonic acid sodium salt

m-PEG Methoxy-PEG$_n$-Silane

miRNA microRNA

MW molecular weight

NDA NanoDisk Array

NHA NanoHole Array

NPA NanoPrisms Array

NSL Nanosphere Lithography

o-NHA ordered NanoHole Array

PBS Phosphate Buffered Saline

PDDA Poly(diallyldimethylammonium chloride)

PDMS Polydimethylsiloxane

PEG Polyethylene Glycol

PMMA Poly(methyl methacrylate)

PS polystyrene

PSS Poly(sodium 4-styrenesulfonate)

QCM Quartz Crystal Microbalance

RDF Radial Distribution Function

RIE Reactive Ion Etching

RSA Random Sequential Adsorption

SA streptavidin

SAM self assembled monolayer

SCL Sparse Colloidal Lithography

SDS Sodium dodecyl sulfate

SEM Scanning Electron Microscopy

SERS Surface Enhancement Raman Spectroscopy

SHCL Shrinking-Hole Colloidal Lithography

SiNW Silicon NanoWire

SLG Soda Lime Glass

SNSA Semi-NanoShell Array

SP Surface Plasmon

SPP Surface Plasmon Polaritons

SPR Surface Plasmon Resonance

SSC Saline Sodium Citrate

ssDNA single-stranded DNA

TCO Transparent Conducting Oxides

TWEEN PEG(20)sorbitan monolaurate

List of Figures

List of Tables

Introduction

In the last years, the study of the size-dependent properties of materials at nanometric scale gained a lot of interest due to the innovative properties that they present such as optical, magnetic, catalytic and mechanical properties. The research on nanomaterials and their properties became important in many sectors such as nanophotonics, data-storage [5] and telecommunication. These areas of interest needed smaller, faster and more efficient devices and such requests were fullfiled by the nanomaterials research [6].

Photonics is the discipline that studies the production, propagation and detection of electromagnetic radiation in the NIR-Vis-NUV range, while nanophotonics focuses on the behaviour and the interaction of the radiation at nanometric scale. In this framework, one of its most active fields is plasmonics, which studies the interaction of electromagnetic radiation with nanostructures, mainly made of noble metals, in order to control the light on scales below the $\lambda/2$ diffraction limit.

Thanks to their extraordinary optical properties, nanomaterials gained interest also in medical applications in the last decade. Medical research and healthcare need innovative devices in the diagnostic field that allow to reveal very low concentrations of a specific compound, called analyte. For this purpose, nanomaterials are very promising for the development of optical biosensors that are able to reveal concentrations down to the pico-molar range [7, 8].

Plasmonics research focuses on the study of the optical properties by varying dimensions, morphology and composition of nanostructures in order to obtain the best performances in the biosensing field. Indeed, the design and the nanofabrication of different nanostructures and the biosensing experiments represent the main purpose of the present work.

The physical phenomenon that gives peculiar optical properties to noble-metal nanostructures is the excitation of Surface Plasmons. They consist in a collective disturbance of the surface free electrons that can exist at the interface between two materials whose real parts of the dielectric function have opposite sign ($\epsilon_1 \cdot \epsilon_2 < 0$, e.g., a dielectric and a metal). The Surface Plasmon (SP) involves on one side the coherent oscillation of the conduction electrons at the interface inside the metal, and on the other side an evanescent electromagnetic wave inside the dielectric [9].

The conditions under which the excitation of a SP occurs determine the Surface Plasmon Resonance (SPR) phenomenon and this is strongly influenced by the shape, size, material composition and local environment. In particular, the transduction mechanism for developing a biosensor device relies precisely on the dependence of the SPR condition on the dielectric environment adjacent to the metal. The binding of an analyte with previously deposited suitable molecular receptors on the nanostructure is revealed as a change in the SPR condition due to the different dielectric properties of the environment (air or water) and the biological compound, which can be considered as a few nanometers thick dielectric layer on the plasmonic nanostructures.

There are two kinds of SP phenomena, the Localized Surface Plasmons (L-SP) and the Extended Surface Plasmons (E-SP). The first is typical of the three-dimensionally confined nanostructures such as nanospheres, nanoprisms, nanodisk, nanorods and can be directly excited by light in the Vis-NIR range [7]. The second one is supported by nanostructures which are confined at nanoscale in one or two dimensions, such as films, one

or two dimensional nanogratings and nanohole arrays [8]. The Localized Surface Plasmon Resonance (LSPR) occurs when the plasmonic coupling condition is fulfilled in the first case whereas the Extended Surface Plasmon Resonance (ESPR) determines the plasmonic coupling in the second case.

Both categories of plasmonic nanomaterials can be employed for biosensing due to the dependance of the coupling condition on the local dielectric environment. Proper functionalization steps have to be performed in order to graft bioreceptor molecules to the nanomaterial, and thus to transform a plasmonic nanostructure into a biosensor. The presence of receptors that bind only to the selected analyte provides a high-specificity. Moreover, the enhanced sensitivity due to the plasmonic resonance can add a further advantage, the lable-free biosensing, that consists in detecting an analyte without binding it with a fluorescent dye. Furthermore, a nanomaterial-based biosensing platform may take advantage of the integration of the sensor with microfluidics thus allowing the lab-on-chip development [10].

There are different strategies for manufacturing a nanomaterial. On one side Electron Beam Lithography (EBL) and Focused Ion Beam (FIB) top-down techniques allow to directly design arbitrarly shaped nanostructures of dimensions below 10nm [11]. However, these lithography techniques are expensive and provide a low throughput. On the other side, colloidal lithographies provide an innovative, cost-effective and high throughput alternative to synthesize a nanomaterial [12].

In the present work two different colloidal techniques, that rely on the assembling of polystyrene (PS) nanospheres as deposition mask, are employed for developing different plasmonic nanostructures with a cost-effective nanopatterning of wide areas and fine tuning of the morphology of the nanostructures: Nanosphere Lithography (NSL) and Sparse Colloidal Lithography (SCL). On one hand, NSL is based on the self assembling of uncharged PS nanospheres in a close-packed hexagonal monolayer [13, 14] and it allows to synthesize ordered arrays of nanostructures. On the other hand, SCL is based on the self assembling of charged PS nanospheres in a disordered pattern, and thus disordered arrays of nanostructures can be synthesized [15, 16].

By combining the self-assembling of the PS nanospheres with metal deposition and dry etching techniques, four different nanostructures are designed and synthesized for biosensing purposes in the present work. The NSL is employed for manufacturing ordered NanoHole Array (o-NHA) and NanoPrisms Array (NPA), whereas disordered NanoHole Array (d-NHA) and NanoDisk Array (NDA) are synthesized by SCL. The o-NHA and d-NHA consist in a thin metallic film ($50 \div 100$ nm) patterned with, respectively, an hexagonal and a disordered array of circular holes. The NPA consists in a honeycomb lattice of triangular shaped nanoprisms with edges of $\sim 100 \div 200$ nm and height of $40 \div 80$ nm. Finally, the NDA consists in a disordered array of non interacting disks $100 \div 300$ nm diameter and $40 \div 80$ nm height.

The NPA and the NDA due to their three-dimensional confinement exhibit the Localized Surface Plasmon Resonance property whereas the o-NHA and d-NHA support the Extended Surface Plasmon Resonance. In particular, the o-NHA, due to its ordered hexagonal pattern, possesses a remarkable optical property, the extraordinary optical transmission (EOT) [2]. Under specific conditions the intensity of the transmitted light through the o-NHA is greater than the intensity that would pass through a single hole with an area equivalent to the sum of all the nanohole apertures.

The plasmonic properties and the sensing performances are firstly investigated by Finite Elements Method (FEM) computation in order to optimize the morphologies and thus finding the best-performing nanostructures. The FEM computations are performed with two

different softwares, COMSOL Multiphysics® and EMUstack. Afterward, the nanofabrication techniques were studied and optimized in order to obtain a reproducible protocol for the patterning of large areas with gold nanostructures. Furthermore, the best morphological parameters obtained from numerical simulations are investigated experimentally in order to get the optimal optical and sensing properties.

Two kinds of biosensing tests are performed by first functionalizing the plasmonic nanostructures with proper biological receptors and then exposing the samples to the selected analyte. Firstly, a model system exploiting the interaction between Biotin and Streptavidin molecules is employed. Due to their high affinity, this complex is widely used as a proof-of-concept protocol for the detection assay. Here, biotin is used as a receptor whereas different concentrations of streptavidin as the analyte and thus the specificity and the limit of detection (LoD) are investigated. Secondly, a molecule of major interest in medical diagnostics is studied, the microRNA (miRNA), which consists of a non-coding RNA molecule that acts as a biomarker for specific diseases, like tumors. In this case complementary single stranded RNA molecules are employed, respectively, as receptor and target.

The present thesis is organized as follows:

Chapter 1 A theoretical description of the interaction between electromagnetic radiation and metallic nanostructures is presented;

Chapter 2 The state-of-art of LSPR and ESPR based biosensors is presented and the performances of different sensing platforms reported in literature are described;

Chapter 3 The two different nanofabrication techniques are described in detail by stressing the ability of finely tuning the morphological parameters and thus the plasmonic properties;

Chapter 4 Numerical simulations are carried out to design the optical properties and the sensing performances of the plasmonic nanostructures;

Chapter 5 The manufactured plasmonic nanostructures are characterized optically, morphologically, and their bulk and local sensitivities are investigated by taking into account the optimization from the numerical simulation;

Chapter 6 The results from the biosensing test with the biotin-streptavidin protocol are presented.

Chapter 7 The biorecognition tests for the microRNA molecule are, finally, reported.

1 Metallic Nanostructures and Electromagnetic Radiation

1.1 Interaction of electromagnetic radiation with matter

Plasmonics is a field of nanophotonics which studies how electromagnetic (EM) radiation can be confined within dimensions smaller than its wavelength. Interaction of electromagnetic fields with metals, which highly depends on frequency and electronic structure of the metal, can be described by Maxwell's equations, and optical properties of metals can be understood without reporting to quantum mechanics.

For low frequency radiation, as microwave or far-infrared, metals are very reflective and electromagnetic waves do not propagate through them. Only a negligible fraction of radiation penetrates into the metal to a depth called *skin depth*.

As frequency rises towards the visible part of the EM spectrum, field penetration in metals increases, dissipation becomes considerable and it results difficult to scale from low frequencies how metal works in visible range.

Finally, at ultraviolet frequencies (and in particular, below a characteristic frequency called plasma frequency, as it will be shown in the following), a metal acts as a dielectric and allows propagation of EM radiation. Refractive index and absorption depend on electronic band structure. For example, while alkali metals become transparent to UV radiation, noble metals, as gold and silver, have strong adsorption in UV range due to interband transition.

Optical and dispersive properties are described in a classical way via a *complex dielectric function* $\epsilon(\omega)$ which can be measured experimentally or calculated theoretically, using simple models such as the *Drude model*.

The startpoint for the study of electromagnetic response of metals is given by the Maxwell's macroscopic equations [17]:

$$\nabla \cdot \mathbf{D} = \rho_{ext} \tag{1.1a}$$

$$\nabla \cdot \mathbf{B} = 0 \tag{1.1b}$$

$$\nabla \times \mathbf{E} = -\frac{\partial \mathbf{B}}{\partial t} \tag{1.1c}$$

$$\nabla \times \mathbf{H} = \mathbf{J_{ext}} + \frac{\partial \mathbf{D}}{\partial t} \tag{1.1d}$$

which link the four macroscopic fields, electric field $\mathbf{E}$, magnetic field $\mathbf{B}$, dielectric displacement $\mathbf{D}$ and magnetic induction $\mathbf{H}$, with the external charge density ρ_{ext} and external current density $\mathbf{J_{ext}}$. Two more fields are introduced, polarization $\mathbf{P}$ and magnetization $\mathbf{M}$, and they are linked to the others by:

$$\mathbf{D} = \epsilon_0 \mathbf{E} + \mathbf{P} \tag{1.2a}$$

$$\mathbf{H} = \frac{1}{\mu_0}\mathbf{B} - \mathbf{M} \tag{1.2b}$$

Since only non magnetic media will be considered in the present study, the term $\mathbf{M}$ can be neglected and only polarization effects will be considered. Since the polarization $\mathbf{P}$ is related to internal charge density ρ_{int} by $\nabla \cdot \mathbf{P} = -\rho_{int}$, charge conservation $\nabla \cdot \mathbf{J} = -\frac{\partial \rho_{int}}{\partial t}$ implies that

$$\mathbf{J} = \frac{\partial \mathbf{P}}{\partial t} \tag{1.3}$$

At this point, if the medium is linear, isotropic and nonmagnetic, $\mathbf{D}$ and $\mathbf{H}$ are proportional to $\mathbf{E}$ and $\mathbf{B}$. Equations 1.2 can be expressed using relative electrical permittivity ϵ and magnetic permeability μ, which for nonmagnetic media is 1, as:

$$\mathbf{D} = \epsilon_0 \epsilon \mathbf{E} \tag{1.4a}$$

$$\mathbf{B} = \mu_0 \mu \mathbf{H} \tag{1.4b}$$

Moreover, for the same medium, there is another linear relationship, between internal current density $\mathbf{J}$ and electric field $\mathbf{E}$ where the conductivity σ is introduced

$$\mathbf{J} = \sigma \mathbf{E} \tag{1.5}$$

However equations 1.4a and 1.5 are correct for linear media that do not exhibit temporal or spatial dispersion. These assumptions are not satisfied by metals whose response strongly depends on frequency. Taking into account the non-locality in time and space, the linear $(\mathbf{r}, t)$ relationships are generalized as

$$\mathbf{D}(\mathbf{r}, t) = \epsilon_0 \int dt' \mathbf{dr}' \epsilon(\mathbf{r} - \mathbf{r}', t - t') \mathbf{E}(\mathbf{r}', t') \tag{1.6a}$$

$$\mathbf{J}(\mathbf{r}, t) = \int dt' \mathbf{dr}' \sigma(\mathbf{r} - \mathbf{r}', t - t') \mathbf{E}(\mathbf{r}', t') \tag{1.6b}$$

Equations 1.6 are simplified by taking their Fourier transforms in $(\mathbf{k}, \omega)$ domain, converting convolution into multiplication:

$$\mathbf{D}(\mathbf{k}, \omega) = \epsilon_0 \epsilon(\mathbf{k}, \omega) \mathbf{E}(\mathbf{k}, \omega) \tag{1.7a}$$

$$\mathbf{J}(\mathbf{k}, \omega) = \sigma(\mathbf{k}, \omega) \mathbf{E}(\mathbf{k}, \omega). \tag{1.7b}$$

Using equations 1.2a, 1.3 and 1.7 a relationship is found between conductivity σ and relative permittivity ϵ (from now on called *dielectric function*):

$$\epsilon(\mathbf{k}, \omega) = 1 + \frac{i\sigma(\mathbf{k}, \omega)}{\epsilon_0 \omega}. \tag{1.8}$$

Due to this intimate relationship electromagnetic phenomena can be described using either quantity. Historically, conductivity is preferably used at low frequencies while dielectric function is used at optical frequencies.

In this work, properties in NIR-Vis-UV range will be studied so from now on only dielectric function ϵ will be considered. In the next section, a simple model to calculate ϵ will be introduced.

In eq. 1.7 a further simplification is done considering spatially local interaction. This is valid as long as the wavelength λ of the EM radiation is larger than other relevant dimensions, as unit cell size and mean free path of electrons. This condition is fullfiled up to the ultraviolet frequencies ($\lambda \lesssim 100nm$). Under this assumption dielectric function

becomes $\epsilon(\mathbf{k} = \mathbf{0}, \omega) = \epsilon(\omega)$

In general ϵ is a complex function of the angular frequency ω, which is a real value, and can be expressed as $\epsilon(\omega) = \epsilon_1(\omega) + i\epsilon_2(\omega)$. However, via reflectivity measurements, complex refractive index $\tilde{n}(\omega) = n(\omega) + ik(\omega)$ of the medium can be determined. Taking into account that $\tilde{n}(\omega)$ is defined by

$$\tilde{n}(\omega) = \sqrt{\epsilon(\omega)}, \tag{1.9}$$

finally the dielectric function can be calculated as follows:

$$\epsilon_1 = n^2 - k^2 \qquad \epsilon_2 = 2nk \tag{1.10}$$

The complex part of $\tilde{n}(\omega)$, k, is called the *extinction coefficient* and determines the optical adsorption of EM radiation propagating through a medium. It is proportional to the absorption coefficient α of Beer's exponential attenuation law in a medium ($I(x) = I_0 e^{-\alpha x}$) by

$$\alpha(\omega) = \frac{2k(\omega)\omega}{c} \tag{1.11}$$

1.1.1 Drude model

As pointed out previously, the dielectric function $\epsilon(\omega)$ tells most of the information about the interaction between metal and EM radiation. A simple model to calculate ϵ for the frequency range of interest for the present work, i.e., VIS and NIR portion of the spectrum, is the Drude model of free electron gas. Here, a density n of free electrons is supposed to move against a fixed lattice of positive ions. Since electrons are supposed to be free particles, details of lattice potential and electron-electron interactions are neglected. Moreover, some aspects of band structure could be embedded in the electron mass by considering effective mass of the electron.

When a radiation impinges a metal, electrons move according to the external field until they collide with a positive ion. Collisions occur with a caracteristic frequency $\gamma = 1/\tau$, where τ is the relaxation time of the free electron gas, and γ typically is of the order of 100 THz at room temperature.

Despite these strong assumptions, this model gives good results in a wide range of frequencies, up to the interband transitions of the metal. While for alkali metals the model fits well up to the ultraviolet frequencies since interband transitions are in UV range, for noble metals these occur at optical wavelengths and its validity is limited.

To take into account interband transitions, which lead to high absorption of radiation, contribution of bound electrons should be considered and this will be studied in section 1.1.2.

Considering only free electrons and a driving electric field $\mathbf{E}$ one obtains a simple equation of motion

$$m\ddot{\mathbf{x}} + m\gamma\dot{\mathbf{x}} = -e\mathbf{E}. \tag{1.12}$$

Assuming a harmonic dependence for the electric field $\mathbf{E}(t) = \mathbf{E_0} e^{-\imath\omega t}$, the steady state solution has the same harmonic dependence $\mathbf{x}(t) = \mathbf{x_0} e^{-\imath\omega t}$, where $\mathbf{x_0}$ is a complex value. Using $\mathbf{x}(t)$ in 1.12 leads to the solution

$$\mathbf{x}(t) = \frac{e}{m(\omega^2 + \imath\gamma\omega)}\mathbf{E}(t) \tag{1.13}$$

As $\mathbf{x}(t)$ is the displacement of a single electron, this gives a single electric dipole moment

$\mathbf{p}(t) = -e\mathbf{x}(t)$. Macroscopic polarization P is obtained from contribution of all the n electrons in a unit of volume

$$\mathbf{P} = -ne\mathbf{x} = -\frac{ne^2}{m(\omega^2 + \imath\gamma\omega)}\mathbf{E} \tag{1.14}$$

Upon inserting eq. 1.14 into the eq. 1.2a the displacement vector $\mathbf{D}$ results:

$$\mathbf{D} = \epsilon_0 \left(1 - \frac{\omega_p^2}{\omega^2 + \imath\gamma\omega}\right)\mathbf{E} \tag{1.15}$$

where the plasma frequency of the free electron gas $\omega_p^2 = \frac{ne^2}{\epsilon_0 m}$ was introduced. The quantity between the brackets above is the dielectric function from Drude model and separating real and imaginary part results

$$\epsilon(\omega) = 1 - \frac{\omega_p^2}{\omega^2 + \imath\gamma\omega} = \left(1 - \frac{\omega_p^2}{\omega^2 + \gamma^2}\right) + \imath\left(\frac{\omega_p^2\gamma}{\omega(\omega^2 + \gamma^2)}\right) = \epsilon_1(\omega) + \imath\epsilon_2(\omega). \tag{1.16}$$

For frequencies $\omega < \omega_p$, the model gives good results. At higher frequencies such as $\omega \gg \omega_p$, equation 1.16 gives $\epsilon(\omega) \to 1$. For real metals and specially for noble metals this is false, as the d band electrons are close to the Fermi surface and they take to greater polarization. This effect can be included in equations above by adding the term $\mathbf{P}_\infty = \epsilon_0(\epsilon_\infty - 1)$ in eq. 1.2a so $\mathbf{P}$ now represents only the polarization due to free electrons. With this correction dielectric function becomes

$$\epsilon(\omega) = \left(\epsilon_\infty - \frac{\omega_p^2}{\omega^2 + \gamma^2}\right) + \imath\left(\frac{\omega_p^2\gamma}{\omega(\omega^2 + \gamma^2)}\right) \tag{1.17}$$

where $\epsilon_\infty \simeq 1 \div 10$. The validity of this model for noble metals is shown in Fig.1.1 where experimental data for real and imaginary part of $\epsilon(\omega)$ from Johnson and Christy [1] are compared with the dielectric function from Drude model (Eq.1.17). Model agrees with experimental measurements as long as interband transitions are not important. Specifically, interband transitions become relevant above 2 eV (i.e., below 600 nm) for copper and gold and above 4 eV (below 300 nm) for silver. Above those energies ϵ_2 increases and metals present high adsorption for such radiation.

To summarize, the Drudel model describes correctly optical response of metals up to the threshold of interband transitions and specifically for silver works down to UV wavelength (300 nm) while for gold and copper validity is limited down to (600 nm).

A big advantage of having an analitycal formula for dielectric function is that it can be easily included in numerical solvers for Maxwell's equations, such as the finite-difference time-domain (FDTD) scheme [18].

1.1.2 Lorentz-Drude model

Above the frequency thresholds incident radiation is such that bounded d electrons, below Fermi surface, are excited to higher bands yielding strong adsorption and competition between the two excitations of s and d electrons.

To take into account the contribution of bounded electrons an additional elastic term is added to the equation of motion 1.12:

$$m\ddot{\mathbf{x}} + m\gamma\dot{\mathbf{x}} + m\omega_0^2\mathbf{x} = -e\mathbf{E}. \tag{1.18}$$

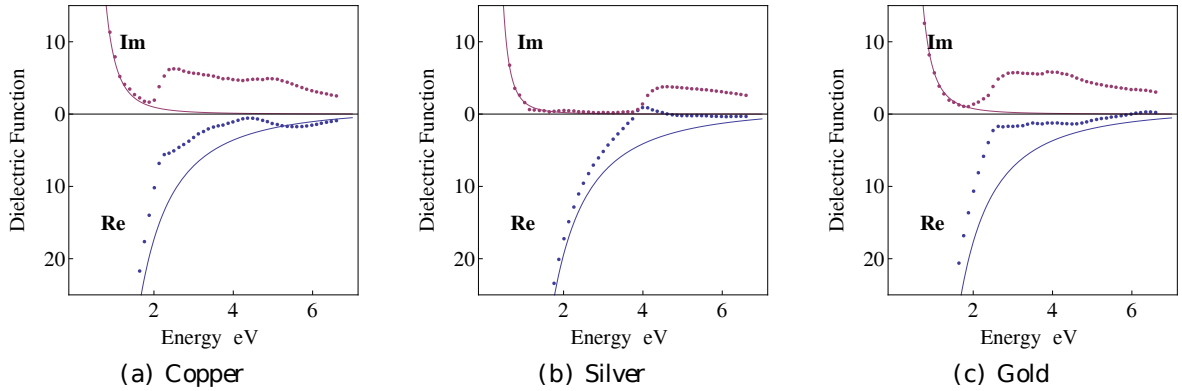

Figure 1.1: Solid line represents dielectric function $\epsilon(\omega)$ from Drude model fitted to experimental data from Johnson and Christy [1] (dotted line)

	$Au(\epsilon_\infty = 1.1156, \sigma/\epsilon_0 = 1355.01 s^{-1})$			$Ag(\epsilon_\infty = 1.4783, \sigma/\epsilon_0 = 3157.56 s^{-1})$		
	A_i[eV]	B_i[eV^2]	C_i[eV^2]	A_i[eV]	B_i[eV^2]	C_i[eV^2]
$i=1$	$-8.577 \cdot 10^4$	$-1.156 \cdot 10^4$	$5.557 \cdot 10^7$	$-1.160 \cdot 10^5$	-3050	$3.634 \cdot 10^8$
$i=2$	-2.875	0.0	$2.079 \cdot 10^3$	-4.252	-0.8385	112.2
$i=3$	-997.6	-3090	$6.921 \cdot 10^5$	-0.4960	-13.85	1.815
$i=4$	-1.630	-4.409	26.15	-2.118	-10.23	14.31

Table 1.1: Coefficients of L4 model for Au and Ag

Interband transition are therefore included considering the bounded electrons as oscillators with an own resonance frequency ω_0. This frequency corresponds to a particular interband transitions with $\hbar\omega_0$ energy. If more interband transitions are considered, there will be the same number of equations like Eq.1.12 to solve, each of them with its own resonance frequency.

Each single equation leads to a Lorentz-oscillator term of the form

$$\frac{S_i}{\omega_i^2 - \omega^2 - \imath\gamma_i\omega}$$

that adds up to the dielectric function yet calculated for free-electrons [19]. Here ω is the radiation frequency while ω_i is the resonance frequency of the i-th interband transition, whose oscillator strength is S_i.

Generally, if N interband transitions are considered, the resulting dielectric function can be written as:

$$\epsilon(\omega) = \epsilon_\infty - \frac{\omega_p^2}{\omega^2 + \imath\gamma\omega} + \sum_{i=1}^{N} \frac{S_i}{\omega_i^2 - \omega^2 - \imath\gamma_i\omega} \tag{1.19}$$

For example, taking into account 4 interband transitions, *L4* model is obtained. Reminding the relationship between ϵ and σ (Eq.1.8) and renaming coefficients, the dielectric function becomes

$$\epsilon(\omega) = \epsilon_\infty - \frac{\imath\sigma}{\epsilon_0\omega} + \sum_{i=1}^{N} \frac{C_i}{\omega^2 + \imath A_i\omega + B_i}. \tag{1.20}$$

Coefficients for eq. 1.20 were calculated by Nordlander and Hao [20] and are shown in

table 1.1. In figure 1.2 can be observed that *L4* analytical dielectric function $\epsilon(\omega)$ fits very well experimental data and it turns helpful for numerical calculations, due to the computationally simple formula for $\epsilon(\omega)$.

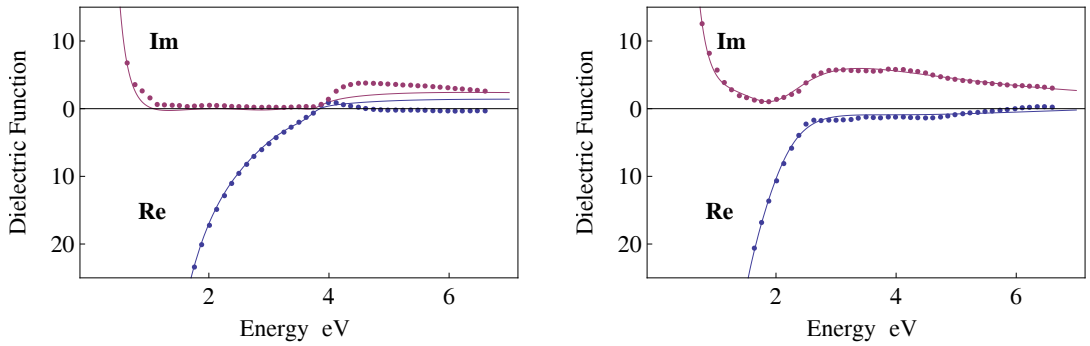

(a) Silver **(b)** Gold

Figure 1.2: Dielectric constant from *L4* model and experimental data from Johnson and Christy

1.2 Plasmon Excitations

1.2.1 Volume Plasmons

Considering ϵ from free-electron model (eq. 1.16) and considering its high frequency limit ($\omega > \omega_p \gg \gamma$, therefore, neglecting interband contribution to $\epsilon(\omega)$), it is easy to show that metals are transparent to the radiation. Indeed, $\epsilon(\omega)$ becomes predominantly real, as the imaginary part becomes negligible, and it results

$$\epsilon(\omega) \sim \epsilon_1(\omega) = 1 - \frac{\omega_p^2}{\omega^2}. \tag{1.21}$$

Reminding eq. 1.1c, 1.1d from Maxwell's equations, where $J_{ext} = 0$ is assumed, and combining them with the above dielectric function, a wave equation is found. Thus, in this regime metal supports propagating waves whose dispersion relation results

$$\omega^2 = \omega_p^2 + k^2 c^2 \tag{1.22}$$

On one side, only transverse electromagnetic waves propagates through the plasma with the dispersion relation above. On the other side, the electron sea presents longitudinal quanta oscillations against fixed ions with ω_p frequency. The quanta of these charge oscillations are called *volume plasmons*, which are collective excitations of the free electrons in the metal, and, due to their longitudinal nature, they cannot couple with transverse EM waves. Thus, the only way to excite volume plasmons is by particle impact.

1.2.2 Surface Plasmon

An other type of plasmon oscillation, that has a central role in this work, is the Surface Plasmon (SP). It arises at an interface between a metal and a dielectric. In particular, if oscillations occur at an extended interface they are named Surface Plasmon Polaritons (SPP) or Extended Surface Plasmons (E-SP), otherwise, if they occur at the surface of

three-dimensional confined nanoparticles, excitations are called Localized Surface Plasmons (L-SP).

Surface Plasmon Polaritons consist of electromagetic excitations propagating along the interface between a dielectric and a metal and are confined evanescently in the perpendicular direction. Such waves arise when incident EM radiation couples to the oscillation modes of the conduction-electron plasma at the interface. Due to the confinement in sub-wavelength volumes at the interface, EM field enhancement can be obtained. The EM waves can't couple directly to the electron oscillations because of a momentum gap between the two corresponding dispersion relations. However in the following sections some strategies that allow the coupling will be presented.

Localized Surface Plasmons are non-propagating excitations of the conduction electrons in a three-dimensionally confined nanostructure coupled to the EM field. The curved surface of the sub-wavelength size nanoparticle exerts a restoring force on electrons thus, under certain conditions, a resonance may occur between incident light and electrons. This resonance is called Localized Surface Plasmon Resonance (LSPR) and leads to a field enhancement near the surface of the nanostructure both inside the metal and outside in the surrounding dielectric environment. Differently to propagating SPPs, localized plasmon resonances can be directly excited by light, without the use of special coupling technique.

1.3 Surface Plasmon Polaritons

1.3.1 Surface Plasmon Polaritons at a flat interface

The startpoint to study physical properties of SPP is the wave equations obtained by combining eq. 1.1c and 1.1d from Maxwell's equations:

$$\nabla^2\mathbf{E} - \frac{\epsilon}{c^2}\frac{\partial^2\mathbf{E}}{\partial t^2} = 0, \tag{1.23}$$

where negligible variation of ϵ is assumed over distances of optical wavelengths. Considering, in all generality, a harmonic time dependence $\mathbf{E}(\mathbf{r},t) = \mathbf{E}(\mathbf{r})e^{-\imath\omega t}$, the wave equation results

$$\nabla^2\mathbf{E} + k_0^2\epsilon\mathbf{E} = 0, \tag{1.24}$$

where $k_0 = \frac{\omega}{c}$ is the wave vector of the propagating radiation in vacuum, and in this form it is known as the *Helmholtz equation*.

Assuming a semi-infinite media geometry as described in figure 1.3, waves travel along x-direction while ϵ depends only on z-direction. Moreover, a planar interface is assumed between metal and dielectric, that coincides with $z = 0$.

Under this geometry assumptions, propagating waves at $z = 0$ interface along x-direction can be described as $\mathbf{E}(x,y,z) = \mathbf{E}(z)e^{i\beta x}$, where β, the *propagation constant*, is the component of the wave vector in the direction of propagation. This yields a simplified form of eq. 1.24

$$\frac{\partial^2\mathbf{E}(z)}{\partial z^2} + (k_0^2\epsilon - \beta^2)\mathbf{E}(z) = 0. \tag{1.25}$$

A similar equation can be found for the magnetic field $\mathbf{H}$. In order to solve these two equations and to get explicit expressions for the fields, boundary conditions are imposed at the interface $z = 0$.

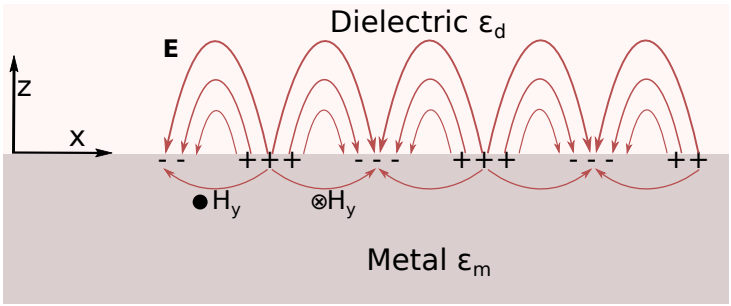

Figure 1.3: Geometry for SPP propagation at interface between a metal and a dielectric. Electric and magnetic fields for the p-polarized SPP are also described.

Two sets of solutions with different polarization are found, according to the polarization of the incident radiation: transverse magnetic (TM) and transverse electric (TE) mode. Once defined the scattering plane as the plane on which the incident and the reflected radiation lay, the TM wave has magnetic field **H** perpendicular to this plane while the TE wave has the electric field perpendicular to the scattering plane. It is simple to show that surface plasmon polaritons only exist for TM polarization, so solutions for the electric field will have propagating component along x-direction with β wave vector, null component along y-direction and evanescent component along z-direction.

For TM modes a dispersion relation is found, after imposing boundary conditions:

$$\beta = k_0 \sqrt{\frac{\epsilon_m \epsilon_d}{\epsilon_m + \epsilon_d}} \tag{1.26}$$

where ϵ_m and ϵ_d are respectively dielectric function of the metal and the dielectric. This relation is valid for both real and complex ϵ_m, or equivalently for metals without or with attenuation respectively.

Ideal conductor metal An explicit dispersion relation $\omega(\beta)$ can be found, for example, assuming that the metal has no attenuation and thus considering a purely real dielectric function from eq. 1.21 for ϵ_m. In figure 1.4a the dispersion relation $\omega(\beta)$ and both real and immaginary part of the wave vector β are plotted for two different interfaces air/metal and silica/metal. SPP excitations correspond to the part of the dispersion curve at the right side of the light line due to their bound nature. For air and silica real dielectric constants are considered respectively 1 and 2.25.

For large wave vectors, frequency of SPPs tends to finite value, the *surface plasmon frequency* ω_{sp}. In fact, inserting eq. 1.21 in eq. 1.26, for large k it results

$$\omega_{sp} = \frac{\omega_p}{\sqrt{1 + \epsilon_d}} \tag{1.27}$$

As ω approaches to ω_{sp}, wave vector tends to infinity and group velocity of oscillation $v_g = \frac{\partial \omega}{\partial k}$ tends to zero. In this case oscillation mode acquires electrostatic character and it is called *surface plasmon*. Therefore such mode is obtained when $\epsilon_m(\omega) + \epsilon_d = 0$.

Real metal at interface Above, the metal at the interface was assumed to be an ideal conductor (no dissipation). If real metal is then considered, both ϵ_m and β become complex quantities. In this case ω_{sp} is reached at a finite wave vector and excitation becomes a damped SPP oscillation with a propagation length $L = (2Im(\beta))^{-1}$ (typically between

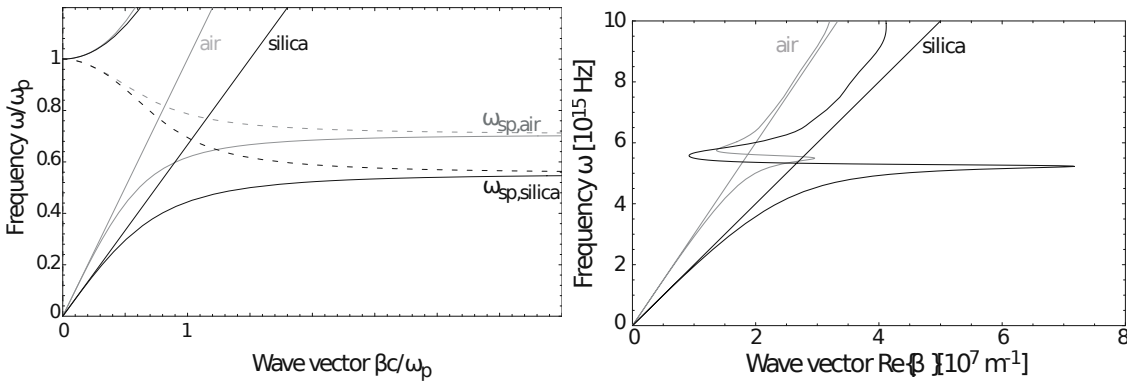

Figure 1.4: (a) Dispersion relation at air/Drude metal and silica/Drude metal interfaces for dispersionless metals. Solid and dashed curves represent respectively $Re\{\beta\}$ and $Im\{\beta\}$ while straight lines represent light lines $\omega = kc/n$. **(b)** Dispersion relation at air/metal and silica/metal interfaces for real metals (silver in this case).

10 and 100 µm). Additionally, this sets a lower limit for oscillation wavelength and for confinement length perpendiculary to the interface.

It is important to underline that SPP cannot be excited at an interface directly by incident electromagnetic radiation since the propagation constant β is always greater than the component of radiation wave vector k along the interface. Two different techniques for coupling radiation with SPPs are *prism coupling* and *grating coupling* and they will be described in the following sections.

1.3.2 Prism Coupling

As previously observed, in order to excite SPP special techniques for phase-matching are needed, since the projection of wave vector of the radiation along the interface ($k_x = k\sin(\theta)$) is always smaller than the SPP propagation constant β.

A way to get phase-matching to SPPs is to put a thin metal layer between two insulators with different real dielectric constants. One is assumed to be air($\epsilon_1 = 1$) and the other is a dielectric material in the form of a prism with $\epsilon_2 > 1$.

If, inside the prism, the radiation impinges the prism/metal interface with θ incidence angle and it is totally reflected, the metal will have an in-plane wave vector $k_x = k\sqrt{\epsilon_2}\sin(\theta)$ that is sufficient to excite a SPP at metal/air interface. Therefore, the excitation of a SPP is detected experimentally as a minimum in the reflected light because, in this case, most of the radiation remains confined at the interface instead of being reflected backwards.

In figure 1.5 both dispersion relations are ploted for air/metal and prism/metal interfaces, where a Drude metal is considered. Since light line in the prism crosses the air/metal SPP dispersion relation, it implies that EM waves in the prism are able to excite SPP modes at air/metal interface.

Two common geometries are usually used to excite SPP modes. Both Kretschmann configuration and Otto configuration are illustrated in figure 1.6 and both are based on attenuated total internal reflection (ATR) at prism/metal interface. In Kretschmann geometry a thin metal layer is directly deposited on the glass prism whereas in Otto geometry metal layer and prism are separated by a thin air gap.

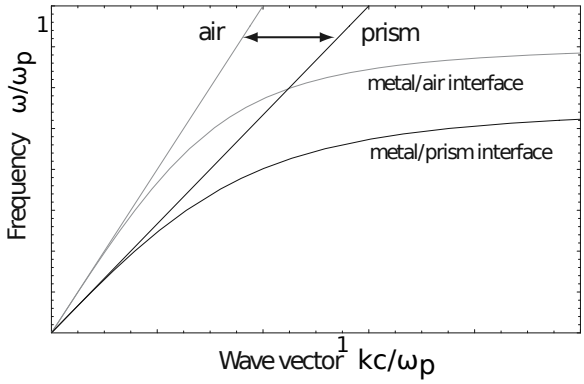

Figure 1.5: SPP dispersion and light lines for prism coupling. The accessible propagation constants for SPP are those between the two light lines.

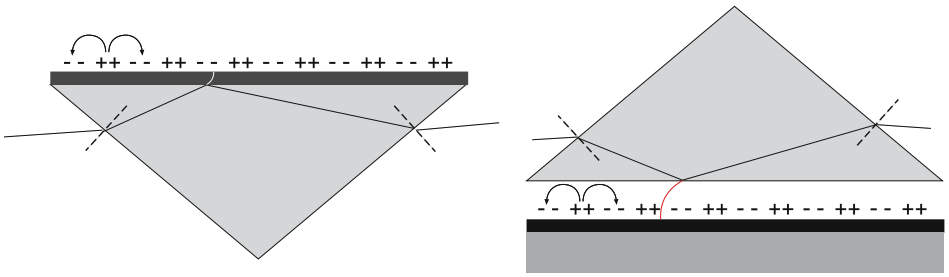

Figure 1.6: Prism coupling to SPPs via attenuated total internal reflection in Kretschmann (left) and Otto (right) configurations.

1.3.3 Grating Coupling

Another way to provide the missing wave vector in order to couple impinging photons and SPPs is patterning the metal surface with a lattice of grooves or holes. The ordered array of corrugations can be described by a primitive cell and basis vectors. This yields the presence of reciprocal lattice vectors, and these can provide the missing momentum needed for SPP excitation.

For a simple one-dimensional array of grooves with its periodicity a, illustrated in figure 1.7, SPP excitation arises whenever the following condition is satisfied

$$\beta = k\sin(\theta) + \frac{2\pi}{a}j. \tag{1.28}$$

In this equatiom $k\sin(\theta)$ is the in-plane component of incident light wavevector and $\frac{2\pi}{a}j$ is a wavevector from reciprocal lattice, where $j \in \mathbb{Z}$. Here $\mathbf{k}$ is considered parallel to the grating direction so incidence plan is perpendicular to the grooves.

If corrugations at interface are shallow, with depth of order of 10 nm, no significant changes occur to the SPP dispersion relation so eq. 1.26 can be used for β. As with prism coupling, excitation of SPPs is detected as a minimum in the reflected intensity. In the presence of a grating also the reverse process can take place. A SPP travelling across a surface can couple to the light and radiate if meets up a grating.

As the size of corrugations increases, the interface can no longer be treated as a small perturbation of the flat interface and dispersion relation 1.26 is no longer accurate. Moreover, localized modes arise as the depth of the grooves grows. A further case will be treated in section 1.5, that is when grating lattice becomes an ordered array of holes through the

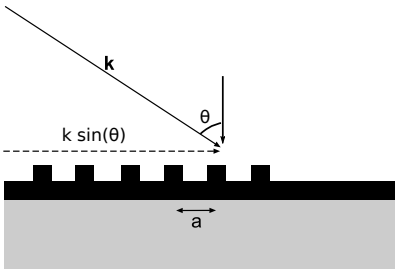

Figure 1.7: Grating coupling between light and SPPs.

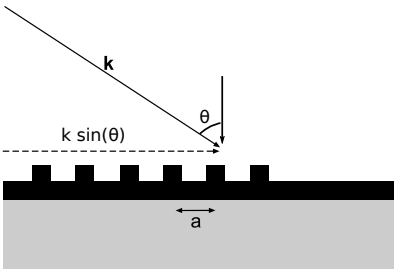

Figure 1.8: Scheme for SPP excitation in the conical mounting.

metal film. Such system presents peculiar optical properties, like the Extraordinary Optical Transmission (EOT), as discussed below.

1.3.4 1D sinusoidal grating

Surface plasmons can be excited, for example, on a metallic surface patterned with a one-dimensional sinusoidal grating. Besides the coupling where $\mathbf{k_0}$ of the incident light is aligned with the grating direction, as depicted in figure 1.7, the plasmon excitation can occur even when the plane of incidence is azimuthally rotated with respect to the grating direction [21]. Such a configuration is called *conical mounting* and it is presented in figure 1.8. In this case the component of wave vector parallel to the sample surface, given by $k_T = k_0 \sin(\theta)$ where θ is the incidence angle, it is not parallel to the direction of the grating given by the reciprocal space vector $\mathbf{G} = \frac{2\pi}{\Lambda}\hat{\mathbf{G}}$ where Λ is the periodicity of the grating. In fact there is a nonzero azimuth angle ϕ between the two directions. Only the component of $\mathbf{G}$ normal to the scattering plane is transferred for the coupling, and thus two surface plasmons can be excited in directions nonparallel to the scattering plane [22]. The resonance condition can be found as follows, for both cases with $\beta < G$ and $\beta > G$:

$$\begin{cases} \beta_x = G\cos\phi - k_T = G\cos\phi - \frac{2\pi}{\lambda}\sin\theta \\ \beta_y = G\sin\phi \end{cases} \qquad \text{for } G > \beta \tag{1.29}$$

$$\begin{cases} \beta_x = \mp G\cos\phi - k_T = \mp G\cos\phi - \frac{2\pi}{\lambda}\sin\theta \\ \beta_y = \mp G\sin\phi \end{cases} \qquad \text{for } G < \beta \tag{1.30}$$

Measurements of the reflectance angular spectra can be done varying the incidence angle θ once fixed a wavelength for the light source and an azimuth angle ϕ. The excitation of the two surface plasmons is revealed as two dips in such spectra. If the spectra are acquired for multiple wavelengths shifts of the reflectance dip are observed.

1.4 Localized Surface Plasmons and Mie Scattering

As introduced previously, the L-SP phenomenon occur when light impinges a three-dimensionally confined plasmonic nanostructures, such as spheres. The LSPR arises for a specific incident λ_{LSPR} without needing any special coupling technique.The λ_{LSPR} depends on the composition and the morphology of the nanostructure and on the dielectric function of the surrounding environment. For example, the LSPR phenomenon for a wide range of configurations of gold and silver nanoparticles can be excited by radiation in the visible/near-infrared range.

There is no general analytic solution to describe the dependence of λ_{LSPR} on the shape, size and composition and in most of the cases numerical simulations have to be carried out in order to predict properly the scattering from a nanoparticle.
However, the scattering of the light from a single non-interacting spherical particle was solved analitically by Gustav Mie in 1908 [23]. The solutions for the internal and scattered fields were computed by the multipolar expansion, given the symmetry of the nanoparticle itself. A further analytical treatment was provided by Gans [24] who proposed the solutions for ellipsoidal non-interacting particles.

1.4.1 Quasi-static regime

The quasi-static regime approximation consists in considering a nanoparticle much smaller than the λ of the impinging light. The spatial variation and the phase difference of the electric field across the nanoparticle can be neglected, thus considering the nanoparticle immersed in uniform electric field that varies in time.
The following convenient geometry was considered: a homogeneous, isotropic sphere of radius R immersed in a uniform static electric field $\mathbf{E} = E_0\hat{\mathbf{z}}$ and embedded in an isotropic loss-less medium with dielectric constant ϵ_m. In the electrostatic approach, the equation to solve is the Laplace equation $\nabla^2\Phi = 0$, where Φ is the scalar potential. From Φ, the electric field can be computed by $\mathbf{E} = -\nabla\Phi$. By taking into account the spherical symmetry of the problem, the potential solution will be obtained from multipolar expansion:

$$\Phi(r,\theta) = \sum_{l=0}^{\infty}\left[A_l \cdot r^l + B_l \cdot r^{-(l+1)}\right] P_l(\cos\theta) \tag{1.31}$$

where $P_l(\cos\theta)$ are the Legendre Polynomials of l order, θ the angle between vector r to the point P and the $\mathbf{E_0}$. By imposing the boundary conditions and the continuity conditions on the particle surface it results that the nanosphere response could be described as an electrical dipole p situated in the center of the sphere and proportional to the applied field:

$$\mathbf{p} = 4\pi\epsilon_0\epsilon_m R^3 \frac{\epsilon - \epsilon_m}{\epsilon + 2\epsilon_m}\mathbf{E_0} \tag{1.32}$$

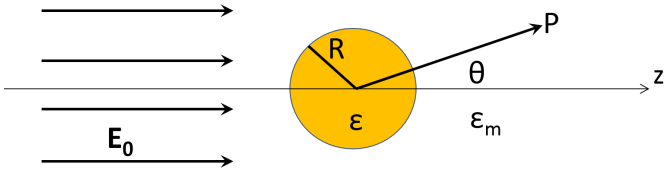

Figure 1.9: Geometry for the quasi-static approximation.

By remembering the definition $\mathbf{p} = \epsilon_0\epsilon_m\alpha\mathbf{E_0}$, the polarizability α is given by:

$$\alpha = 4\pi R^3 \frac{\epsilon - \epsilon_m}{\epsilon + 2\epsilon_m} \tag{1.33}$$

It can be observed that α would have a resonant enhancement when the denominator module $|\epsilon + 2\epsilon_m|$ is minimum. If $\mathrm{Im}[\epsilon]$ is negligible, the α diverges when the *Frölich condition* is fullfiled:

$$Re[\epsilon(\omega)] = -2\epsilon_m. \tag{1.34}$$

A resonance occurs when Frölich condition is fullfiled and it is associated with the dipole

surface plasmon of the metal nanoparticle, that is the LSPR. From equations 1.21 and 1.34 follows:

$$\omega_{LSPR} = \frac{\omega_p}{\sqrt{1+2\epsilon_m}} \tag{1.35}$$

where ω_p is the plasma frequency. This highlights a fundamental property of the LSPR, that is the dependence on the dielectric constant of the medium at the nanoparticle interface.

The electrical field, inside and outside the nanoparticle, is also enhanced if Frölich condition is fullfiled and is given by

$$\mathbf{E_{in}} = \frac{3\epsilon_m}{\epsilon + 2\epsilon_m}\mathbf{E_0} \tag{1.36}$$

$$\mathbf{E_{out}} = \mathbf{E_0} + \frac{3\mathbf{n}(\mathbf{n}\cdot\mathbf{p}) - \mathbf{p}}{4\pi r^3 \epsilon_0 \epsilon_m} \tag{1.37}$$

where $\mathbf{n}$ is the unit vector that represents the scattering direction. Finally, the scattering, the absorption and the extinction cross ansection were computed thanks to the electric fields (cf.[25]):

$$\sigma_{sca} = \frac{k^4}{6\pi}|\alpha|^2 = \frac{8\pi}{3}k^4R^6\left|\frac{\epsilon-\epsilon_m}{\epsilon+2\epsilon_m}\right|^2 \tag{1.38a}$$

$$\sigma_{abs} = k\mathrm{Im}[\alpha] = 4\pi kR^3\mathrm{Im}\left[\frac{\epsilon-\epsilon_m}{\epsilon+2\epsilon_m}\right] \tag{1.38b}$$

$$\sigma_{ext} = \sigma_{sca} + \sigma abs = 9\frac{\omega}{c}\epsilon_m^{3/2}V\frac{\epsilon_2}{(\epsilon_1+2\epsilon m)^2+\epsilon_2^2} \tag{1.38c}$$

where $k = 2\pi/\lambda$, R is the radius of the nanosphere and V its volume.

1.4.2 Size-correction

For larger nanospheres, the quasi-static approximation fails since the variation of the phase of the electric field across the nanosphere is no longer negligible. The dipolar theory was corrected for larger nanospheres [26, 27] and a new polarization was obtained:

$$\alpha = \frac{1-\frac{1}{10}(\epsilon+\epsilon_m)x^2 + O(x^4)}{\frac{1}{3}+\frac{\epsilon_m}{\epsilon-\epsilon_m} - \frac{1}{30}(\epsilon+10\epsilon_m)x^2 - \imath\frac{4\pi^2\epsilon_m^{3/2}}{3}\frac{V}{\lambda_0^3} + 0(x^4)} \tag{1.39}$$

where x represents the size parameter defined by $x = \frac{\pi R}{\lambda_0}$. Every term in the expression has a physical interpretation. The quadratic term at numerator is correlated with the retardation of the electric field over the volume V whereas the quadratic term at the denominator is linked to the retardation of the depolarization field inside the particle. Both this effects yield a redshift of the LSPR as the particle dimension increases.
The quadratic term at the denominator also reduces the importance of the $\mathrm{Im}[\epsilon(\omega)]$, thus increasing the polarization. However, the purely immaginary term at the denominator opposes to this increase of the polarization since it is linked to the radiation damping due to the decay of L-SP into photons. This effect becomes increasingly important for larger particles. Therefore, for larger particles the plasmonic resonance is damped by the decay of plasmons in photons whereas for smaller particle ($\sim 1-10$ nm) the absorption by interband and intraband transitions is dominant. For an arbitrary size a fully multipolar expansion has to be considered as calculated by G. Mie [23]

In a wider perspective, the extinction cross section, and thus the λ_{LSPR} at which the

resonance rises, depends also on the nanoparticle composition, size [28], shape [29, 3], orientation and local dielectric environment.

With regard to the composition, silver and gold are the most common plasmonic materials. The former presents the best plasmonic property in the Vis-NIR range but it oxidize whereas the latter has still good plasmonic properties and it's inert. However, in the last years alternative plasmonic materials were studied such as Titanium Nitride (TiN) [30], doped semiconductors or Transparent Conducting Oxides (TCO) [31].

1.4.3 Many Particles System

With respect to the single particle, if a particle array is considered then interaction between their localized modes might occur if the interdistance is not much larger than the particle dimensions. Such interaction could lead to a shift of the resonance condition with respect to the single particle case.

For a random distribution of nanoparticles, the coupling effects occur if the interdistance d is smaller than λ and particle size a. In an ordered array, if $a \ll d$ then particles can be considered non-interacting dipoles. On the contrary, if $d \sim a$ and both $d, a \ll \lambda$ then hot-spots with a high field enhancement arise in the space between the nanoparticles and the scattering is suppressed. Here, particles can be treated as interacting dipoles. Under these assumptions two different regimes are found, depending on the distance between particle. On one hand, if $d \ll \lambda$ then near-field interaction with a dependence of d^{-3} dominates and strong field localizaton is observed in space between adjacent particles. On the other hand, if $d \gg \lambda$ there is larger particle separation so far-field dipolar coupling with dependence of d^{-1} dominates.

1.5 Ordered NanoHole Array and Extraordinary Optical Transmission

This section will present a particular grating couplig technique to obtain plasmonic properties that consists in patterining a thin metallic film with an ordered array of nanometric holes. The excitation of Surface Plasmon Polaritons gives to this nanostructure special optical properties, such as extraordinary optical transmission (EOT), first described by Ebbesen [2]. This phenomenon constists in the transmission through a metallic ordered NanoHole Array (o-NHA) with subwavelength size of more light than that would pass through a hole with an area corresponding to the sum of the nanoholes areas. EOT phenomenon is excited and becomes relevant when hole's radius r is smaller than the wavelength λ_0 of the incident radiation.

For apertures with $r \gg \lambda_0$ propagating modes of radiation are allowed so transmission coefficient T, given by the ratio of total transmitted intensity to the incident intensity on holes area, approaches 1.

In case of sub-wavelength apertures Huygens-Fresnel principle can not be used and radiation does not propagate but it is transmitted by tunneling through the holes. Despite this, Bethe and Bouwkamp [32] provided an analytical solution for the transmission coefficient for a single hole T_{SH} of normally incident radiation through a single sub-wavelength circular hole in a perfectly conducting and opaque and infinitely thin screen:

$$T_{SH} = \frac{64}{27\pi^2}(kr)^4 \propto \left(\frac{r}{\lambda_0}\right)^4 \tag{1.40}$$

Relaxing the infinitely thin screen assumption and considering a finite thickness h, numerical simulations show that T_{SH} decreases exponentially with h [33]. On the other side, if finite conductivity is taken into account, it is enough for h to be on the order of several skin depths to restore screen's opacity.

Eq. 1.40 shows that transmission should rapidly goes to zero as λ_0 gets greater than hole's dimension. Despite this, Surface Plasmon Polaritons can enhance tranmission through such holes if a metal layer is patterned with a regular periodic lattice of holes [34]. Briefly, due to grating coupling, incident light excites SPP that travels through the hole then it is scattered in far field on the other side.

The presence of an ordered array yields a reciprocal space of wave vectors which helps radiation to couple with SPP. From eq. 1.28 it is easy to rewrite the condition, i.e., for a square lattice of holes with periodicity a:

$$\beta = k\sin(\theta) + nG_x + mG_y = k\sin(\theta) + (n+m)\frac{2\pi}{a} \tag{1.41}$$

Here k is the incident wavevector, G_x and G_y are basis wavevectors of the reciprocal lattice and n, m are Miller integer indexes, which define scattering order, thus direction of propagation of the excited SPP. Therefore, maximum transmission peaks can occur in presence of surface plasmon resonance when standing SPPs are formed on the surface (also called SPP-Bloch waves [35, 36]). It can be shown that such excitation arises, for normally incident radiation, whenever is fullfiled the condition

$$\lambda_{SPP}(n,m) = \frac{a}{\sqrt{n^2+m^2}}\sqrt{\frac{\epsilon_m\epsilon_d}{\epsilon_m+\epsilon_d}}. \tag{1.42}$$

Here, to get a first approximation, β from eq. 1.26 was assumed, where a flat infinite interface between metal and dielectric is considered. A rough approximation is done, just considering the periodicity of the structure in the null-aperture approximation and, as a consequence, the predicted peak positions are at slightly shorter wavelengths than those observed experimentally.

Under the same assumption, a similar condition for the maxima can be found for an hexagonal hole array with periodicity a [37]:

$$\lambda_{SPP}(n,m) = \frac{a}{\sqrt{\frac{4}{3}(n^2+nm+m^2)}}\sqrt{\frac{\epsilon_m\epsilon_d}{\epsilon_m+\epsilon_d}}. \tag{1.43}$$

As o-NHA can not be treated as small perturbation of the flat interface, in order to get more precise relations than eq. 1.42, 1.43 a more accurate relation for the propagation constant β of SPPs would be necessary. Moreover, these relations are valid for a single interface between two semi-infinite layers. Since the nanohole array has two interfaces that can be in contact with different dielectrics, different transmission spectra with different positions of the peaks can be obtained depending on which interface is illuminated by the incident radiation.

In presence of surface plasmon resonance, extraordinary optical transmission occurs. Let us define a normalized transmission coefficient T_{norm} as the ratio of the transmitted intensity through the nanohole array T_{NHA} to the sum of the ordinary transmissions of single holes T_{SH}:

$$T_{norm} = \frac{T_{NHA}}{\sum_j T_{SHj}} \tag{1.44}$$

At the surface plasmon resonance maxima with $T_{norm} > 1$ can be found in the transmission spectrum and this means that more light than that which incides on the area of all the apertures is transmitted. This is possible because even the light impinging on opaque regions between the holes can be channeled and transmitted to the other side via propagating SPPs.

This EOT property of nanoholes array was first demonstrated by Ebbesen and co-workers for a square array of circular holes in a thin silver film [2]. In figure 1.10a transmission spectrum of normally incident radiation on a 200 nm nm thick film of silver patterned with a nanohole array with 150 nm hole diameter and 900 nm periodicity. Several transmission peaks can be observed, two of which occur at wavelength greater than both the hole diameter and the array periodicity. This suggests that such transimission is not due to ordinary tunneling through holes but rather is mediated via SPPs.

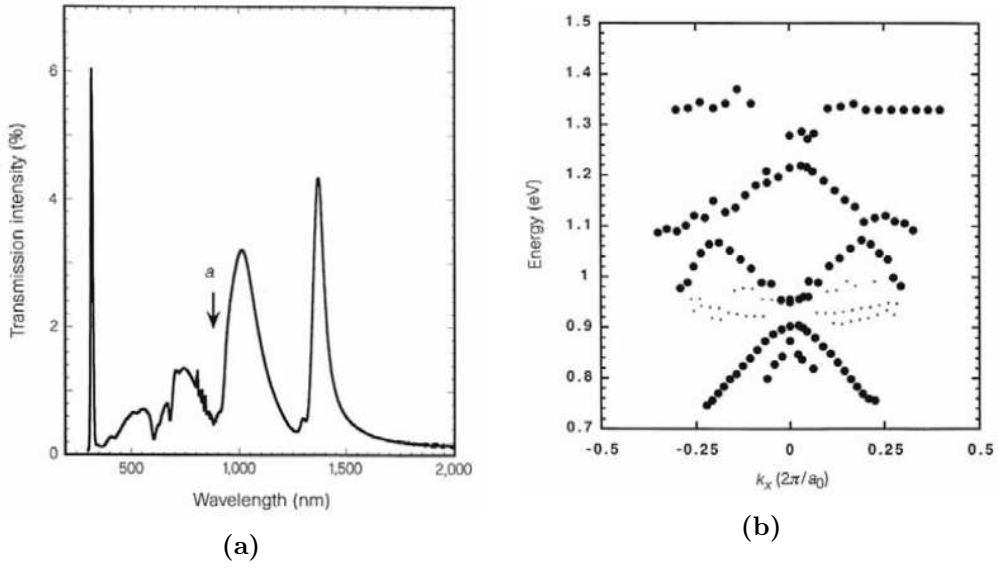

(a) **(b)**

Figure 1.10: (a) Normal-incidence transmission spectrum for a 200 nm silver film with square array of holes of 150 nm diameter with $a = 900$ nm periodicity. **(b)** Dispersion relation of grating-coupled SPPs along [10] direction extracted from the energy of transmission peaks as in fig. 1.10a. Plots copyrighted by Ebbesen et al.,1998 [2]

As previously showed also for LSPR, an important advantage of the plasmonic properties is the simplicity with which the spectral position of the plasmonic resonance properties can be tuned. In fact, despite the rough approximations used, it is clear from eq. 1.42, 1.43 that positions of peaks in the spectrum are directly proportional to the periodicity of the array.

Other geometrical parameters also influence the transmission spectra $T(\lambda)$, as described here after.

Thickness t of the metal film has to be larger than the skin depth δ in order to suppress the transmission through the metal and to highlight the transmissione mediated by SPPs through the holes. In this work, UV-Vis-NIR range of the EM spectrum will be considered and here $\delta \sim 1 \div 5$nm whereas the will be tenths of nm.

Hole diameter d has to fullfil $d \leq \lambda/2$ in order to supress the ordinary light propagation through the hole in advantage of the SPP mediated transmission.

Hole symmetry Different transmission spectra are observed with square rather than cir-

cular holes [38]. While circular hole, due to its symmetry, acts similarly in response to incident light with different polarization, square holes produce different spectra depending on polarization.

In addition to SPPs due to grating coupling, the penetration of the incident field inside the metal enables the strong localization of the field of localized surface plasmons on the rim of the each hole. In case of a single aperture in a flat film, presence of field hot-spots has two consequences that affect the transmission spectrum. On one hand, hole's effective diameter is increased as well as the cutoff wavelength, beyond which propagative modes are not allowed inside the hole. On other hand, the field-enhancement at the rim, whenever localized plasmons are excited, also increases the transmission. Nevertheless, a study of Degiron and Ebbesen [39] about role of localized modes in EOT through sub-wavelength nanohole arrays showed that they produce only minor changes in the transmission spectrum compared to the importance of propagating SPP.

Enhanced Transmission through disordered NanoHole Array

The localized modes around the nanohole have an important role in enhancing the transmission through a film patterned with a disordered array of nanometric holes. Even if the transmission mechanism is less efficient than the EOT of the ordered arrays, transmission through a disordered pattern is mediated by the the interconversion of L-SP and SPP [15, 40]. The plasmonic mediation of this transmittance mechanism is also demonstrated by the resonance-like shape of a transmittance peak centered at a wavelength greater than diameter of the holes and the average interdistance of the holes.

Conclusion

In this chapter the plasmonic properties of the nanostructures were presentend, and they are mainly divided into Localized Surface Plasmons and Extended Surface Plasmons. It has been stressed how the spectral position of a plasmonic resonance depends on the morphology and on the surrounding environment, namely on the dielectric constant. In this work the latter dependence will be exploited in order to develop nanostructures able to sense refractive index variations at the interface between nanostructures and the adjacent dielectric. More specifically, Localized Surface Plasmon Resonance and Surface Plasmon Resonance were exploited for biosensing applications, that represent the sensing of biomolecules that binds to a previously functionalized nanostructure thus changing the refractive index at the interface.

2 Biosensing with plasmonic nanostructures

2.1 Introduction

The possibility of fastly detect a biological marker has a fundamental importance in the biotechnology and in the medical diagnostics in particular. In these fields very low concentrations, below the picomolar (pM) level, of small biomolecules have to be detected in realtime without employing any labelling technique. For this purpose biosensors, that are devices able to reveal a specific biological compound called analyte (or target), are developed.

A biosensor fundamentally consists of a biological recognition layer designed to selectively bind to the analyte and a physical transducer, which translates the biochemical interaction with the analyte into a signal that can be more easily measured and quantified [41]. Biological receptors could be made, for example, by enzymes, antibodies, antigens or nucleic acids. These are chosen to specifically interact with the desired analyte thus giving the *specificity* property to the device.
The purpose of a biosensor is to produce a physical signal, either electrical or optical, which is proportional to the concentration of the bound analyte without any labelling strategies (e.g., with fluorophores), therefore working in the lable-free mode. On one side, biosensors that rely on electrical properties are reported in literature and they mainly employ Silicon NanoWire (SiNW) Field-Effect Transistor (FET) [42, 43]. The transduction mechanism is based on conductance variations of the SiNW-FET that occur when the analyte binds to the conveniently functionalized silicon surface. However the main drawback is that only charged biomolecules produces a conductance variance and thus a sensing signal.

On the other side the biochemical detection has been strongly improved in optical devices by the Surface Plasmon Resonance (SPR) based devices and they can be employed to sense any kind of biological or chemical analyte such as proteins, oligonucleotides, virus, bacteria, toxines, DNA chains, cancer markers, allergy markers, antibodies, drugs and hormones. SPR devices have gained increasing interest both in enhancing the signal from surface-enhanced spectroscopic methods [44] and in affinity sensing as optical transducers [3]. In the latter case, the plasmon spectroscopy gained reputation as a high-sensitive method for detecting molecules of both biological and chemical interest. With respect to other optical sensors, the plasmonic ones do not require the analyte to be labelled with an optically-active marker in order to reveal binding events [45]. Therefore, an active and intense research was devoted to optimize the performances of plasmonic biosensors in terms of sensitivity, resolution and limit of detection. In the next sections the principle of SPR sensing will be described and then the most common SPR sensing platforms and their performances will be reported.

2.2 Principle of Surface Plasmon Resonance sensing

The first biosensing application of SPR was demonstrated in 1983 by Liedberg et al. [46] and since then many domains as biology and medical diagnostics widely employed this technique[47]. The potential of SPR-based sensors lies in the very high sensitivity of the plasmonic excitations at metal-dielectric interface to a change of the refractive index of the adjacent dielectric. The disperison relation in eq. 1.26 for the propagation constant β of the surface plasmons at the interface can be rewrited, and by considering the relation between the refractive index and the dielectric constant from 1.1 it yields:

$$\beta = k \cdot \sqrt{\frac{\epsilon_m n_d^2}{\epsilon_m + n_d^2}} \tag{2.1}$$

where k is the wavenumber of the incident light, ϵ_m is the dielectric constant of the metal and $n_d = \sqrt{\epsilon_d}$ is the refractive index of the adjacent dielectric. On one side this relation points out that Extended Surface Plasmons (E-SP) can be excited if the materials at the interface fulfill the condition $\epsilon_m < -n_d^2$, that requires a metallic/dielectric interface. Silver and gold satisfy this condition in the Vis-NIR range and also present relatively small losses. On the other side, the relation highlights how a local variation of the refractive index yields a change of the plasmonic property. Therefore, the simplest transduction system consists of a metallic film. A variation of n_d alters the resonance condition necessary for exciting Extended Surface Plasmons on the surface of the metallic film. The change of the coupling condition between E-SP and the interacting optical wave can be detected by measuring the optical properties. Different characteristics of the incident light interacting with plasmons can be interrogated and thus SPR based sensors can be divided in four categories that rely, respectively, on angular, wavelength, intensity or phase modulation [48]. The angular and the wavelength modulation represent the most commonly used techniques due to the their high resolution and to the simpler experimental setup required.

Angular modulation A monochromatic light wave with a variable angle of incidence is used to excite E-SPs. Angular spectra of reflected light are measured at multiple angles of incidence and the coupling with an E-SP is observed as a dip in the reflectivity spectrum. The strongest coupling occurs at the minimum in the spectrum, and it corresponds to the resonance angle $\theta_{\text{E-SP}}$. Therefore, when n_d changes $\theta_{\text{E-SP}}$ varies accordingly and represents the sensor output.

Wavelength modulation A polychromatic optical source is employed with a fixed optical setup. The plasmon excitation is observed as a dip in wavelength spectra of reflected light. Here, the resonance wavelength λ_{E-SP} represents the sensor output.

Intensity modulation Here, both the angle of incidence and wavelength are fixed, and the absolute intensity of reflected light wave serves as a measurement of coupling between light and surface plasmons.

Phase modulation As for the intensity modulation, angle of incidence and wavelength are fixed and the phase shift of the reflected light wave is measured and represents the sensor output.

The sensing performances of a SPR device are described by three parameters:

Bulk sensitivity S_∞ , is defined by the derivative of the sensor output Y with respect to the refractive index n_s variation at the surface: $S_\infty = \frac{\partial Y}{\partial n_s}$;

Resolution represents the minimum refractive index variation that the sensor can resolve and it depends on the accuracy of the Y measurement. It is defined by the ratio of the Y accuracy to the sensitivity S;

Local sensitivity S_0, also called surface sensibility, is defined by the second derivative of the sensor output Y with respect to the refractive index variation and to the thickness t of a dielectric layer of refractive index n_s that is added on the surface, for $t \to 0$:

$$S_0 = \left.\frac{\partial^2 Y}{\partial n_s \partial t}\right|_{t=0} \cong \frac{1}{\Delta n_s} \cdot \left.\frac{\partial Y}{\partial t}\right|_{t=0} . \tag{2.2}$$

S_0 evaluates the sensor's response when only a thin surface layer changes the refractive index by Δn_s whereas S_∞ quantifies the sensor response when the refractive index of all the environment around changes.

In order to achieve a proper bio-sensor, refractive index transducer has to be properly functionalized, that means binding to its surface suitable bioreceptors that can specifically interact with a desired analyte biomolecule. When exposed to the solutions with the analyte molecules, these will conjugate specifically to the bioreceptors and so the refractive index at the interface will increase. Non-specific binding events could also occur thus generating a false signal so a protection against these aspecific contributions is necessary.

A properly bio-functionalized SPR device is called an *affinity biosensor* and it relies on the binding affinity between receptor and analyte, and this dramatically influences the selectivity of the biosensor. Therefore, the selectivity of the target-ligand molecules impacts on the performances of the biosensor which can be described by the sensitivity and the limit of detection (LoD), which represents the lowest concentration of analyte that could be revealed [47].

2.3 Prism-coupling SPR biosensor

The prism-based sensor is the most commonly used amongst the SPR techniques for real-time monitoring of biorecognition events [49, 50]. It is sketched in figure 2.1 and it consists of a thin gold film of about 50 nm deposited on a high refractive index glass prism in Kretschman configuration. In the wavelength modulation of the Attenuated Total Reflectance (ATR) method presented in figure, a polychromatic light beam impinges the gold film with a fixed incidence angle and thus E-SPs are excited and observed as a dip in the reflectance spectrum. The matching condition for the SPR is fullfilled when the wavenumbers of the light and the E-SP are equal and is expressed by

$$\frac{2\pi}{\lambda} n_{prism} \sin\theta = Re(\beta) \tag{2.3}$$

where the left member represents the in-plane projection of k vector of the light in inside the prism.

When biomolecules bind to the gold/medium interface, the matching condition changes and thus a shift of the minimum reflectance is observed as in figure 2.1b. Therefore, the shift $\Delta\lambda$ represents then the signal output of the biosensor.

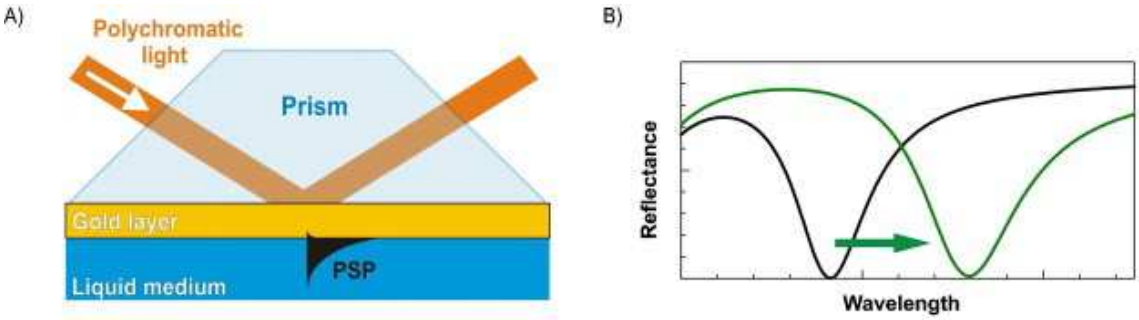

Figure 2.1: The scheme of a prism-coupling SPR biosensor. (A) E-SP excitation by ATR method in Kretschmann configuration. (B) Two reflectance spectra corrispondig to two different values of the refractive index of the adjacent medium. The two dips correspond to two different SPR matching conditions.

Prism-coupled sensor with intensity interrogation In SPR sensors with intensity modulation both incidence angle and wavelength are fixed. An innovative approach to enhance sensitivity of this configuration was reported by Sepúvleda et al. [51]. They obtained threefold enhancement of the sensitivity with respect to the common SPR one by combining plasmonic properties with the magneto-optic activity of magnetic materials and they reported a resolution of 5×10^{-6} Refractive Index Unit(RIU). Intensity interrogation was also widely employed for biological sensing of small molecules. Nelson et al. [52] reported lable-free detection of oligonucleotides of 18 bases down to a concentration of 10 nM, corresponding to a resolution of 10^{-5} RIU. Interaction between streptavidin (SA) protein and biotinylated oligonucleotides was investigated and SA concentration lower than 1 pg were detected by Shumaker-Parry et al. [53]. A further improvement of this technique was reported by Piliarik et al. [54] by employing a spatial distribution of Au films ad the polarization contrast. Oligonucleotides composed by 23 basis were detected down to 100 pM concentrations.

Prism-coupled sensor with wavelength and angle interrogation In 1990 a prism-coupled biosensor based on angular interrogation was developed and commercialized by Biacore© reporting a resolution of 10^{-7} RIU. Dosálek and co-workers developed a wavelength division multiplexing SPR sensor to get better performances. Here, multiple E-SP excitation were obtained in different areas of the metallic film thus generating multiple dips in the reflectance spectrum. Thanks to this technique they achieved a resolution of $\sim 10^{-6}$ RIU[55]. Ultra-high sensing performances were achieved also by the excitation of long range Surface Plasmon Polaritons (SPP) in the work of Nenninger and Slavík [56, 57]. They reported respectively a bulk sensitivity of $5.7 \cdot 10^4 \frac{\text{nm}}{\text{RIU}}$ and a resolution of $2.5 \cdot 10^{-8}$ RIU.

2.4 NanoHole Array based biosensor

As introduced in section 1.5 a E-SP could be excited without the prism-coupling if there is an periodic grating. The momentum gap to reach the SPR condition is provided then by the reciprocal lattice of the periodic grating. Also in this case, the coupling condition between the impinging light and the E-SP for the SPR depends on the refractive index of the adjacent medium, thus allowing to develop refractometric biosensors. A sinusoidal grating with 500 nm period and 40 nm peak-to-valley amplitude was employed by Meneghello et al. [58] with angular modulation to excite SPP on the gold surface. Thanks to the conical mounting (cf. fig. 1.8) a sensitivity up to 800°/RIU was achieved.

A grating-coupling system widely employed is given by the patterning of a metalic film with a ordered NanoHole Array (o-NHA) (cf. sec 1.5). When the coupling condition between the E-SP and the light is fulfilled, the incident electromagnetic field is localized near the o-NHA surface. Therefore, the o-NHA was also employed as refractometric sensor utilizing the same detection principle of the prism-coupled ones [59]. Even if with the o-NHA both transmission and reflection interrogations are possible, the most commonly used is the transmission one, which allows to exploit the extraordinary optical transmission (EOT) property [60].

The very first report on EOT sensing was from Brolo et al. [61] and a 400 $\frac{\text{nm}}{\text{RIU}}$ sensitivity was found. NanoHole Array (NHA) were fabricated by Focused Ion Beam (FIB) with 200 nm hole diameter, $\sim$ 600 nm periodicity and 100 nm gold thickness. An optical setup with collinear geometry was used for transmittance measurements at normal incidence and it represented an important semplification with respect to the measurements in Kretschmann configuration. Since then EOT based device have been widely use for the lable-free detection of biomolecules.

Monteiro et al. [62] described the effect of the periodicity on the sensing performances of EOT sensor with squared lattice of circular holes and the maximum sensitivity is reported to be 463 $\frac{\text{nm}}{\text{RIU}}$ with a resolution of 4×10^{-4} RIU (NHA by FIB milling, period $a = 455\,\text{nm}$, diameter $d = 200\,\text{nm}$, Au height $h_{Au} = 100\,\text{nm}$).

Both wavelength and intensity interrogation are employed with the co-linear transmission optical arrangement. Cetin et al. [63] developed a handheld SPR imaging device based on intensity interrogation and a limit of detection of 3.9 μg/mL of Immunoglobulin G was reached with a sensitivity of 612 nm/RIU and a resolution of $\sim 4 \times 10^{-3}$ RIU (NHA by UV lithography, squared lattice with $a = 600\,\text{nm}$, circular holes with $d = 200\,\text{nm}$ and $h_{Au} = 120\,\text{nm}$).
Briscoe et al. [64] employed the intensity interrogation and the detection of microcystin-leucine-arginine (MC-LR) in water was achieved with a LoD of 10 pM (NHA by FIB milling, squared lattice with $a = 500\,\text{nm}$, circular holes with $d = 250\,\text{nm}$ and $h_{Au} = 100\,\text{nm}$).

Better resolution was achieved by Jia et al. [65] with the wavelength interrogation technique and they obtained a bulk sensitivity of 522 nm/RIU and a resolution of 2×10^{-5} RIU (NHA by Electron Beam Lithography (EBL), squared lattice with $a = 600\,\text{nm}$, circular holes with $d = 200\,\text{nm}$ and $h_{Au} = 100\,\text{nm}$).
Wavelength modulation was employed also by S. Cho et al. [66] who demonstrated the detection of malaria pathogen through antibody-antigen interaction and a sensitivity of 378 nm/RIU was reported (NHA by FIB, squared lattice with $a = 500\,\text{nm}$, circular holes with $d = 200\,\text{nm}$, $h_{Au} = 100\,\text{nm}$).

The NHA sensing platforms reported so far were developed on a planar and transparent substrates and the liquids with target molecules flowed over the NHA sample. An enhancement of the binding events and so of the sensing performances was achieved by developing free-standing NHA. Therefore, target solution can be forced to flow through the NHA thanks to the integration of NHA with nanofluidics and so the adsorption kinetics of the target molecules is enhanced. Eftekhari et al. [67] demonstrated that the flow-through configuration yields a faster response and they reported 324 nm/RIU sensitivity (NHA by FIB, square lattice with $a = 500\,\text{nm}$, circular holes with $d = 300\,\text{nm}$, $h_{Au} = 100\,\text{nm}$). Yanik et al. [68], instead, reported the direct detection of viruses down to concentrasions of 10^6 plaque $-$ forming units(PFU)/mL (NHA by EBL, squared lattice with $a = 600\,\text{nm}$, circular holes with $d = 200\,\text{nm}$, $h_{Au} = 100\,\text{nm}$).

Another technique to enhance the sensing performances of the NHA is presented by Zhang et al. [69] and consists in a thermal annealing at 600°C in Ar atmosphere. The

roughness of the gold surface is heavily reduced thus enhancing the EOT response and increasing the surface sensitivity ~ 3 times (NHA by EBL, square lattice with $a = 500\,\text{nm}$, circular holes with $d = 150\,\text{nm}$, $h_{Au} = 100\,\text{nm}$).

Even if gold is the most commonly used material for biosensing, the development of alternative plasmonic materials [31] leaded to their application for sensing platforms. Canalejas-Tejero et al. [70] developed an Aluminum NHA and they reported a bulk sensitivity of about 500 nm/RIU (NHA by EBL, triangular lattice with $a = 500\,\text{nm}$, circular holes with $d = 220\,\text{nm}$, $h_{Al} = 100\,\text{nm}$).

Besides the direct detection of target analytes, the NHA platforms were also employed in molecular spectroscopy. In particular, NHA represent a promising platform for Surface Enhancement Raman Spectroscopy (SERS) due to the electric field enhancement that occurs at the gold surface when SPR condition is fullfilled and due to the tunability EOT property [71].

The NHA reported above were synthesized by Electron Beam Lithography, Focused Ion Beam or UV lithography and these techniques allow finely tune the morphology and thus the EOT property. Other techniques that offer tunability and also the possibility of a cost-effective NHA synthesis are the Nanosphere Lithography (NSL) and Sparse Colloidal Lithography (SCL), and both will be employed in the present work.

2.5 Localized Surface Plasmon Resonance based biosensor

With respect to the E-SP based sensors that rely on prism or grating coupling, the Localized Surface Plasmons (L-SP) can be excited directly by light. Therefore, if white light impinges a three-dimensionally confined plasmonic nanostructures, Localized Surface Plasmon Resonance will occur at a specific wavelength λ_{LSPR} that depends on the morphology, on the composition and on the adjacent dielectric medium. By changing morphology and composition the λ_{LSPR} measured in air can be finely tuned in the Vis-NIR range [3]. The figure 2.2 presents extinction spectra of confined silver nanostructures with different shapes and sizes. The decay length l_d of the evanescent electric field that arises

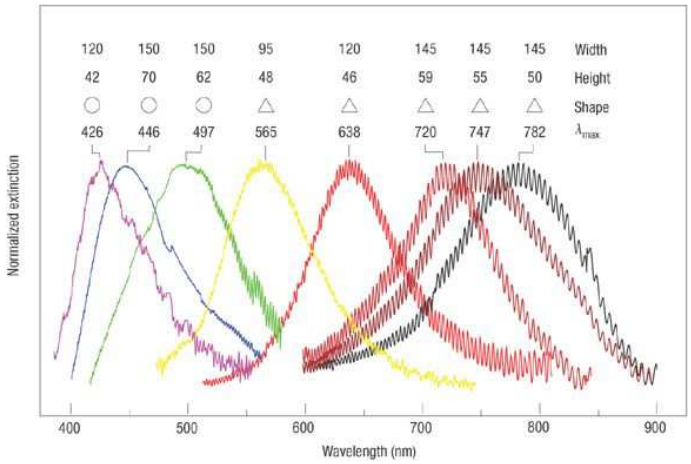

Figure 2.2: Size and shape dependance of LSPR peak of silver nanostructures. Copyrighted by Anker et al. [3].

on the surface when plasmonic resonance occurs is roughly one order of magnitude smaller in the case of the L-SP than the one of the E-SP ($l_d^{E-SP} \sim 100\,\text{nm}$) [72]. Therefore, the electric field in the case of L-SP is confined in smaller volumes than the E-SP case and

this grants to the LSPR-based sensors a huge sensitivity to small changes in the refractive index of thin films on the nanostrucutre surface [73].

Sensing performance of ordered and disordered arrays of nanostructures are widely reported in the literature and other nanostructures are mostly obtained by cost-effective techniques such colloidal lithography or chemical synthesis [74].

Joshi et al. [28] achieved a sensitivity of 647 nm/RIU employing dispersed gold nanoprisms with an edge length of 28 nm. From biosensing tests with the Biotin-Streptavidin a limit of detection of 1 pM was reached.
The sensing performances of gold nanoring obtained by colloidal lithography and integrated on a microfluidic chip were investigated by Huang et al. [75]. Gold nanorigs with internal and external diameter, respectively, 100 and 130 nm and thickness 50 nm showed a bulk sensitivity of 350 nm/RIU.
Fancier nanostructures are also reported. Gold nano-crosses with LSPR in the IR range (~ 1400 nm) were developed by EBL by Rodríguez-Fortuño [76] and they showed a sensitivity of 500 nm/RIU. Sparsed gold nano-stars, were synthesized by Dondapati et al. [77] and were tested for the Biotin-SA binding detection obtaining a 0.1 nM LoD.

Au-Ag alloy Semi-NanoShell Array (SNSA) were synthesized by Russo et al. [78] by NSL and consisted of a metallic cap deposited on the top of polystyrene (PS) nanospheres. Due to the short interdistance, highly interacting semishels were obtained and a high field enhancement was achieved at the shell edges. A bulk sensitivity of 405 nm/RIU and a LoD of 30 pM with Biotin-SA were reported.

The LSPR devices presented by now are interrogated with a simple co-linear optical setup. A high improvement in the sensing performances is claimed by Maccaferri et al. [79] by exploiting the control of the phase of light in Nichel magnetoplasmonic nanodisks with 100 nm diameter and 30 nm thickness.

Besides the sensing performance evaluations, LSPR based sensors are widely used for the detection of chemical and biological species not only in medical diagnostics but also, for example, in food safety or enviromental monitoring research [73].

MicroRNA are short noncoding oligonucleotides whose level in blood could indicate a specific disease and revealing very low concentrations leads to a early diagnosis. Joshi et al. [80] reported the detection in plasma of microRNA related to pancreatic cancer. Gold nanoprisms were chemically sinthesized, functionalized with the complementary RNA strand and thus a LoD of 30 fM was found for the 21-base microRNA.
Aćimović et al. [81] developed gold nanorods with in plane dimensions of 200×105 nm and thickness of 80 nm by EBL and integraded the plasmonic platform into microfluidic lab-on-chip device. Specific antibodies were bound to the surface of nanorods and then cancer markers, human α-feto-protein and prostate specific antiged, were detected down to a concentration of 0.5 ng/mL.

Guerreiro et al. [82] investigated the molecule-protein interaction with gold nanodisks obtained from Sparse Colloidal Lithography with diameter of 100 nm and height of 20 nm. The α-amylase protein, a glycoprotein with $MW = 53.5$ kDa, was employed as bioreceptor for the detection of the pentagalloyl glucose (PGG), a small molecule with $MW = 940$ Da, and a LoD of 0.5 μM was reported.

2.6 Functionalization methods and conclusion

There are two main challanges in plasmonic biosensing research. Firstly, nanostructures and interrogation strategies could be improved in order to achieve better sensitivities to refractive index variations. Secondly, functionalization protocols are also fundamental to

obtain a specific and selective biosensor.

On one side bioreceptors must be bound to the plasmonic surface and Au/Ag devices take advantage of the strong bound that the thiol group -SH forms with Au or Ag surfaces [83]. Thiol-terminated bioreceptors can be directly self-assembled on the plasmonic surface or they can be bound to previously self-assembled thiols by cross-linking reactions. For example, DNA/RNA can be engineered to obtain thiol terminated aptamers [80] while antibodies have an internal disulfide bond, which can be reduced thus obtaining an active native thiol on each half [84]. Both oligonucleotides and antibodies have a high selectivity to bind to respectively, the complementary oligo and the corresponding antigen.

On the other side, in order to avoid biofouling effects all the surfaces of the plasmonic devices must be properly protected against aspecific binding, not only the metallic surfaces but also the dielectric ones that are exposed, i.e., the substrate silica. Oliverio et al. [85] reported the most comonly employed protection strategies such as silanization of the dielectric surface, Polyethylene Glycol (PEG) grafting or Bovine Serum Albumine (BSA) protein exposure.

In this work, different nanostructures will be developed and employed for biosensing experiments. More specifically in chapter 6 biosensing measurements with the benchmark protocol Biotin-Streptavidin will be presented, while in chapter 7 the detection of miRNA will be reported.

In conclusion, an analytical model for the sensor response to refractive index variations is presented. The wavelength interrogation will be used across all the present work, so the signal output of the sensor will consist in a variation of the resonance wavelength $\Delta\lambda$. Therefore the signal output of a sensor embedded in an environment with refractive index n_{env}, when a small layer of thickness t adjacent to its surface changes its refractive index to n_s, can be described by the following equation [72]:

$$\Delta\lambda = m(n_s - n_{env})\left(1 - e^{-2t/l_d}\right). \tag{2.4}$$

By remembering the definition from equation 2.2, the local sensitivity S_0 can be computed

$$S_0 = \left.\frac{\partial^2\lambda(t, n_s)}{\partial n_s \partial t}\right|_{t=0} = \frac{2m}{l_d}. \tag{2.5}$$

The bulk sensitivity, instead, was defined by $S_\infty = \frac{\partial Y}{\partial n_s}$ where $t \to \infty$ since the refractive index variation is considered in all the surrounding environment. By using equation 2.4 is obtained:

$$S_\infty = \lim_{t\to\infty}\left(\frac{\partial\lambda(t, n_s)}{\partial n_s}\right) = m. \tag{2.6}$$

Therefore, the m parameter in equation 2.4 represents the bulk sensitivity and morever a theoretical relation is obtained between bulk and local sensitivity that relies on the decay length l_d of the localized electric field:

$$S_0 = \frac{2 \cdot S_\infty}{l_d}. \tag{2.7}$$

3 Nanofabrication techniques

In this chapter, the techniques used to produce the plasmonic nanostructures will be presented. As showed in chapter 1, the plasmonic properties of nanostructures strongly depend on both surrounding dielectric medium and geometrical parameters. On one side, synthesis techniques that allow to tune dimensional parameters of plasmonic nanostructures are necessary. On the other side, for the purpose of this work, that is producing high-sensitivity high-specificity biosensors using plasmonic nanostructures, a cost-effective way to produce such devices is also needed.

In this work two bottom-up nanofabrication techniques were employed, both relying on the colloidal lithography in which a monolayer mask of monodispersed polystyrene (PS) nanoparticles self-organizes on a flat surface. One one side, ordered nanostructures with an hexagonal symmetry were obtained by the Nanosphere Lithography (NSL) where uncharged polystyrene nanoparticles self-assemble in a hexagonal close-packed motif. One the other side, disordered patterns of nanostructures were developed by Sparse Colloidal Lithography (SCL) where charged polystyrene nanospheres were utilized. Thank to these techniques, planar arrays of nanostructures were synthesized on different substrates (i.e., silicon wafer, silica and Soda Lime Glass (SLG)), covering areas up to a couple of cm^2.

Each of the two techniques introduced above were employed to produce two kinds of nanostructures, whose morphology could be finely tuned during the fabrication, a 3D confined one and a 1D confined one. Thank to NSL, the following nanostructures were obtained: the NanoPrisms Array (NPA), which consists of a honeycomb lattice of triangular-shaped nanoprisms, and the ordered NanoHole Array (o-NHA), which consists of a metallic thin film patterned with an hexagonal array of subwavelength holes. Analogously, by SCL two other geometries were produced: the disordered NanoHole Array (d-NHA), similar to the o-NHA but with a disordered pattern of holes in place of the hexagonal one, and the NanoDisk Array (NDA), which consists of a disordered array of circular-shaped confined nanostructures.

The NPA and the NDA exhibit the Localized Surface Plasmon Resonance (LSPR) property, which is common to the 3D confined plasmonic nanostructures whereas both the NanoHole Array (NHA), the ordered and the disordered one, sustain Extended Surface Plasmons (E-SP).

Firstly, the NSL technique will be presented and how the NPA and the o-NHA can be produced and, secondly, the SCL employed for the NDA and the d-NHA will be described. The possibility of finely tuning the morphology, and thus the plasmonic behaviour, of the nanostructures above will be also stressed.

3.1 Nanosphere Lithography

Nanosphere Lithography is a powerfull fabrication technique to produce wide and well-ordered nanoparticle arrays in a high-throughput and cost-effective way and controlling finely shape, size and interparticle spacing of the nanostructures. Named firstly "natural lithography " and described by Deckman [86], this technique was then renamed Nano Sphere Lithography, developed and operationally described in a more systematic way by

Van Duyne et al. [13, 14].

To produce any nanostructure by NSL, first a self-assembled monolayer (or mask) is formed from size-monodisperse polystyrene (PS) nanospheres (NS) of diameter a, in the range 100 nm - 1 μm. Thus, a monolayered hexagonally close-packed pattern of spheres crystallizes on a substrate. Large well-ordered masks, of the order of 1 cm^2, can be easily produced. However a variety of defects can arise due to nanospheres diameter polydispersity and the presence of vacancies, slip dislocations and polycrystalline domains. Therefore defect-free domain size is reduced in the 10-100 μm range [87]. Usually spheres are deposited on the substrate by spin-coating or drop-coating, but in the present work another way of self-assembling will be used and described.

Once a mask is formed on a substrate, the NPA is synthesized by directly depositing the metal species through the mask. For the o-NHA, instead, before metallic deposition it is first necessary an etching process that shrinks the spheres' diameter leaving unaltered the lattice and interparticle distances. A detailed description of the NSL process will be now given.

3.1.1 Self-assembled monolayer of polystyrene nanospheres

Cleaning of substrates

Three type of substrates were used (with a typical side of 1-2 cm): Soda Lime Glass (SLG), highly-pure *HSQ 300* silica (SiO_2) and monocrystalline silicon (Si). In order to get a high degree of order and as few defects as possible in the nanosphere mask, substrates surfaces should have no impurities. For this purpose all the used substrates firstly went through two cleaning processes.

The first, *acid piranha*, consists in the treatment of the substrates in a 3:1 solution of sulfuric acid (H_2SO_4) and hydrogen peroxide (H_2O_2) for 1 hour at the temperature of 90°C. Since it is a strong oxidizing agent, this step removed most of the organic matter impurities from the surfaces and made them highly hydrophilic.

After thoroughly rinsing the substrates with Milli-Q water (18.2 $M\Omega \cdot cm$ resistivity), a *basic piranha* has been carried out, which consists in a basic 3:1 solution of ammonium hydroxide (NH_4OH) and hydrogen peroxide. Substrates were treated in this solution for 20 minutes at the temperature of 90°C to further increase their hydrophilicity.

Mask self-assembling

The deposition of the nanospheres on the substrate was based on the work of Schatz [88]. Polystyrene nanospheres with the same nominal diameters a were used for the mask assembly and a colloidal suspension of nanospheres in water and alcohol was first preparated. A small amount of nanoparticle solution was then deposited on the substrate and this was dipped mechanically into a Petri dish filled with Milli-Q water. The floating nanospheres formed a self-assembled monolayer on the surface thanks to the meniscus between the alcoholic dispersion and the water. A second substrate was then dipped and the monolayer was collected manually and left to dry. The figure 3.1 summarizes the steps of the mask formation. The samples were then dried at room temperature with relative humidity of about 75%. As the solvent evaporates, the nanospheres, which are free to move on the surface of the substrate, are driven by capillary forces that gather them together and thus a hexagonally close-packed pattern is formed (cf. fig. 3.2a). Figure 3.2b shows a FE-SEM image of masks of PS nanospheres of 522 nm diameter.

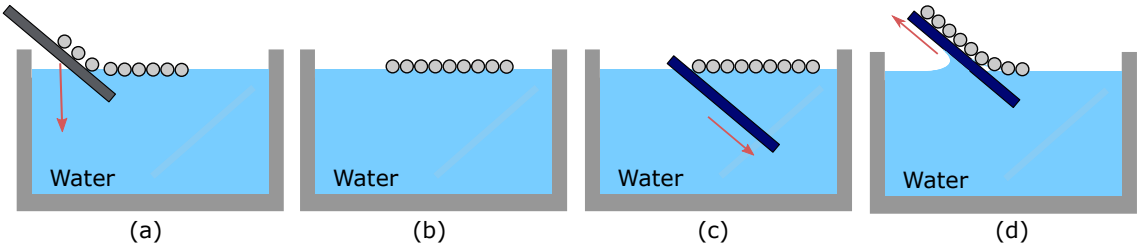

Figure 3.1: The image summarizes the formation of the ordered monolayer: (a) a substrate with a droplet of nanoparticle solution deposited on is dipped; (b) nanospheres self-assemble into a well-ordered monolayer on the water surface during the dipping; (c) a second sample is immersed beneath the monolayer and (d) the nanosphere mask is then collected manually.

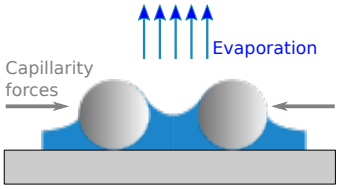

(a)

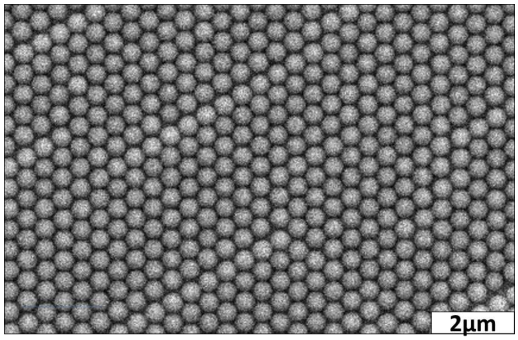

(b)

Figure 3.2: **(a)** Drying step, while capillarity forces drive the monolayer to a close-packed pattern. **(b)** SEM image of a self-assembled mask of nanospheres with 522 nm diameter.

3.1.2 NanoPrisms Array

At this point, if a metal is deposited through the PS mask, a honeycomb array of triangularly shaped nanoparticles can be created. In fact, during the deposition metal atoms reach the substrate only through the interstices between spheres and thus, removing the mask, triangular nanoprisms are produced (figure 3.3) [14, 89]. It can be shown that interparticle distance d between triangles is linked to the nanospheres diameter a by

$$d = \frac{1}{\sqrt{3}}a. \tag{3.1}$$

Moreover, it can be pointed out that the perpendicular bisector of the nanotriangle (b) and the width L are correlated to the diameter a of the nanosphere [14]:

$$b = \frac{3}{2}\left(\sqrt{3} - 1 - \frac{1}{\sqrt{3}}\right)a \approx 0.233a \approx \frac{1}{4}a \qquad L = (2 - \sqrt{3})a \tag{3.2}$$

Therefore, the NPA were obtained by thermal evaporation of metal (cf. section 3.1.4), that also allowed to control the height of the nanostructures. To obtain plasmonic samples, first a 2 nm of Cr, which serves as an adhesion layer, then the gold are evaporated. It is clear then how geometrical dimensions, and thus the plasmonic properties, of the NPA could be simply tuned thanks to the Nanosphere Lithography technique by changing the diameter a of the PS nanospheres, which controls L and d, and the height of the metallic layer.

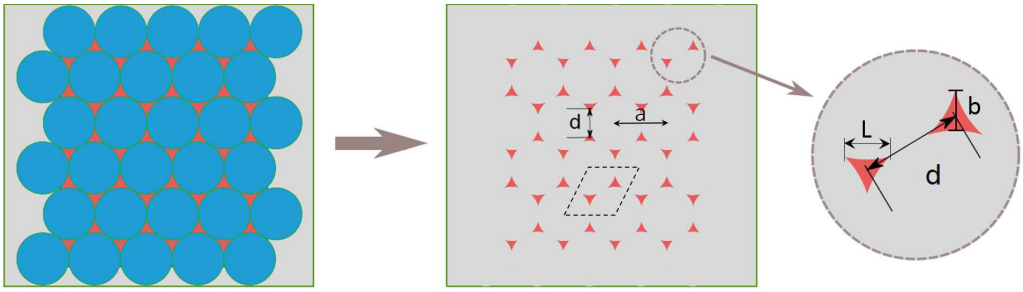

Figure 3.3: NanoPrisms Array from NSL method. First metal is deposided (left) then mask is removed (right). The dashed parallelogram represents the unit cell of the ordered array of nanoprisms. The main geometrical parameters are showed: a is the periodicity, d the distance between the two nanoprisms in the unit cell and b the height of the triangular shape and L the width.

3.1.3 Reactive Ion Etching

Description of the RIE process

In order to produce nanohole arrays using NS masks they have to go through another process, that shrinks polystyrene nanospheres leaving unchanged the lattice structure and thus creating the negative mask for the nanohole. Such process should be able to erode the nanospheres reducing their diameter with a controlled rate without altering periodicity of the initial lattice, and thus creating an ordered non-close-packed NS array. Reactive Ion Etching (RIE) [90] is the process that best fit this purpose. It consists in a dry ion-assisted chemical etching process, which uses a chemically reactive plasma to remove material deposited on a substrate. High-energy ions from the plasma, generated under low pressure, hit the sample surface and react with it. A typical RIE system consists of a cylindrical vacuum chamber, with a wafer plate to hold substrates situated in the bottom part of the chamber. The plate is electrically isolated from the rest of the chamber, which is usually grounded. Input valve for the gases used for the etching is situated in the top of the chamber while products from etching exit to the vacuum pump through an inlet situated in the bottom. Etching process is strongly influenced by the type and the amount of the gases employed, and their choice depends on what material has to be etched.

First, vacuum is created in the chamber, whose pressure is typically maintained in a range between 10^{-3}-10^{-1} mbar. As the gas flows into the chamber, a plasma is created by the application of a radio-frequency (RF) electromagnetic field to the plate. The ionizing field is tipically set to a frequency of 13.56 MHz and it is applied at a power of a few tens Watts. After the ignition the plate acquires a negative charge and positive ions are driven towards the substrate by the electrostatic field thus generated. On one side, colliding ions can chemically react with the material of the samples, erode it and finally volatile byproducts are desorbed. On the other side, an ion with low chemical reactivity can sputter, and thus physically etch, parts of the material by transfering kinetic energy. All these products diffuse away from the sample and are collected by the vacuum pump. The different steps are illustrated in figure 3.4.

Since reactive ions collide perpendicularly the sample, driven by the electric field, the process has a very anisotropic profile and the material is etched mainly in a vertical direction.

Etching process depends on many parameters, such as chamber pressure, gas flows and RF power and choice of these parameters had to be optimized for synthesis of the o-NHA to be optimized.

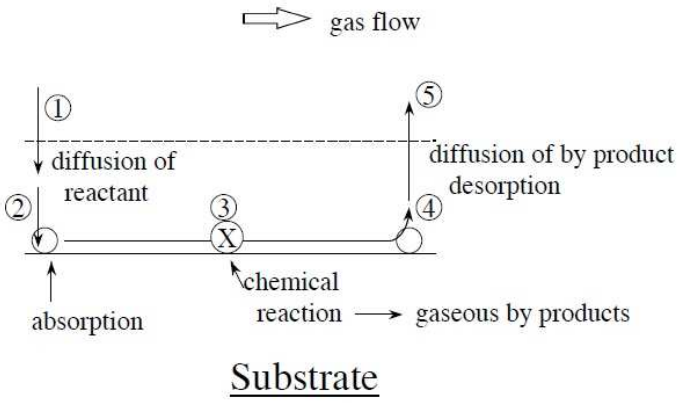

Figure 3.4: Schematic representation of the RIE process

RIE on PS nanospheres mask

RIE process is largely used for the production of nanohole arrays by NSL [71, 91]. Here a mixture of two gases was employed: oxygen (O_2) is the chemical reactant while Argon (Ar), which is chemically inert, is used for physical etching. Parameters have been studied empirically and optimal values were found in order to make the etching process stable and reproducible. Two different regimes of etching are possible at low-pressure ($\sim 0.009\,\text{mbar}$) and at high pressure ($\sim 0.15\,\text{mbar}$), as showed in figure 3.5. The low-pressure etching has less gas flow and ions can easily difuse towards the sample driven vertically by the electric field. Thus an anisotropic erosion on vertical direction is performed. On the other side, a higher gas flow leads to a more isotropic etching of the spheres.

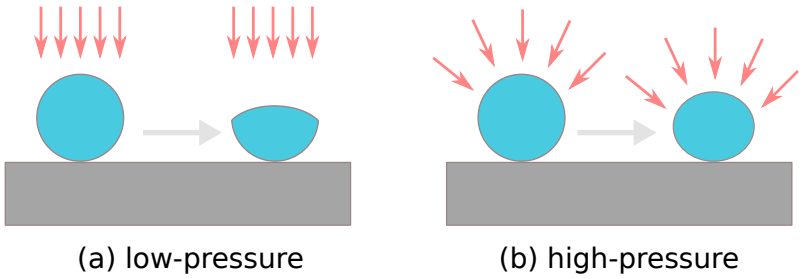

Figure 3.5: Scheme of the PS Nanosphere shape after low-pressure ($\sim 0.009\,\text{mbar}$) (a) and high-pressure ($\sim 0.15\,\text{mbar}$) (b) RIE process.

For the etching of masks for the o-NHA synthesis the high-pressure regime has been used with the optimized parameters from table 3.1.

Pressure	O_2 flux	Ar flux	V Bias	Power
$155 \cdot 10^{-3}$ mbar	9.2 sccm	3.6 sccm	119 V	35 W

Table 3.1: Optimal parameters for high-pressure RIE process used in the present work.

Once these parameters were fixed, etching time was the only free parameter left that allowed to finely control the diameter of spheres, and thus the diameter of the nanoholes. For this purpose, tests were carried out for different etching time and masks were analized with Scanning Electron Microscopy (SEM) to get average diameter. Using such data it was possible to draw a calibration between etching time and final diameter. Attention must be

paid to avoid collapse of nanospheres, caused by excessive etching, by restricting the RIE process to a final diameter d greater than half of the initial one.

Figure 3.6 shows the FE-SEM images of the PS masks that went through RIE process with different processing times.

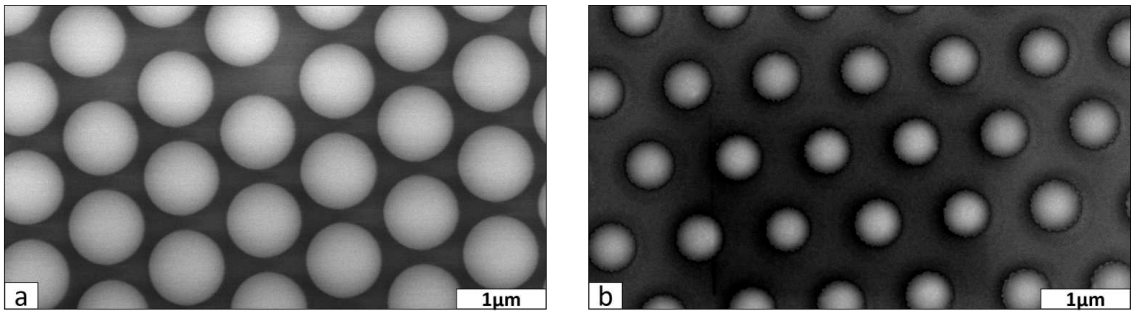

Figure 3.6: Non-closed-packed NS arrays after going through etching processes with different times: (a) 6 minutes, (b) 12 minutes. The initial PS nanosphere diameter was 522 nm.

3.1.4 Metals deposition: Thermal Evaporation and Magnetron Sputtering

In order to obtain the nanostructures, metal has to be deposited through the PS nanosphere mask, either etched or not. In this work two different techniques were employed for the metal deposition, the thermal evaporation and the magnetron sputtering, which both belong to the family of physcal vapor depositions (PVD). Both techniques allow to deposit mono-elemental thin layers, i.e., Au, Ag, Ti and Cr, by finely controlling the thickness from a couple of nanometers up to hundreds of nanometers, whereas layers of multi-elemental materials, such as silica (SiO_2) or alloys, can be obtained only by magnetron sputtering.

Thermal Evaporation

The thermal evaporation relies in heating a material, called target, above its evaporation temperature. Target is put in a crucible and a high current flows through it and thus the crucible and the target are heated due to the Joule effect. Once the evaporation temperature is reached atoms leave the target and travel towards the sample. A low pressure, i.e, 1×10^{-5} mbar, is needed in order to ensure that the mean free path of the atoms is greater than the distance between target and sample thus allowing to the atoms to reach the substrate without interacting with other atoms.

The atoms reaching the sample condensate and thus the metallic layer is formed. Thanks to a Quartz Crystal Microbalance (QCM) which is mounted inside the vacuum chamber and previously calibrated, the thickess of the deposited metal can be monitored in real-time and thus finely controlled. Once the threshold current that is necessary to start the evaporation for a specific element is reached, the deposition time represents the free parameter of the process. The typical threshold currents needed to start the evaporation process range from 120 A up to 200 A and depend on the melting temperatures of each element.

Thanks to the two crucibles present inside the vacuum chamber, at most two elements could be evaporated in sequence and thus multi-layered nanostructures could be synthesized. In figure 3.7a the scheme of a thermal evaporation set-up is presented.

Magnetron Sputtering

The sputtering process consist in the physical removal of material from a target (metal or insulator) by the collision of inert atoms (e.g Argon). Atoms from an ionized gas strike the target eroding it and atoms from it are ejected in all directions due to the transfer of kinetic energy to target atoms [92]. The last ones reach the sample through diffusion in the previously evacuated chamber and there start to grow by depositing the desired metallic layer.

The magnetron sputtering system consists of a vacuum chamber containing the target and a sample holder, both connected in the same electrical circuit. A high negative DC voltage is applied to the target holder, which is the cathode, while the sample holder is grounded, representing the anode. Once vacuum is created (pressure $\approx 3 \cdot 10^{-6}$mbar), gas flows inside the chamber through an inlet reaching higher pressures of work of order of 10^{-3}mbar. Here Argon was used to create the plasma for target erosion, because it is inert and does not react either with the target or with the growing layer. The high electric field ignites the plasma ionizing the Argon atoms and drives them towards the cathode where the target is situated. In addition to the electric field, a magnetic field is present thanks to magnetrons situated inside the target holder. Such field increases plasma density and confines it in a region near the target, thus speeding up the erosion process and improving sputtering efficiency.

In the sputtering process neutral precursors are extracted from the target due to the physical erosion and these aren't trapped by electric and magnetic fields but they difuse and collide with other precursors or atoms in the atmosphere. The collision rate during the diffusion is strongly dependent on the chamber pressure given by the gas flow. On one hand, collision rate decreases in case of lower pressures making the sputtering less efficient since there are less ionized atoms to hit the target. On the other hand, higher pressures increase both the erosion and the collision rates leading to a less efficient deposition on the sample since the sputtered precursors are deflected and few of them reach it. For these reasons pressure of work is usually of order of $10^{-3} - 10^{-2}$ mbar.

The figure 3.7 shows the scheme of a single-target sputtering system. The one used in this work has three target holders and each of them can ignite and confine its own plasma. Therefore, at most three elements can be deposited in the same process. On one hand, metal alloys can be deposited by ingniting plasmas and co-sputtering multiple metals at the same time. On the other hand, multi-layer deposition is possible by sputtering consecutively different metals.

As in the case of the RIE process, first optimal parameters were found for the power and the voltage applied to each target and the pressure of the chamber. Then, the only free parameter is the sputtering time and calibration were done to find the deposition rate for each target and then control finely the thickness of the deposited layers.

Due to the different geometry of the two deposition set-ups, small differences may arise when metal is deposited through similar masks. The thermal evaporation crucible can be considered as a divergent point source since its dimensions (circular well with 1 cm diameter) are much smaller than the distance between the crucible itself and the substrate ($\sim$ 25 cm). Therefore, the divergence of the source produces a shadow effect, and the footprint left by a an obstacle is larger than the obstacle itself. On the contrary, the source in the sputtering process is a plasma ring with $\sim$ 5 cm diameter and samples are placed only $\sim$ 10 cm far from the target. This ensures the uniformity of the sputtering rate deposition and produces an opposite effect with respect to the evaporation. Therefore, depositing through an obstacle yields a footprint smaller than the obstacle itself. The figure 3.8 highlights this difference between the thermal evaporation and the magnetron

sputtering.

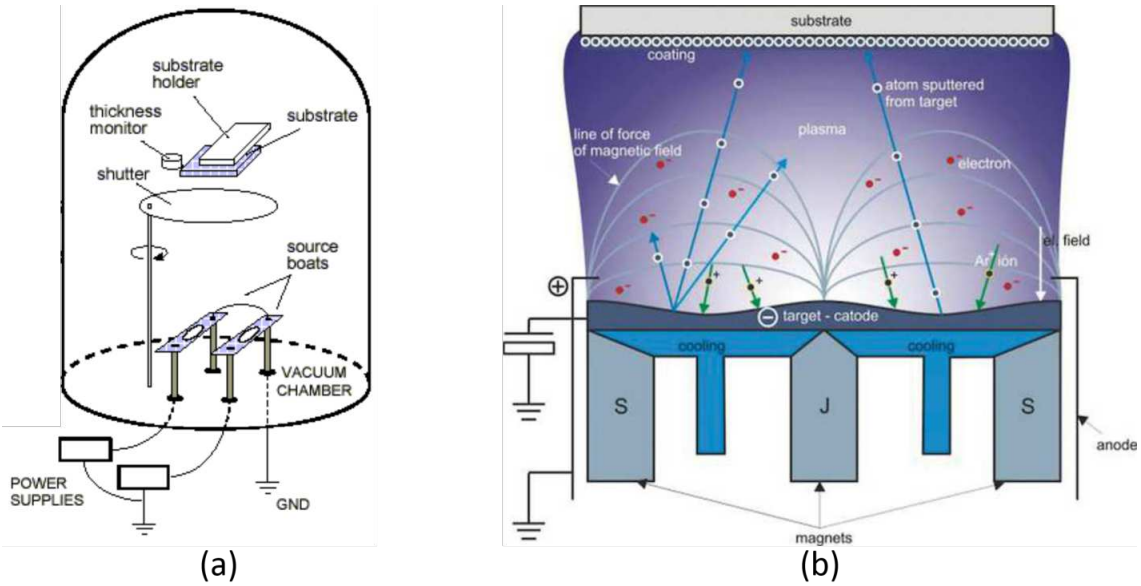

Figure 3.7: The deposition set-ups are schematically depicted: (a) thermal evaporation chamber with two crucibles where pellets of two different elements could be placed; (b) magnetron sputtering scheme with one plasma torch (in this work a set-up with 3 torches for three different targes has been employed).

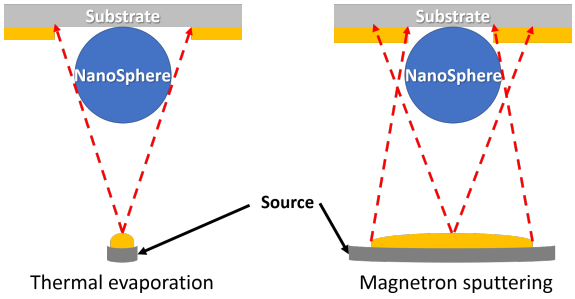

Figure 3.8: The difference between the precursor sources for thermal evaporation and magnetron sputtering set-ups is depicted. The distances and the dimensions are not to scale.

3.1.5 Ordered NanoHole Array

In order to obtain the o-NHA sample, multi-layered depositions were performed. First a 2 nm thin layer of chromium was deposited then a gold layer was added. The latter yields the good plasmonic property of the nanostructure whereas the chromium layer enhances the adhesion between the gold layer and the substrate.

Attention must be paid to the total thickness of the metallic film. This had to be large enough to become opaque for the impinging light radiation, thus avoinding the ordinary transmission through the metallic film and favouring the extraordinary optical transmission (EOT) through the holes. On the other side, too thick metalic layers could trap the nanosphere preventing us from removing them.

Once the deposition was done, the o-NHA finally was obtained by removing the PS nanoparticles. Firstly they were peeled off with the adhesive tape and then were sonicated

in toluene to dissolve and remove the residual polystyrene. Figure 3.9 shows a nanohole array obtained after mask removal. Therefore, metallic ordered NanoHole Array samples on chosen substrates were obtained by NSL combined with RIE and sputtering deposition. The figure 3.10 summarizes the nanofabrication steps to produce an o-NHA, from the self-assembly of a close-packed mask to the metallic nanohole array.

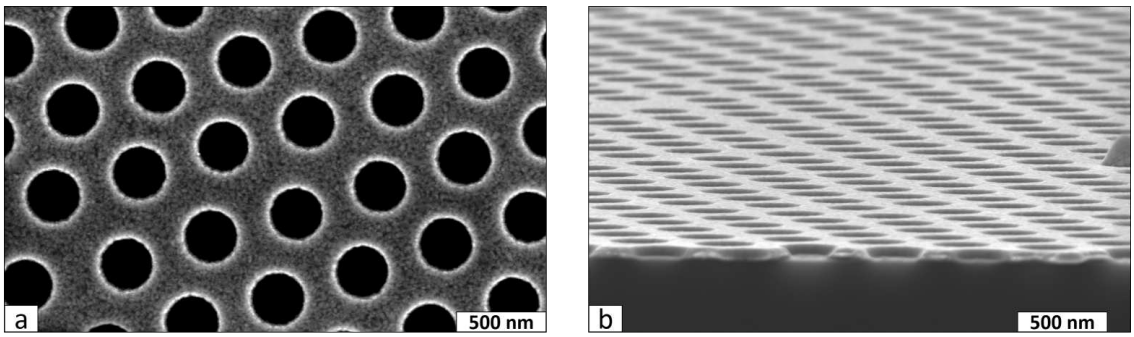

Figure 3.9: FE-SEM images, (a) top-view and (b) side-view, captured at 100kX magnification of o-NHA sample after the mask removal. The mask from 522 nm PS nanospheres was etched for 12 min and then 2 nm of Cr and 70 nm of Au were deposited.

Once again it must be stressed how simply geometrical parameters could be tuned thanks to the Nanosphere Lithography technique. The morphology of an hexagonal nanohole array is fully described by three parameters, the periodicity a, the hole diameter d and the metal film thickness t, which can be finely tuned.

- Periodicity a of the hexagonal array is equal to the initial diameter of the polystyrene nanospheres used to create the mask.
- Hole diameter d is tuned varying the etching time in the RIE step.
- Thickness t is tuned by changing the metal deposition time.

For d and t calibrations have to be done first to obtain a relation between the time and, respectively, the hole diameter and the thickness. Another geometrical parameter that is linked to a and d is the hole coverage of the surface that is defined as the ratio between the area occupied by holes and the total area. It can be demonstrated that the surface coverage of the holes, θ, is given by

$$\theta = \left(\frac{d}{a}\right)^2 \frac{\pi}{2\sqrt{3}}.$$

As pointed out in section 1.5 the plasmonic properties of the nanohole arrays are strongly dependent on their morphology and thus they can be simply tailored for specific purposes by changing the geometry.

3.2 Sparse Colloidal Lithography

This is another powerful fabrication technique which represents a valid alternative for the NSL if the order of the nanostructure pattern is not mandatory. It allows to cover large surface areas with nanostructures in a cost effective way and with high throughput

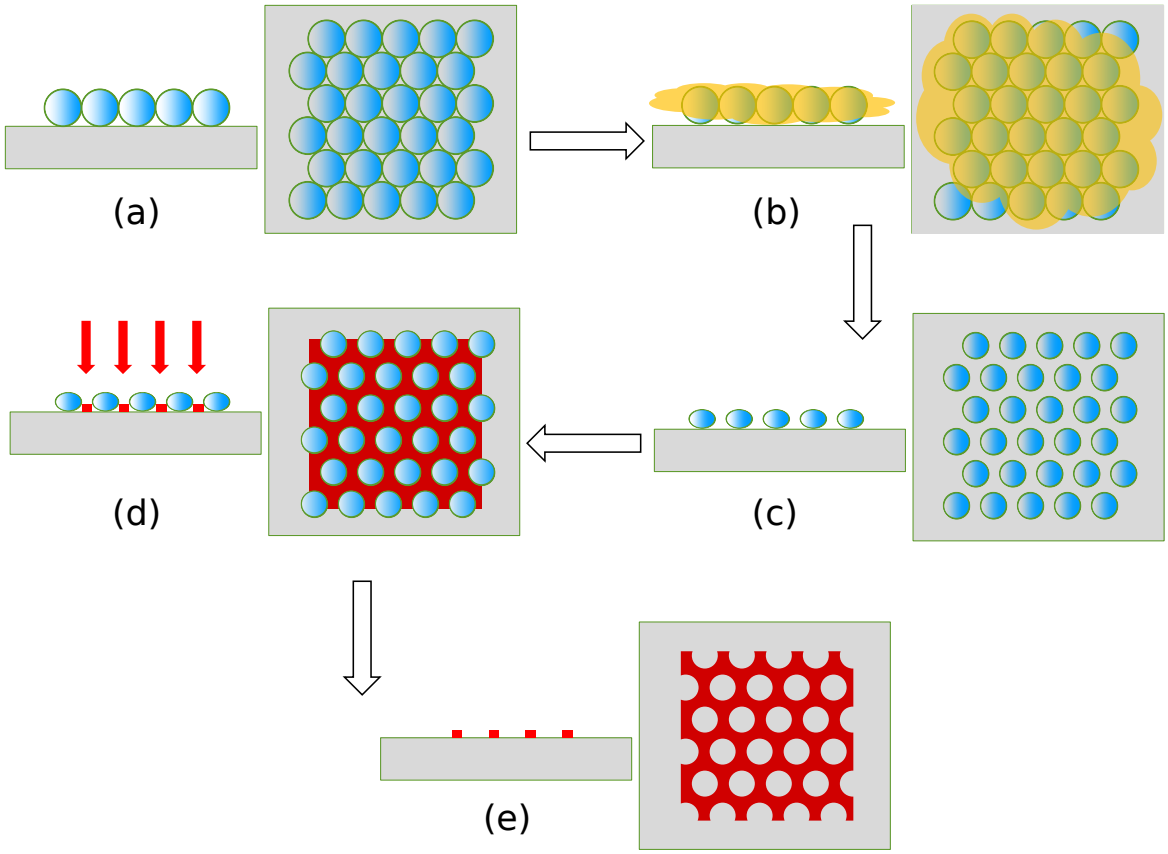

Figure 3.10: Steps for the production of o-NHA are here summarized. (a) A close-packed mask of PS nanospheres is self-assembled on a substrate. (b) A RIE process shrinks the spheres' size and (c) an hexagonal non-close-packed mask is obtained. (d) Metal is deposided on the substrate through the mask, which is then removed. (e) After the mask removal a metalic nanohole array is obtained.

by controlling the shape, the size and the spacing of the pattern. Even though there is no long-range symmetry, the patterns produced by SCL present a short-range order similar to structure of an amorphous medium. As for the NSL, the SCL consists in, firstly, depositing a monolayer of PS nanoparticles and, secondly, using this monolayer as a deposition mask to obtain a specific pattern of nanostructures. Now will follow a detailed description of the SCL technique and the fabrication of the NanoDisk Array and the disordered NanoHole Array.

3.2.1 Random adsorption of charged PS nanospheres

Differently from the NSL, whose self-assembling process of the PS nanospheres takes place at the water/air interface, in the SCL charged particles are randomly adsorbed directly onto a oppositely charged substrate, driven by electrostatic interaction. The protocol employed in this work for the particles deposition is based on the work of P. Hanarp et al. [93] which points out the fundamental parameters for the SCL process such as the ionic strength, the pH and the concentration of the particle solution that is employed.

Firstly, the substrates were pre-cleaned as described in section 3.1.1 and a solution of monodispersed negatively charged PS nanoparticles was prepared. In order to allow their

irreversible adsorption on the substrate, this had to be oppositely charged by exposure in sequence to three polyelectrolyte solutions, which added on the surface a positively charged precursor film of roughly 1 nm thickness [94]. Therefore, a freshly cleaned substrate was exposed in sequence to 2% w/w Poly(diallyldimethylammonium chloride) (PDDA), 2% w/w Poly(sodium 4-styrenesulfonate) (PSS) and 5% w/w Aluminum Chlorohydrate (ACH) by thoroughly rinsing it with Milli-Q water at each step.

The solution of negatively charged PS nanospheres was deposited on the positively charged substrate and thus the adsorption process started. Finally, the remaining PS nanoparticles were washed away with Milli-Q water and the substrate was dried with N_2 gas flow.

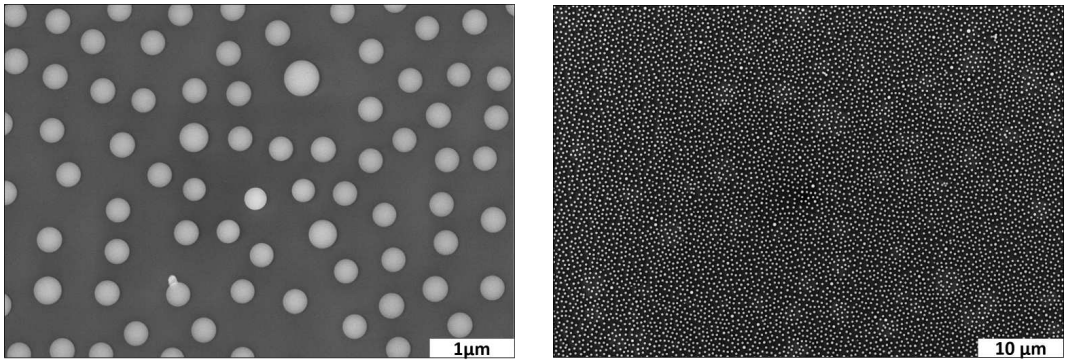

(a) Zoom 50kX **(b)** Zoom 5kX

Figure 3.11: FE-SEM image of disordered PS nanospheres with 300 nm diameter. A surface coverage $\theta = 0.21$ has been computed.

The figure 3.11 shows a typical disordered monolayer of PS nanospheres obtained by SCL. The particles are homogeneously distributed over wide areas and disuniformities arise in correspondence of the nanospheres, whose dimensions are out of the monodisperse size distribution given by the PS nanoparticle producer. The FFT computed image in 3.12a highlights that the PS monolayer is similar to an amorphous medium due to the homogeneity and the small amount of aggregates. In addition to the spheres diameter, there are two other geometrical parameters that characterize the PS mask: the surface coverage θ and average centre to centre distance r_{avg} between the neighbouring particles. The former was easily computed as a ratio $\theta = \frac{\text{Area covered by particles}}{\text{Total area}}$ while the latter was computed from the Radial Distribution Function (RDF), $g(r)$. It is defined by

$$g(r) = \frac{\rho(r)}{\rho_0} \tag{3.3}$$

where ρ_0 is the average density of nanoparticles and $\rho(r)$ is the density of spheres in a circular thin shell with r radius around a chosen particle. In the RDF graph in figure 3.12b, the first peak corresponds to the average distance between neighbouring nanospheres $r_{avg} \simeq 520\,\text{nm}$.

The diameter of the particles is fixed but monodispersed PS nanospheres are available with diameter from tenths of nm up to hundreds of microns. The surface coverage θ and average distance r_{avg} instead can be tuned within certain limits during the nanoparticle deposition step. For this purpose, as previously introduced, the most important parameters are the ionic strength and the concentration of the particle solution and the deposition time of the particles [95, 15].

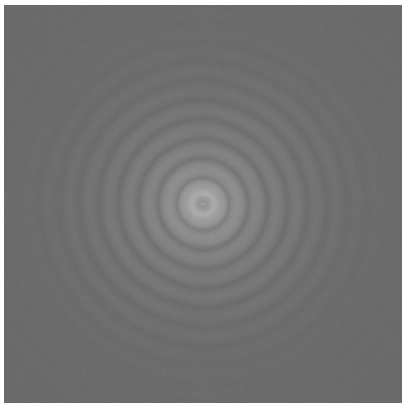

(a) FFT image for the sample in figure 3.11

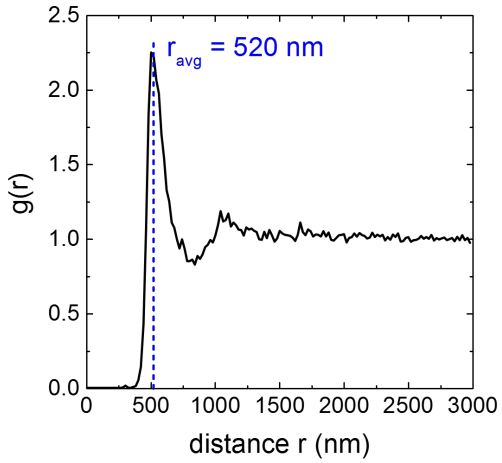

(b) Radial Distribution Function $g(r)$ for sample in figure 3.11

Figure 3.12: FE-SEM images from figure 3.11 were analyzed by ImageJ software.

The higher is the particle concentration the greater will be the surface coverage and the smaller will be the r_{avg}. Since coulombic repulsion of the charged particle sets an upper limit for the surface coverage, in order to further increase it, the ionic strength of the particle solution could be increased simply by adding NaCl. Thus, due to the screening effect of the ions the coulombian repulsion is weakened and a higher surface coverage could be achieved. However, the number of aggregates could copiously increase by pushing to the upper limit the surface coverage.

Despite the experimental challenge of avoiding the aggregation of nanoparticles, there is also a theoretical upper limit for the surface coverage. In the simplest case that consists of non-interacting particles (i.e., neutral particles) the irreversible adsorption on a substrate can be described by the Random Sequential Adsorption (RSA) model [96] who sets an upper limit for the surface coverage of $\theta = 0.547 \pm 0.002$ [97].

On the other side, there is no theoretical lower limit for the surface coverage. Decreasing the particle concentration would decrease also θ. However, a low particle concentration could affect the homogeneity and large areas could result empty. There are two ways of lowering the surface coverage without loosing homogeneity. On the one hand, the time deposition could be reduced in order not to reach the saturation concentration thus reducing the number of particles randomly adsorbed. On the other hand, the surface coverage of a polystyrene mask already produced could be decreased by exposing the PS monolayer to a RIE process, already introduced in section 3.1.3, in order to decrease the diameter of the particles and so θ. The main drawback of the RIE is that the choice of substrates is limited to the ones that resist to such process thus excluding polymeric substrates such as Poly(methyl methacrylate) (PMMA) and Polydimethylsiloxane (PDMS).

3.2.2 Disordered NanoHole Array

As previously introduced, one of the nanostructures that was obtained from Sparse Colloidal Lithography is the disordered NanoHole Array [98, 15]. Once a monolayer of disordered PS particles was formed on a substrate, a multilayered metalic film was deposited through the mask by thermal evaporation or by magnetron sputtering (cf. section

3.1.4). In order to obtain a plasmonic nanostructure first a chromium layer was deposited as adhesion layer then a gold layer was added. Since the surface coverage could be varied, samples with θ similar to the one of the o-NHA were obtained. Thus both ordered and disordered NHA were synthesized with similar surface coverage, hole diameter and film thickness allowing a direct comparison between nanostructures with similar morphology but different symmetry.

After the metal deposition, the PS nanospheres were removed by peeling them with the scotch tape followed by sonication in toluene to clean any PS residual.

The figure 3.13 shows two d-NHA samples obtained from similar PS nanoparticle mask. The sputtered d-NHA have a slightly smaller diameter than the evaporated one, respectively $d_{sput} = 271 \pm 10\,\text{nm}$ and $d_{eva} = 298 \pm 12\,\text{nm}$ for the samples in picture. The reason of this small difference is showed in figure 3.8.

It is then clear how Sparse Colloidal Lithography technique allow to tune the morphological parameters of the d-NHA, such as diameter and average interdistance, by employing different particle solutions for the mask formation and by eventually combining the SCL technique with the RIE.

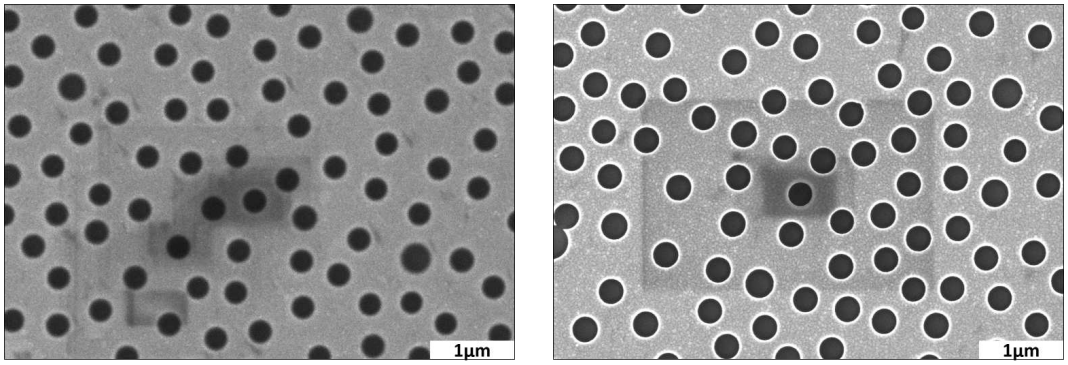

Figure 3.13: Two d-NHA samples obtained by sputtering deposition (left) and thermal evaporation (right). FE-SEM images with 50kX magnification.

3.2.3 Hole-mask Colloidal Lithography and NanoDisk Array

Since the SCL presents some limitations in producing different nanostructures on any substrate, its applicability to the nanofabrication has been extended by the developing of the Hole-mask Colloidal Lithography (HCL) technique [16]. The HCL consists in producing a thin disordered NanoHole Array by SCL on the top of a sacrificial layer previously deposited on the substrate. After selectively etching the sacrificial layer in correspondence of the nanoapertures, this hole-mask can be used as a mask for the metal deposition. Finally the sacrificial layer is removed and thus the wanted nanostructure is obtained on the substrate.

Thank to the HCL technique a large number of 3D confined nanostructures can be produced: circular and elliptical disks [16], nanorings [99], spit-rings [100]. A further development of this technique is introduced by Syrenova et al. [101]. The Shrinking-Hole Colloidal Lithography relies on fact that, during the deposition through the hole mask, metal is also deposited at the hole rims thus decreasing their diameter. By carefully exploiting this process during consecutive metal depositions, arrays of nanostructured dimers or trimers can be obtained.

In this work the HCL technique has been exploited for the synthesis of disordered NanoDisk Array. Firstly a PMMA sacrificial layer was spin-coated on the freshly cleaned

substrates and cured on a hot plate at 170°C for 10 minutes. Then the hydrophilicity of the PMMA layer was improved by a short UV/Ozone treatment. With respect to the SCL process presented in section 3.2.1, the PMMA substrate was exposed only to one polyelectrolyte solution, Poly(diallyldimethylammonium chloride). The PS nanoparticles were then adsorbed on the positively charged PMMA layer and hereafter the metal was deposited and particles were peeled off in order to obtain the nano-hole mask. The PMMA layer was then etched by Reactive Ion Etching (sec 3.1.3) in an Ar/O_2 plasma with a 7 W power. Finally, the plasmonic NDAs were obtained by thermal evaporation followed by the lift-off of the sacrificial layer in toluene. The figure 3.14 summarizes the main steps of the NDA fabrication while figure 3.15 presents two FE-SEM images of NDA thus obtained.

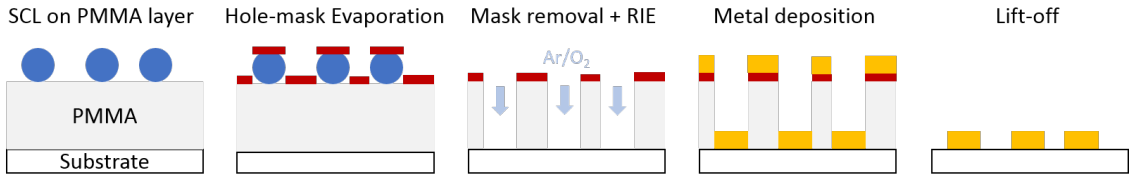

Figure 3.14: The main steps for the synthesis of NanoDisk Array are depicted: first a disordered nanosphere mask was obtained on the top of a PMMA sacrificial layer, a thin metallic layer was deposited to obtain the hole mask, the PMMA layer was etched in corrispondence of the holes, the metal was deposited through the mask and finally the lift-off was performed in toluene.

As for the other nanostructures introduced in this chapter, the geometry of the NDA can be varied thanks to the versatility of the colloidal lithography.

- The disk diameter d is determined by the dimension of the charged nanoparticles.
- The average distance d_{avg} can be tuned by varying the surface coverage as explained in section 3.2.1.
- The height h of the nanodisks is controlled by the last metal deposition and the only constraint is that it has to be much smaller than the thickness of the PMMA layer in order to allow the lift-off.

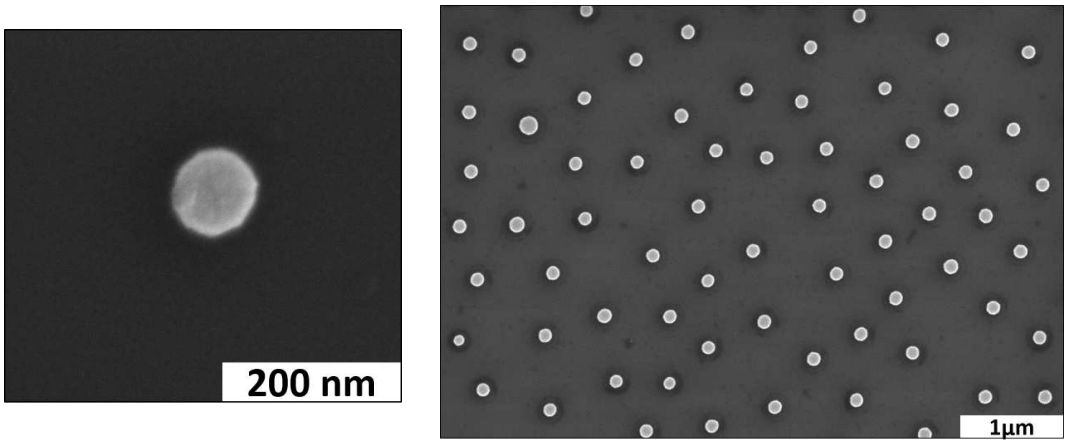

Figure 3.15: FE-SEM images of a NDA sample with 250kX

4 Numerical simulations of the optical properties

The interaction between light and materials can be computed analytically only for very simple and symmetrical geometries. For instance, the optical properties of spherical or ellipsoidal nanoparticles can be computed using Mie and Gans theory [23, 102] while multilayered films can be studied by employing the transfer matrix method [103, 104]. None of the nanostructures presented in this work can be described analytically and, in order to investigate their optical properties, Finite Elements Method (FEM) simulation techniques have been adopted.

4.1 Finite Elements Method softwares

In order to study the behaviour of the electromagnetic waves in the presence of a nanostructure, the Helmholtz equation (eq. 1.24) should be solved in the real space. For this purpose a finite space is discretized in small elements, the Helmholtz equation is solved for each small cell and the proper boundary conditions are imposed. There are two ways of investigating the electromagnetic response of nanostructures by FEM [105]. On one side, the Finite Difference Time Domain (FDTD) method solves for succeeding time steps the Maxwell's curl equations once an electromagnetic field is given as input. On the other side, the Finite Difference Frequency Domain (FDFD) methods solve the Helmholtz equation for each frequency or wavelength separately. For the purpose of this work, Frequecy Domain methods were considered due to the higher computation speed in investigating the plasmonic resonance for different wavelengths separately.

Two different computation softwares were employed to study the electromagnetic response of the nanostructures: COMSOL Multiphysics® and EMUstack.

- **COMSOL Multiphysics®** is a commercial software platform for 3D finite element simulations. Since the space domain is discretised in the three dimensions there is no symmetry costraint for nanostructures to be studied. Thus, COMSOL® could be exploited for investigating all the nanostructures introduced in the previous chapter.

- **EMUstack** [106, 107] is an open-source simulation package based on Python. With respect to COMSOL®, EMUstack presents some costraints for the nanostructures. The nanostructured materials have to be composed by stacks of layers that can be periodic in the in-plane x,y directions but have to be uniform in the z direction. Thus, the in-plane geometry of each layer is discretised and the electromagnetic field computations are made by 2D FEM while the z-axis propagation is computed analytically.

These simulation softwares allowed to investigate both near-field and far-field responses of the nanostructures to a monochromatic plane electromagnetic (EM) wave with normal incidence. By computing in parallel the response to a set of different EM wavelengths the far-field optical properties such as transmittance or absorbance spectra were obtained. Moreover, also the EM near-field distribution was obtained and its behaviour around the

nanostructure was investigated. Therefore, the hot-spots of the electric field and its decay lengths were evaluated for the simulated nanostrucutres.

Since the FEM computations for different wavelengths are independent, both the FDFD methods, COMSOL Multiphysics® and EMUstack, present a native parallelization by computing independently different wavelengths on different CPU cores. Therefore, all the FEM simulations were performed on a dedicated server: AMD Opteron 6274 server, 4 CPU, 32 cores, 128 GB RAM.

The geometrical parameters of the nanostructures were varied in order to study the correlation between the plasmonic properties and the morphology. Specifically, the spectral position of the plasmonic resonances and the corresponding local and bulk sensitivities were investigated as fuctions of the geometry. This represents a powerfull resource since it allowed to predict and optimize the sensing properties by tuning the morphology of the nanostructures. Therefore the samples for the biosensing experiments were developed by taking into account the FEM optimization in order to obtain the plasmonic resonances in the desired wavelength range and to achieve the best sensing performances.

4.2 Ordered NanoHole Array

4.2.1 Definition of the unit cell

The FEM simulations of the ordered NanoHole Array (o-NHA) were carried out with EMUstack software due to its uniform geometry along z-axis. The figure 4.1 shows the scheme that has been defined in the EMUstack source code, a top-view and a side-view, and points out the fundamental geometrical parameters: a the lattice constant, d the nanohole diameter, h the gold layer thickness and h_{Cr} the chromium layer thickness. The latter has been fixed to 2 nm since a thin chromium layer is needed only to assure the adhesion of the structures to the substrate and it hasn't good plasmonic properties. Therefore, a 2 nm Cr layer has been used for all the simulated nanostructure in this chapter, between the substrate and the gold layer.

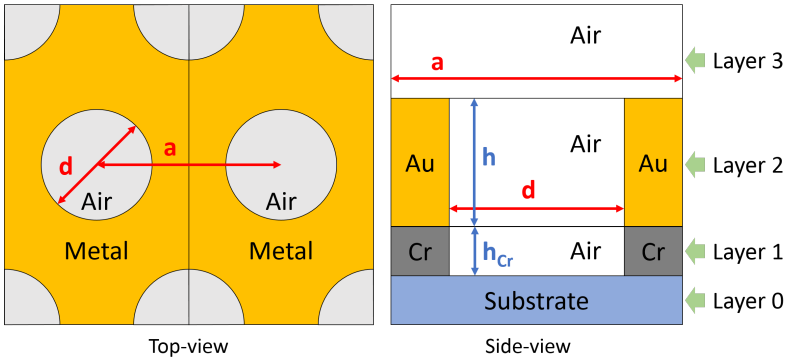

Figure 4.1: Scheme of the rectangular unit cell employed in EMUstack for FEM simulations of the o-NHA. The fundamental parameters are here highlighted: a lattice period, d diameter of the hole, h height of the gold layer and h_{Cr} height of the chromium layer which was fixed to 2 nm.

The top-view presents the in-plane geometry that consists of a rectangular $a\ \sqrt{3} \cdot a$ cell with 5 circular inclusions with diameter d, one in the center and 4 at the vertices. A rectangular lattice built with this cell reproduces the hexagonal pattern of nanoholes. The meshes of the unit cell were generated by *Gmsh 3.0* software and used by EMUstack code for the FEM computations.

The side-view in figure 4.1 shows the stack-structure of the o-NHA. On one side, the layer 0 and 3 represent uniform media respectively under and above the nanostrcuture and no FEM calculations were necessary for EM wave propagation through them. On the other side, the layer 1 and 2 represent respectively the chromium and the gold layer which are uniform in z-axis and present in-plane geometry described above. Therefore the proper FEM computation occured within this two layers.

4.2.2 Far field optical properties

In order to investigate the far-field properties, transmittance spectra were computed by changing the three geometrical parameters: a, d and h (cfr. figure 4.1). The figure 4.2 reports the transmittance spectra obtained for an o-NHA with $a = 500\,\text{nm}$, $h = 70\,\text{nm}$ and, respectively, $d = 250,\ 300,\ 350\,\text{nm}$.

In order to point out that the transmittance peak from the simulations represents the extraordinary optical transmission phenomenon, the spectra from figure 4.2a were normalized to the corresponding surface coverage. Therefore, all the normalized curves presented a transmittance maximum much larger than 100% thus confirming that the plasmonic resonance was well reproduced by the simulation.

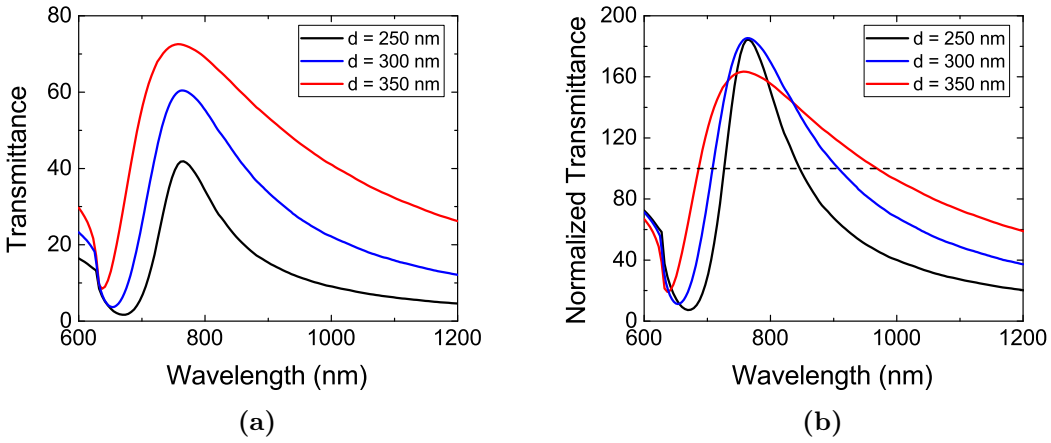

Figure 4.2: (a) Transmittance spectra obtained for 500 nm periodicity, 70 nm Au and respectively 250, 300 and 350 nm diameter. (b) The same spectra, normalized to the hole coverage factor θ

The spectral position of the extraordinary optical transmission (EOT) peak (λ_{EOT}) was computed as a function of the morphological parameters and the results are summarized in the colour plots from figures 4.3a and 4.4a.

Firstly, in the figure 4.3a the lattice constant a was varied from 250 to 1250 nm and the height h from 40 to 100 nm whereas the diameter was defined by $d = \frac{3}{5} \cdot a$, thus maintaining the surface coverage of the holes constant. It can be observed that the λ_{EOT} depends directly on the period of the o-NHA. A profile curve is presented in figure 4.3b in order to highlight that $\lambda \propto a$ and a linear fit with $y = m \cdot x + q$ was done resulting in $q = 260 \pm 40\,\text{nm}$ and $m = 1.09 \pm 0.04$. This confirms that the λ_{EOT} is directly proportional to the lattice constant a, as theoretically predicted in equation 1.43.

For the purposes of this work, the nanostructures must be resonant in a spectral region where the light sources and the detection set-ups allow a fast and high-throughput optical measurements. The optical set-ups that meet these requests cover the NIR spectral range, up to 1000 nm, so the nanostructure geometry was tuned in order to obtain the EOT peak

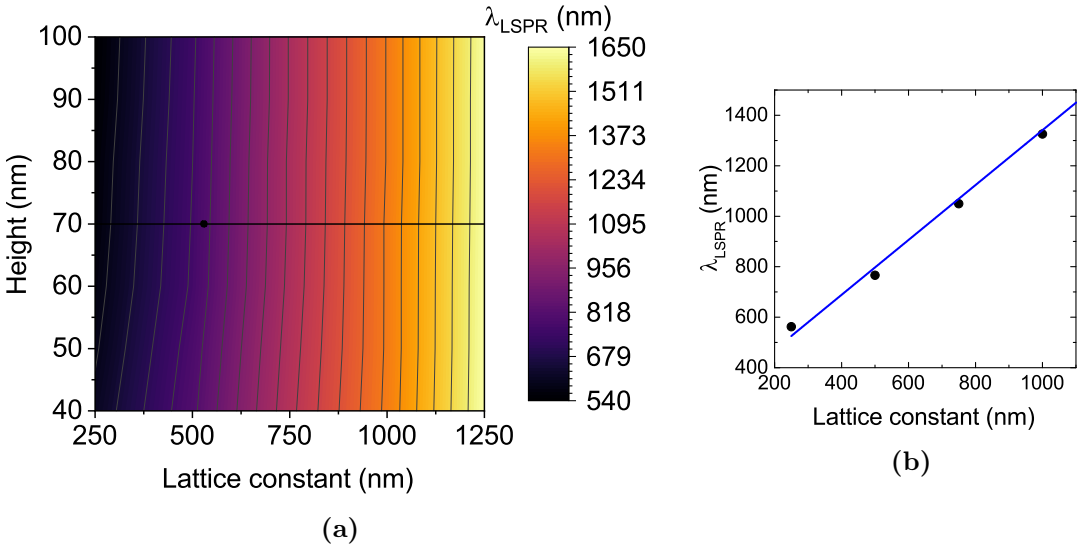

Figure 4.3: (a) Colour plot of the λ_{EOT} as a function of the lattice constant a and the height h with the diameter $d = 3/5 \cdot a$. (b) A profile line extracted to point out the linearity between λ_{EOT} and a

in a 700 - 800 nm range. From the figure 4.3a it follows that a 500 nm lattice constant would produce $\lambda_{EOT} \sim 800\,\text{nm}$ thus meeting the request above.

Secondly, the lattice constant was set to $a = 500\,\text{nm}$ and both the diameter and the height were varied respectively from 150 nm to 400 nm and from 40 nm to 100 nm. Thus, the EOT peak position is represented as a function of d and h in figure 4.4a. It can be observed that changing the diameter also allows to tune the λ_{EOT} but the latter is less affected by the diameter rather than the lattice constant variations. The profile plot in figure 4.4b shows that there is no linear dependence between λ_{EOT} and d and a parabolic plot is presented only to guide the eye.

4.2.3 Near field properties

In order to better understand the extraordinary optical transmission phenomenon, the near-field response was investigated by analyzing the electric field near the nanostructure. In this section, the near field computation were done by considering an o-NHA defined by $a = 500\,\text{nm}$, $d = 300\,\text{nm}$ and $h = 70\,\text{nm}$. In the numerical computations, the input EM radiation was a TE planewave with normal incidence and the in-plane vector for the electric field was $\vec{E} = \begin{pmatrix} 0, & E_0, & 0 \end{pmatrix}$ with $E_0 = 1\,\text{V/m}$. Therefore, the electric field enhancement occurs if the absolute value of the field exceeds E_0. In addition to E_y electric field, when the EM radiation impinges on the o-NHA a component of the electric field perpendicular to the surface ($E_\perp = E_z$) is generated at both, top and bottom, interfaces due to the plasmon resonance.

The figure 4.5a presents a map of E_z at the top interface (air/metal) when an EM wave with $\lambda_{EOT} \simeq 790\,\text{nm}$ illuminates the o-NHA thus producing the maximum transmittance. It can be observed that a strong localization of the electric field occurs at the hole edges ($E_z > E_0$) and this plasmonic coupling is responsible for the enhanced transmission. A similar map was computed by considering another incident wavelength, specifically the one that gave the minimum transmittance, $\lambda_{min} = 682\,\text{nm}$. The E_z map with λ_{min} is presented in figure 4.5b and it points out that the plasmonic coupling for this wavelength

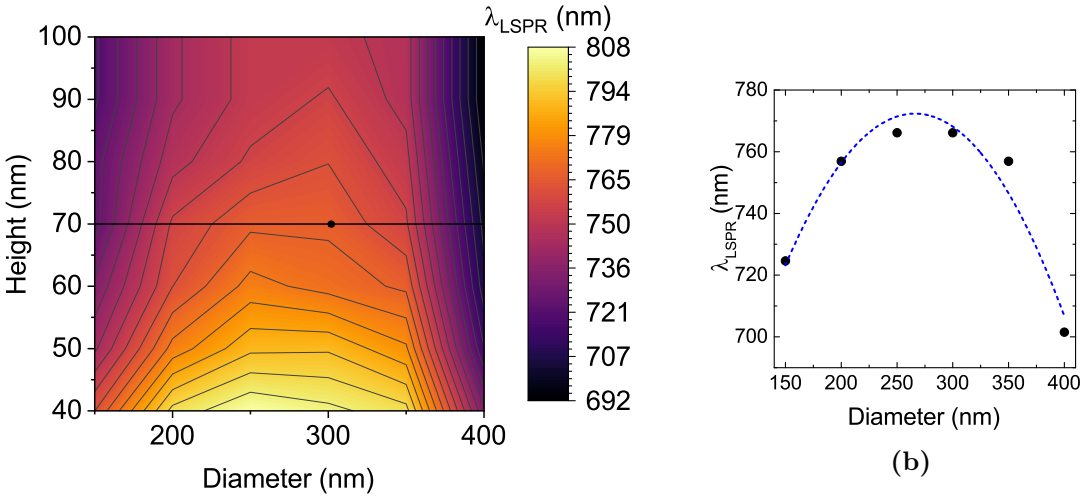

Figure 4.4: (a) Colour plot of the λ_{EOT} as a function of the diameter and the height with the lattice constant $a = 500\,\text{nm}$. (b) A profile line extracted with $h = 70\,\text{nm}$.

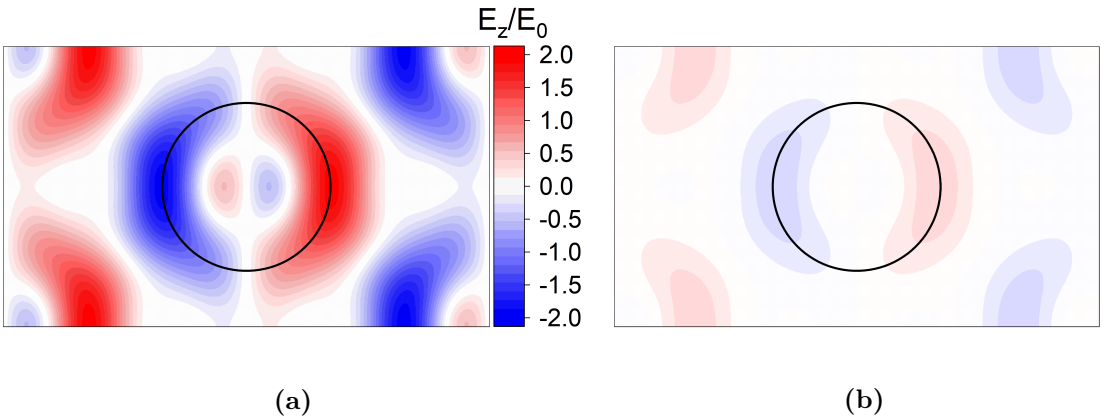

Figure 4.5: Colour map of the localized field E_z at the top interface of the o-NHA when monochromatic light impinges the surface with (a) λ_{EOT} and (b) λ_{min}.

is much weaker and thus no enhanced transmission occurs.

In order to compute how the electric field decays while moving away from the nanostructure, the local field E_z was computed as a function of the distance z from the nanostructure and depicted in figure 4.6a. The decay curves at the top and bottom interfaces are plot and two decay lenghts (l_d^{air}, $l_d^{SiO_2}$) were computed by fitting data with exponential curves:

$$l_d^{air} = 77 \pm 1\,\text{nm} \qquad l_d^{SiO_2} = 122 \pm 1\,\text{nm}.$$

The decay lengths l_d^{air} and $l_d^{SiO_2}$ represent the distance from the o-NHA at which the electric field is reduced to $\frac{1}{e}$ fraction of the electric field at 0 distance. At the bottom and top interface the enhancement factors $|E_z|/E_0$ of the electric field were found to be respectively 3.2 and 2.0 and this suggests that a more intense field localization occur at the bottom rim of the nanohole.

The behaviour of the impingin E_y field inside the hole can be observed in figure 4.6b. A section on the y-z plane of the E_y field was depicted when maximum or minimum

transmittance occur, that was obtained with respectively λ_{EOT} and λ_{min}. In order to highlight the difference between the two situations, the flux of the Poynting vector is illustrated by the yellow lines. These represen tthe energy flux density of the plane-wave electric field that impinges the hole and it is clear that when extraordinary transmission occur the field lines don't extinguish within the hole but they curve and pass through it. On the other side of the nanohole, after a short distance ($\sim 300\,\text{nm}$), the plane wave of the electric field is quickly reconstructed and it propagates in far-field. On contrary, in case of the minimum transmittance, most of the flux lines of the Poynting vector pass through the hole but extinguish quickly at the output interface. Therefore a very low intensity field is transmitted in far-field.

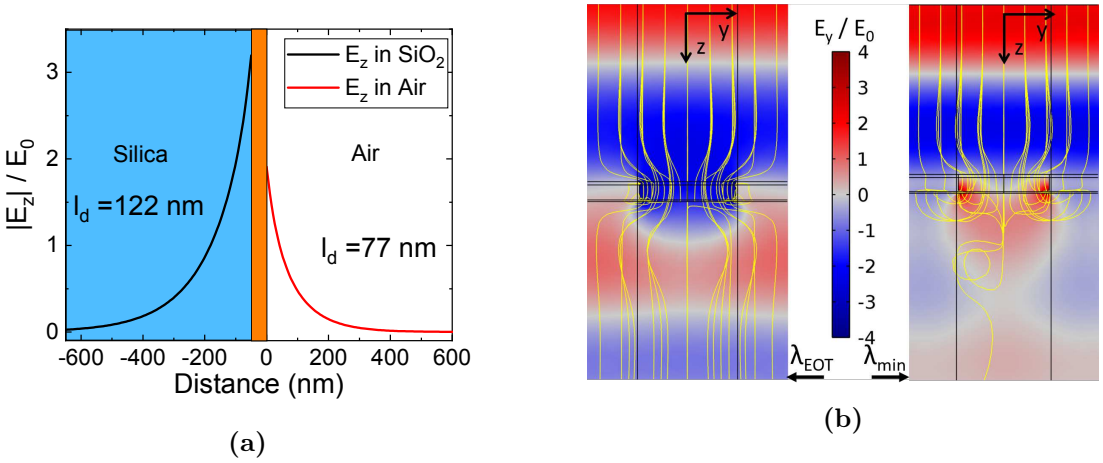

(a) (b)

Figure 4.6: (a) The decay of intensity of the localized electric field E_z as moving away from the nanostructure in z direction. Exponential curves fitted the data and the decay lengths l_d were obtained for top and bottom interfaces. **(b)** Behaviour of the impinging field E_y inside the nanohole respectively when maximum (λ_{EOT}) and minimum (λ_{min}) transmittance occur.

4.2.4 Simulated sensing properties of o-NHA

For the purpose of this work it was necessary to optimize the geometrical parameters of the nanostructures in order to achieve the best sensitivity performances. Therefore, the bulk and local sensitivities were computed changing a, d and h.

Bulk sensitivity

The bulk sensitivity tells how much the peak would shift if the refractive index of the environment above the nanostructure changes, and it is defined by $S_\infty = \frac{\partial \lambda_{EOT}}{\partial n}$. For this purpose the model depicted in figure 4.1 was employed by considering different refractive indexes for the environment. Specifically, the transmittance spectra of different o-NHA were computed in air, water and silica with respectively $n_{air} = 1$, $n_{H_2O} = 1.33$ and $n_{SiO_2} = 1.45$. The λ_{EOT} was linearly fitted as a function of n_{env} and thus, the slope represented the bulk sensitivity.

The geometrical parameters were varied as previously done for the λ_{EOT} and the bulk sensitivity was computed for each set of parameters thus obtaining the colour plots in figure 4.7. It can be observed that the S_∞ could be enhanced on one side by increasing the lattice constant and thus moving the λ_{EOT} to the infrared and, on the other side, by increasing the hole's diameter and thus the surface coverage of the holes.

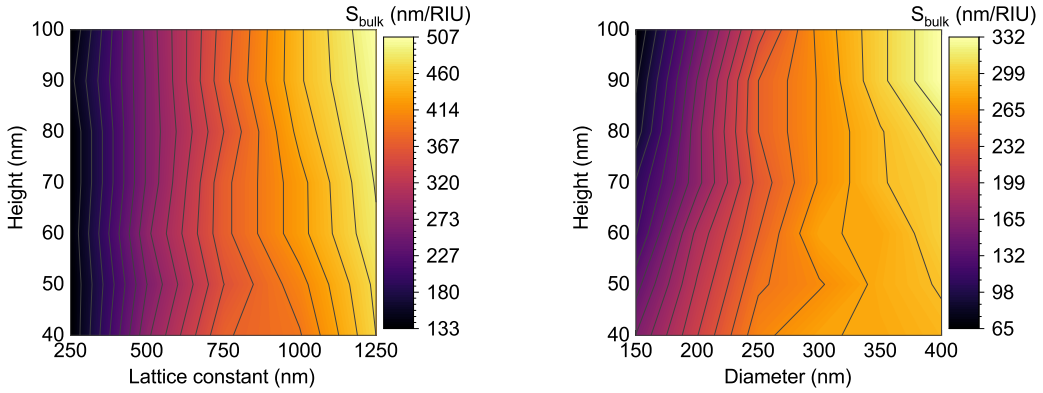

Figure 4.7: Colour maps of the bulk sensitivity as a function of the o-NHA morphology. In (a) the lattice constant a and the height h were varied and diameter was set to $d = 3/5 \cdot a$. In (b) the lattice period is fixed to 500 nm.

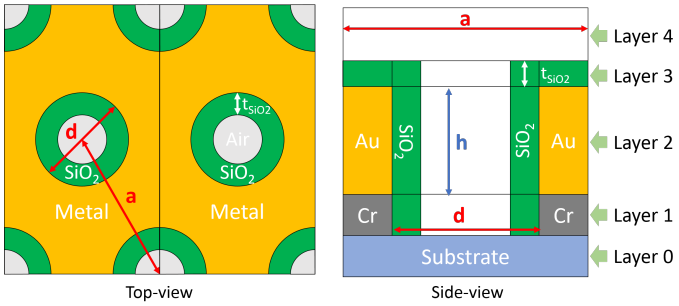

Figure 4.8: Due to the EMUstack costraints of the geometry, a more complex stack structure was designed in order to simulate the local sensitivity of the o-NHA thus slightly increasing the computation costs.

Local sensitivity

The local sensitivity tells how much the plasmonic peak would shift if a thin layer of dielectric is added to the surface of the nanostructure. For its computation, the new scheme in figure 4.8 was designed for the o-NHA in order to add conformally a dielectric layer on the nanostructure. Once the geometry of the o-NHA was set, the transmittance spectrum was simulated for increasing thicknesses of the SiO_2 layer, $t_{SiO_2} = 1, 2, 4, 6, 8, 12, 24, 36$ nm. The response of the EOT for thin layer of dielectric is given by equation 2.4 and it can be semplified by linearization for small t_{SiO_2}:

$$\lambda_{EOT}(t_{SiO_2} = t) = \lambda_{EOT}(t_{SiO_2} = 0) + S_0 \cdot (n_{SiO_2} - n_{air}) \cdot t \tag{4.1}$$

Therefore, a linear fit with $y = m \cdot x + q$ was performed and the local sensitivity was computed as follows:

$$S_0 = \frac{m}{\Delta n} = \frac{m}{n_{SiO_2} - n_{air}}. \tag{4.2}$$

As for the bulk sensitivity, the local one was computed by changing the geometrical parameters in order to find the morphology that produced the best performance. The results are plotted in figure 4.9. In figure 4.9a, the surface coverage of the o-NHA was

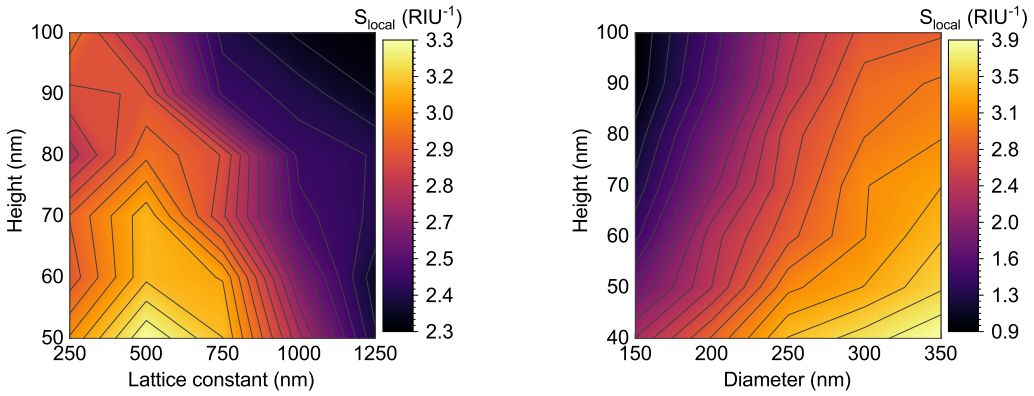

Figure 4.9: Colour maps of the local sensitivity as a function of the o-NHA morphology. As for the bulk sensitivity in figure 4.7, in (a) the lattice constat was varied while in (b) the diameter was changed.

fixed at $d = \frac{3}{5} \cdot a$ and it resulted that increasing the lattice constant did not enhance S_0 as for the S_∞. On the contrary, the best S_0 was achieved for a 500 nm periodicity. Then the lattice constant was fixed to $a = 500\,\text{nm}$ and both the height h and diameter were varied. The results are depicted in figure 4.9b and they show that the local sensitivity depends heavily on the diameter of the nanohole and it's enhanced as the diameter increases.

Since the S_0 property is the fundamental one for the biosensing applications, where thin layers of biomolecules bound to the surface of the nanostrcutures have to be detected, it is clear that the lattice constant $a \simeq 500\,\text{nm}$ yields the best sensing performances.

With regard to the diameter choice, the sharpness of the EOT peak must be taken into account although the figure 4.9b suggested that the larger the diameter and the smaller the height, the better local sensitivity is. However, both a larger diameter and a shorter height produced an EOT peak with larger FWHM thus making harder to resolve experimentally very small shifts of the resonance peaks. Therefore, a sharper resonance was also needed in addition to a high S_0 and this leaded to a compromise regarding the geometrical parameters h and d. Indeed, a figure of merit $F = \frac{S_0}{FWHM}$ can be introduced to follow the experimental determination of $\Delta\lambda$.

For the purpose of this work, the nanofabrication aimed to synthesize o-NHA with periodicity $a = 500\,\text{nm}$, hole-diameter $d = 300\,\text{nm}$ and thickness of the gold layer $h = 70\,\text{nm}$. For these parameters, the following sensing performances are expected:

$$S_\infty = 280 \pm 10 \frac{\text{nm}}{\text{RIU}} \qquad S_0 = 3.1 \pm 0.1 \frac{1}{\text{RIU}}.$$

4.3 NanoPrisms Array

4.3.1 Definition of the unit cell

The FEM computations for the NanoPrisms Array were carried out with COMSOL Multiphysics® and figure 4.10 presents the model that was employed. It can be observed that there are two nanoprisms per unit cell and the simulation geometry is defined by the lattice constant a, the lateral dimension of the nanoprism L and the height h The side of the nanoprism was set to $L = f \cdot a$, with $f = 0.3$ that was also suggested by the

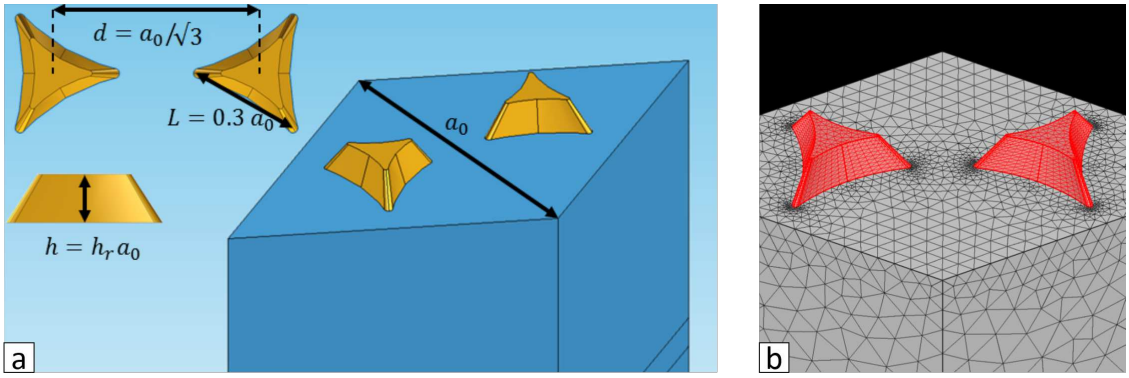

Figure 4.10: The model employed for the NPA simulations. (a) The unit cell and the main geometrical parameters are presented. (b) The meshed model of a unit cell.

experimental measurements of a and L that are depicted in figure 5.4. The height was defined by $h = h_r \cdot a$, so the free parameters for the model were the lattice constant a and the relative height $h_r = h/a$.

With respect to the EMUstack software, the COMSOL Multiphysics® simulations for the NPA rely on 3D FEM computations carried out on a 3D mesh that is presented in figure 4.10b.

In the model designed and employed for the NPA computation, no Cr adhesion layer was added. The optical and sensing properties that are presented in the following sections for the NanoPrisms Array have been also reported in Michieli et al. (2015) [108].

4.3.2 Far field optical properties

The absorbance spectra of the NPA were computed by changing a and h_r geometrical parameters. With respect to the o-NHA that presented an extended surface plasmon resonance, the NPA, due to their 3D confinement, presented a Localized Surface Plasmon Resonance (LSPR) that manifests as a peak in the absorbance spectrum.

The figure 4.11a presents the absorbance spectrum obtained from a simulation of a NPA with $a = 500\,\text{nm}$ and $h_r = 0.1$. The main peak centered in λ^I_{LSPR} represents the dipolar LSPR whereas the smaller peak represents the quadrupolar LSPR, centered in λ^{II}_{LSPR}. The dipolar resonance that arises when light with the proper λ impinges the nanostructure was considered the main plasmonic peak and it was monitored as a function of the geometrical parameters.

Simulations were carried out in order to investigate how the dipolar peak position λ_{LSPR} changes as the geometrical parameters were varied. As previously pointed out, for the aim of this work a plasmonic resonance in the NIR range is preferable and thus the simulations focused on studying the dependance of the resonance wavelength in the 600 - 1000 nm range. More specifically the lattice constant has been varied from $a = 300\,\text{nm}$ to $a = 800\,\text{nm}$ whereas the relative height has been varied from $h_r = 0.05$ to $h_r = 0.20$.

A color map of the results is presented in figure 4.11b and it can be clearly observed that the position of the dipolar LSPR can be tuned finely by choosing properly the geometrical parameters.

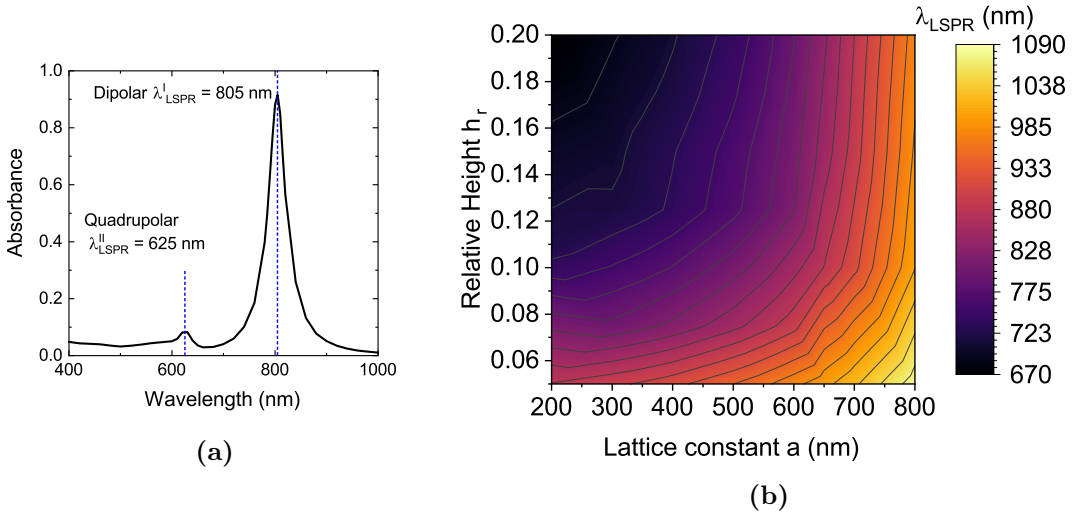

Figure 4.11: (a) Absorbance spectrum obtained from simulation with $a = 500\,\text{nm}$ and $h_r = 0.1$. (b) λ_{LSPR} as a function of a and h_r.

4.3.3 Sensing properties of NPA

The sensitivity performances were investigated by varying the geometrical parameters. These had to be optimized not only to ensure a LSPR resonance in the NIR range but also to achieve the best sensitivity performances. Therefore the bulk and local sensitivities for the NPA were computed as a function of the free parameters a and h_r. The scheme employed for the simulations is depicted in figure 4.12

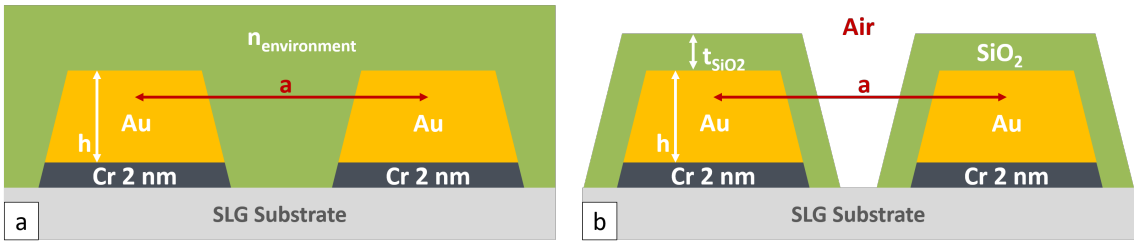

Figure 4.12: Scheme for the sensing simulation. (a) The refractive index of the environment above the nanostructure was changed, thus bulk sensitivity was computed. (b) Incremental thin layers of SiO_2 with thickness t_{SiO_2} were added conformally on the top of the NPA in order to compute the local sensitivity.

Bulk sensitivity

The plasmonic resonance was computed for the NPA fully embedded in an homogeneous medium with different refractive indexes n_{env}. The λ_{LSPR} was computed in air ($n = 1$) and in glycerol ($n = 1.47$) and thus the bulk sensitivity was obtained from the following expression: $S_\infty = \frac{\Delta\lambda_{LSPR}}{\Delta n}$. The figure 4.13a presents S_∞ as a function of the height of the gold nanoprism and the lattice constant and it points out that S_∞ increases as both a and h_r increase. Therefore, the larger is the nanoprism, the greater is the S_∞ and this means that the bulk sensitivity depends mainly on the area of the interface between metal and air, where plasmonic coupling can occur.

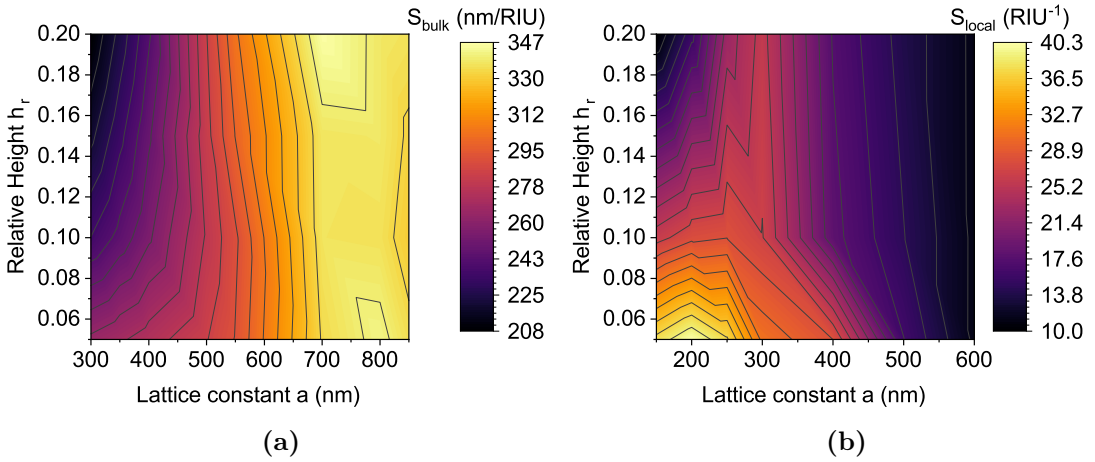

Figure 4.13: (a) S_∞ is reported as a function of the lattice constant a and the relative height h_r. Maximum S_∞ was achieved for $a \sim 800\,\text{nm}$. (b) S_0 is reported as a function of a and h_r and a maximum S_0 was found for $a \sim 200\,\text{nm}$ and $h_r \sim 0.05$.

Local Sensitivity

In order to study the local sensitivity, the λ_{LSPR} was computed for NPA conformally covered by a dielectric thin layer with increasing thickness, as reported in figure 4.12. Once the lattice constant and the height were fixed, λ_{LSPR} was computed for different thicknesses t_{SiO_2} and the local sensitivity was then obtained from a linear fit of the data $\lambda_{LSPR}(t_{SiO_2})$.

The local sensitivity was then investigated by changing the geometrical parameters of the NPA and S_0 as a function of a and h_r is presented in the color plot in figure 4.13b. A maximum local sensitivity was found for $a \sim 200\,\text{nm}$ and $h_r \sim 0.05$. The smaller the lattice constant, the smaller the cross section of the nanoprism is and thus the better the field confinement is. Therefore, the localization of higher electric fields within shorter distances allow to better reveal the presence of dielectric layers with thicknesses of a couple of nanometers, that are much shorter than the decay length of the field.

For the purpose of this work, as previously specified, an easily-revealable resonance peak in the 700-800 nm range is preferable. For this reason, non-optimized geometrical parameters were chosen: $a \sim 500$ nm, $h_r \sim 0.14$ as standard for the synthesis described in the next chapter. With these geometrical parameters the local sensitivity is expected to be $S_0 \sim 15\ \text{RIU}^{-1}$.

As previouly said, no chromium layer was considered for these computations. In order to check how the local sensitivity would be affected by the presence of a 2 nm chromium layer a comparison has been made by considering $a \sim 500$ nm, $h_r \sim 0.14$. It resulted that S_0 diminish by $\sim 10\%$. Therefore the expected local sensitivity for such geometry was $S_0 = 13.6 \pm 0.5\,\text{RIU}^{-1}$.

4.3.4 Near field properties

The behaviour of the localized electric field was also investigated for a NPA with lattice constant $a = 500\,\text{nm}$ and $h_r = 0.10$. When light with the proper λ_{LSPR} impinges the nanostructure, electric field is localized and enhanced near its surface. Therefore, a E_z component of the electric field arises when LSPR occurs and a detailed description of E_z is depicted in figure 4.14. The electric field hotspots were found to be at the tips of the

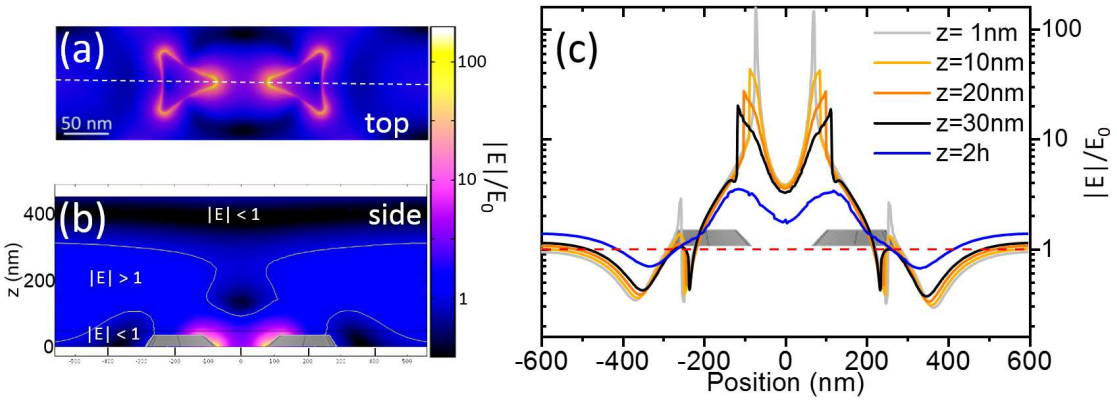

Figure 4.14: Localized electric field around the NPA is described. (a)Top-view of two nanoprism where the hot-spots at the tips can be observed. (b) Side-view across the dashed line in (a). It can be observed that the localized field at the tips decays fastly. Yellow line represents the curve where $E_z = E_0$ (c) E_z at different distances z above the nanoprism is plotted as a function of the position x across the dashed line in (a).

nanoprism. Here, the E_z on the surface of the nanoprism reached intensities tenth times greater than the input electric field ($E_0 = 1\,\mathrm{V/m}$). The decay of E_z moving away from the nanoprism was also investigated and it can be observed in figure 4.14b,c. The electric field decays exponentially as a function of z in the environment above the nanoprism, thus the decay length in corrispondence of the hot-spots was computed to be:

$$l_d^{NPA} = 10.5 \pm 0.5\,\mathrm{nm}$$

The decay lenght si about one tenth with respect to the one of the o-NHA. This points out that in the nanoprism, where LSPR occurs, the electric field is much more enhanced and also confined in much smaller volumes with respect to the NanoHole Array (NHA), where extended surface plasmon resonance occurs.

4.4 NanoDisk Array

4.4.1 Unit cell

The FEM computations for the NanoDisk Array, as for the NPA, were carried out with COMSOL Multiphysics®. Although this nanostructure presents the uniformity along z-axis that EMUstack software requires, the lack of an ordered lattice, that is fundamental for EMUstack, prevents from employing it for the NanoDisk Array (NDA) simulations. Therefore, the FEM computations for the disordered NDA were possible by simulating the behaviour of one single disk without imposing the periodic boundary conditions.

The unit cell employed in COMSOL computations, is presented in figure 4.15. The two main parameters are the diameter d of the nanodisk and the height h of the gold layer. A 2 nm chromium layer was added as an adhesion layer between the silica substrate and the gold. FEM computations have been performend by changing the two free parameters and thus the plasmonic properties have been investigated as a function of h and r.

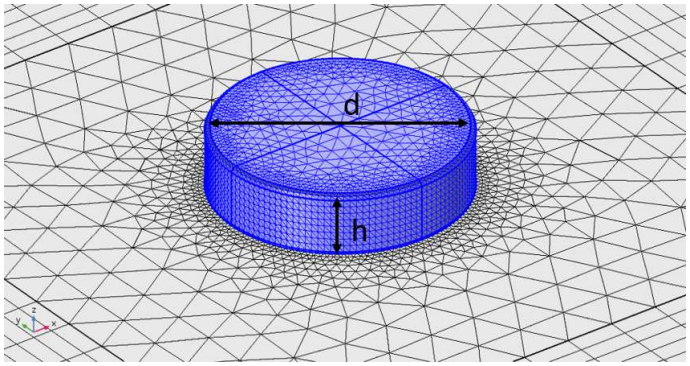

Figure 4.15: Unit cell for nanodisk simulation.

4.4.2 Far field optical properties

From the computations, the optical properties of a single nanodisk were calculated. In order to obtain the response of a disordered nanodisk array, the single response can be simply multiplied by the number of illuminated nanodisks since non interacting nanostructures are considered. This assumption will be further justified in section 4.4.4 by investigating the near field properties.

The extinction spectra of the nanodisk were computed by changing the diameter and the height. The figure 4.16a presents the exctinction spectra obtained from a nanodisk with $h = 90\,\text{nm}$ and different diameters, $d = 150, 200, 250, 300\,\text{nm}$. The wavelength at which exctinction reaches its maximum corresponds to the wavelength at which LSPR is excited. It is clear then, that the spectral position of the peak and thus the λ_{LSPR} depend heavily on the diameter and redshift as the diameter increases.

The figure 4.16b presents a color map that relates the λ_{LSPR} to the h and d parameters. This points out that the spectral position of the LSPR peak depended heavily on the diameter of the nanodisk while increasing the heigth of the gold layer yields only a small variations of the λ_{LSPR}.

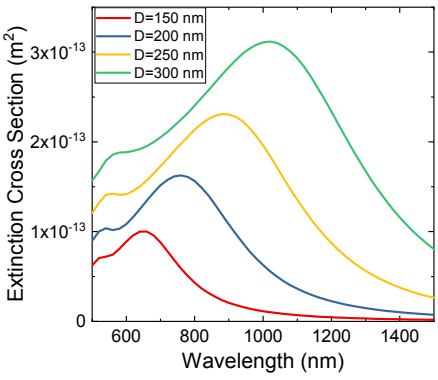

(a) Extinction spectra

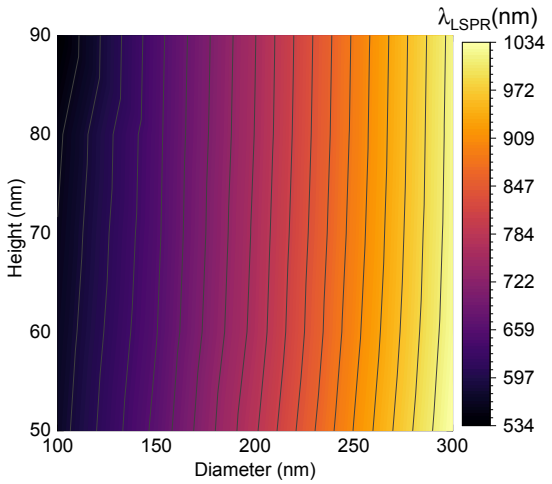

(b) λ_{LSPR} as function of h and d

Figure 4.16: **(a)** Extinction spectra of nanodisks with $h = 90\,\text{nm}$ and different diameters: $d = 150, 200, 250, 300\,\text{nm}$. **(b)** Color map that presents the λ_{LSPR} as a function of the geometrical parameters h and d.

4.4.3 Sensing properties

The expected sensing performances were investigated for the nanodisk by changing the geometrical parameters h and d. Therefore, the bulk and the local sensitivities were computed as functions of h and d.

Bulk sensitivity

The extinction spectra of a nanodisk on a silica substrate for were computed by taking into account two environments, air ($n = 1$) and glycerol ($n = 1.47$). The variation of the LSPR peak position ($\Delta\lambda_{LSPR}$) was computed and then the bulk sensitivity was obtained from: $S_\infty = \frac{\Delta\lambda_{LSPR}}{\Delta n}$. Therefore, the colour map for S_∞ in figure was obtained by computing the exctinction spectra in two different environment and by changing h and d.

It can be observed that S_∞ increases remarkably as the diameter grows whereas the height gives a small contribute. Since the plasmonic coupling occurs mainly at the top and bottom rims of the nanodisk (cf. section 4.4.4) a larger diameter would increase the area where electric field is enhanced, thus leading to a higher bulk sensitivity. For higher nanodisks, the half-way area between the top and bottom edge increases and since low field enhancement occurs in-between, a modest dependance of the S_{bulk} on h is expected.

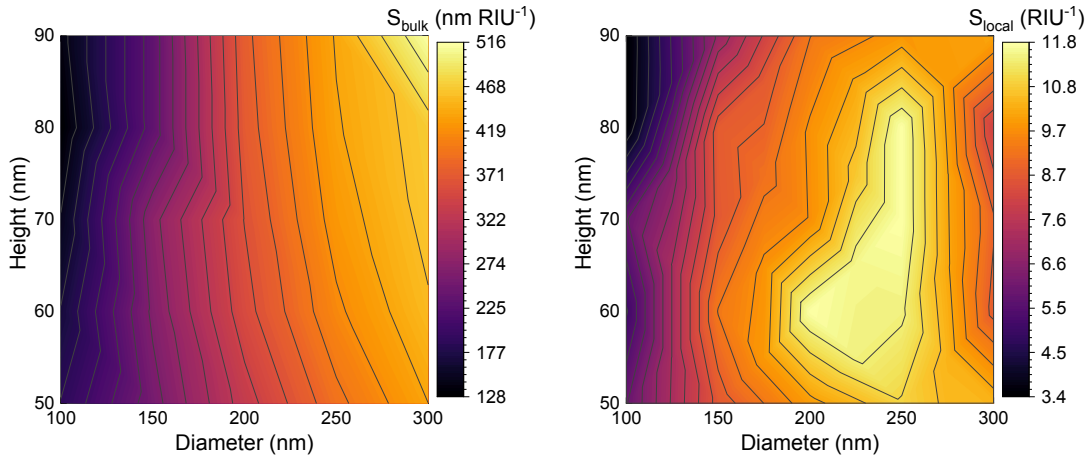

(a) $S_\infty(d, h)$ **(b)** $S_0(d, h)$

Figure 4.17: (a) S_∞ as a function of the diameter d and the gold height h. **(b)** S_0 as a function of d and h. A maximum for $S_0 = 11.8 \pm 0.4\,\mathrm{RIU}^{-1}$ was found for $d = 250\,\mathrm{nm}$ and $h = 75\,\mathrm{nm}$.

Local sensitivity

In order to evaluate the local sensitivity, small layers of silica ($n = 1.45$) with different thicknesses t_{SiO_2} were added conformally on the nanodisk model from figure 4.15. By computing the extinction spectra for increasing t_{SiO_2}, the local sensitivity S_0 was obtained from a linear fit of the λ_{LSPR} as a function of t_{SiO_2}.

The geometrical parameters were then changed in order to investigate the local sensitivity as a function of d and h. The figure 4.17b presents a color map that relates the local sensitivity to the geometrical parameters. It can be observed that a maximum local sensitivity $S_0 = 11.8 \pm 0.4\,\mathrm{RIU}^{-1}$ was obtained for $d = 250\,\mathrm{nm}$ and $h = 70\,\mathrm{nm}$. Therefore, the best performing geometry was assumed as a the standard geometry for the NDA sam-

ples and its synthesis was feasible thanks to the Hole-mask Colloidal Lithography (HCL) technique.

4.4.4 Near field properties

The near field properties were investigated by computing the local electric field when light with $\lambda_{LSPR} = 900\,\text{nm}$ impinges the best performing nanodisk, with diameter of 250 nm and 70 nm gold thickness. In figure 4.18 a top and a side view of the local $|E|$ is depicted. At the top and bottom edges a field enhancement was observed up to 14 times with respect to the incident $\mathbf{E_0}$. The decay of the field intensity was computed by extracting three profile curves at different heights of the nanodisk along radial x direction, as suggested in figure 4.18, and are reported in figure 4.19. It can be observed that a higher field localization occured at the bottom edge than the top one, while at the half height the lowest enhancement was obtained. An exponential fit of the field curves yielded the following decay lengths:

$$l_d^{Bottom} = 18.8 \pm 0.7\,\text{nm} \qquad l_d^{Top} = 27.9 \pm 0.4\,\text{nm} \quad l_d^{Middle} = 63 \pm 2\,\text{nm}.$$

At the bottom, where the enhancement was maximum, also the electric field in the metal was distinguishable and by exponential fitting the skin depth of the field inside gold was found to be $\delta = 5.2 \pm 0.3\,\text{nm}$.

The decay lengths of the localized electric field are much smaller than the edge-to-edge distance between two disks. This confirms that the overlapping of the electrical field from nearest-neighbouring nanodisks is negligible thus the NDA investigated can be considered as the sum of non-interacting single nanodisks.

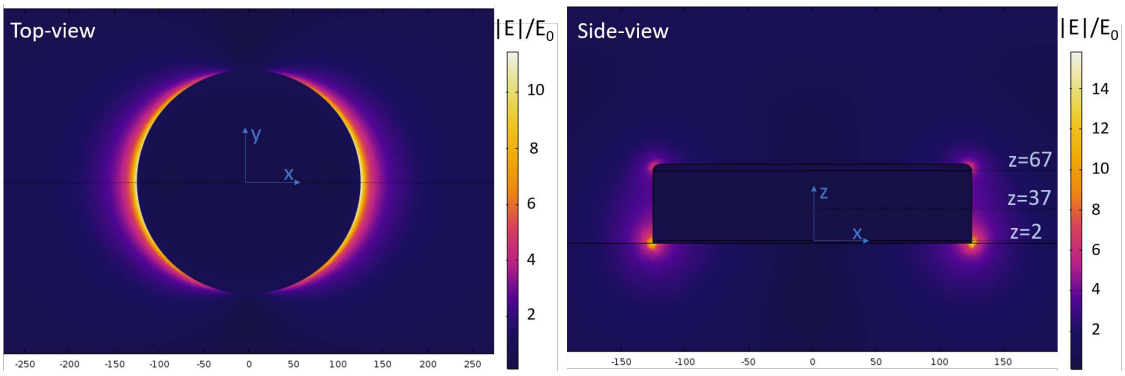

Figure 4.18: Top and side view of the local fields when LSPR occurs. Electric field is enhanced up to 14 times with respect to the incident one, $E_0 = 1\,\text{V/m}$. Profile plots of the electric field are extracted across the dashed lines and reported in figure.

4.5 Conclusions

The expected sensing performances were computed and obtained in this chapter for the ordered NanoHole Array, NanoPrisms Array and NDA. Unit cells with periodic boundary conditions were used to simulate the response of the ordered array while for the NDA the response of a single nanodisk was considered.

Different geometries were investigated to find the best performing one. However, a trade-off had to be made between the expected sensing performances and the feasibility of the synthesis and the measurements of the samples, with the available techniques.

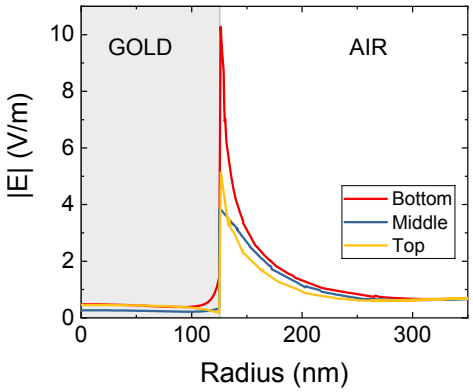

Figure 4.19: Profile plots of the $|E|$ across the radial x direction at three different heights of the nanodisk, bottom ($z = 2\,\text{nm}$), middle ($z = 37\,\text{nm}$) and top ($z = 67\,\text{nm}$).

In table 4.1 the properties of the three simulated nanostructures are summarized.

	NanoHole Array	NanoPrisms Array	NanoDisk Array
Period a (nm)	500	500	-
Gold height (nm)	70	70	70
Width (nm)	300	150	250
λ_{max} (nm)	765	805	900
S_{bulk} (nm/RIU)	280 ± 10	200 ± 10	500 ± 15
S_0 (RIU$^-$1)	3.1 ± 0.1	13.6 ± 0.5	11.8 ± 0.4
l_d (nm)	77 ± 1	10.5 ± 0.5	18.8 ± 0.7

Table 4.1: Summary of the computed properties.

No FEM simulation were carried out instead for the disordered NanoHole Array. It was impossible to do the same assumption as for the NDA and simulate the disordered NanoHole Array (d-NHA) as the sum of sigle nanohole contributions. This was because the plasmonic behaviour is not only given by the localized plasmons of a single hole but is due to the interaction between the Localized Surface Plasmons (L-SP) of the holes and the propagating surface plasmons [15]. One could design a large area of μm^2 with nanoholes distributed according to the Radial Distribution Function from section 3.2.1 and then simulate the response of this large single cell, but this would have a prohibitive computational cost.

In the next chapter, all the 4 nanostructure will be synthesized and their plasmonic properties will be experimentally measured.

5 Synthesis, characterization and sensing performances

In this chapter 4 different plasmonic nanostructures will be presented in detail. The morphological parameters of the nanostructures were investigted in order to find a compromise between the optimization results from Finite Elements Method (FEM) simulations and the experimental feasibility.

For each nanostructure, first the synthesis protocol will be summarised then the sensing properties will be reported by measurements of bulk and local sensitivities.

5.1 NanoPrisms Array

5.1.1 Polystyrene nanosphere self-assembling

The first step for any synthesis process based Nanosphere Lithography (NSL) or Sparse Colloidal Lithography (SCL) is the realization of a monolayer of polystyrene (PS) nanosphere. Mono-dispersed nanoparticles with different diameters were purchased for NSL from Microparticles Gmbh: $248 \pm 9\,\text{nm}$, $340 \pm 9\,\text{nm}$, $522 \pm 12\,\text{nm}$, $1030 \pm 30\,\text{nm}$. Thus, PS nanospheres self-assembled masks can be obtained on freshly cleaned substrates as described in section 3.1.1 and some examples are illustrated in figure 5.1. In particular, 522 nm spheres were able to form wide areas of defectless mask with the same crystallographic direction whereas line and grain boundary defects arise with smaller nanospheres.

Since both the self-assembling of the nanoparticles on the water surface and the drying step of the masks are very sensitive to the environmental conditions, the masks formation was carried out in an isolated chamber with tunable humidity.

A low humidity speeds-up the evaporation of the solvent from the PS mask thus causing line defects, whereas a high humidity slows down the evaporation thus facilitating the formation of wide and defectless areas. In this work, the mask formation has been performed in an environment with a humidity of $\sim 75\%$ and temperature $T_{env} \sim 27°C$.

In figure 5.2 522 nm nanospheres masks are presented. It can be seen by the irridescence that the ordered arrays cover large areas of the substrates($\sim$ cm^2).

5.1.2 Synthesis and characterization of NanoPrisms Array (NPA)

To obtain the NanoPrisms Array samples, the metal was deposited by thermal evaporation through the self-assembled masks and then the nanoparticles were peeled off using an adhesive tape. In order to increase the stability of the nanostructures first a 2 nm chromium layer was evaporated as an adhesion layer then the gold film was added.

Due to its high melting temperature ($T_{melt} = 1857$°C) and thus to the high thermal load needed, Cr thermal evaporation was more challenging with respect to the Au one ($T_{melt} = 1064$°C). However, if the evaporation chamber evacuated down to 10^{-6}mbar, chromium will sublimate directly from the solid phase at temperatures around 1400°C. The typical parameters that were used for Cr/Au thermal evaporation process are reported in table 5.1.

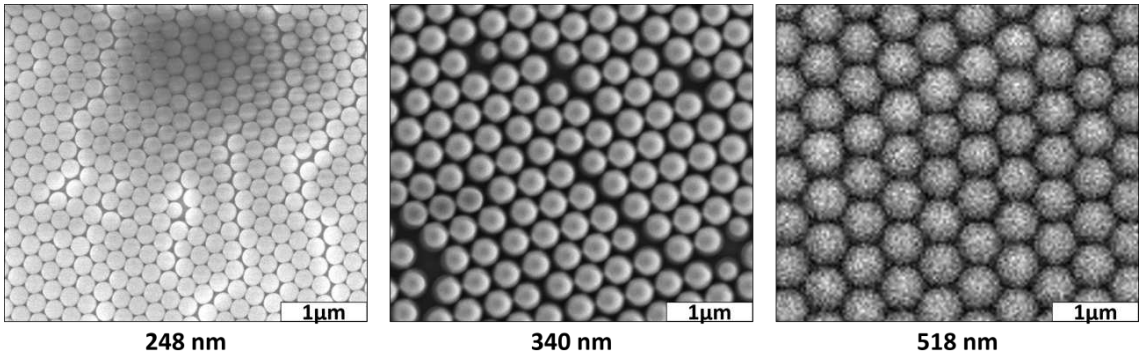

Figure 5.1: Self-assembled masks of PS nanospheres with different diameters: 248 nm, 340 nm and 522 nm.

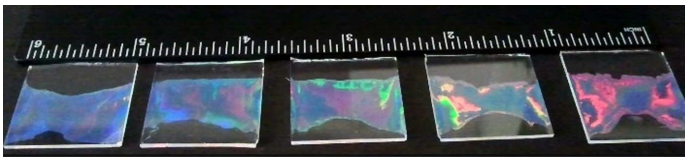

Figure 5.2: PS masks obtained with 522 nm nanospheres. The uniform irridescence suggests that tha array has large ordered domains.

	Pressure [mbar]	Current [A]	Rate Å/s
Cr	$3 \cdot 10^{-6}$	200	1
Au	$1 \cdot 10^{-5}$	120	7

Table 5.1: Thermal evaporation parameters

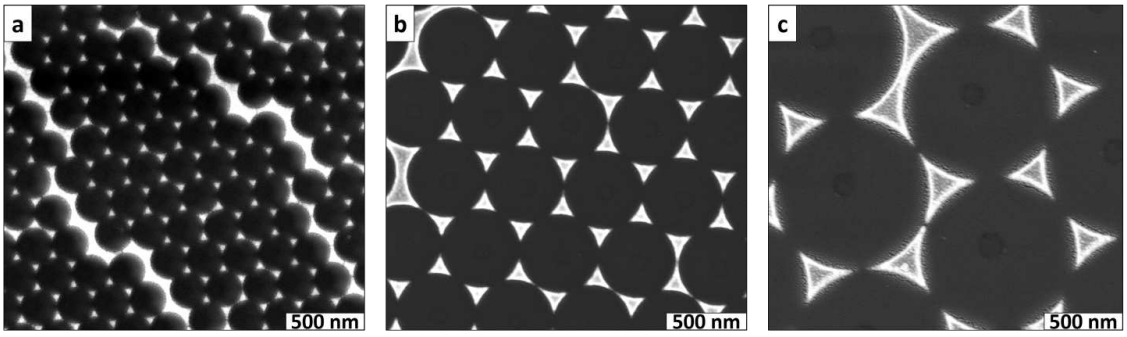

Figure 5.3: NanoPrisms Array obtained by NSL with different nanospheres: (a) 248 nm; (b) 522 nm; (c) 1030 nm

Figure 5.3 shows NPAs obtained with nanoparticles of different diameters, respectively 248 nm, 522 nm and 1030 nm. The lateral size and the lattice constant are defined by the PS nanoparticle dimensions whereas the height was given by the evaporation step. However, there is a maximum height that can be reached for each nanoparticle dimension due to the shrinking of the interstitial area between the nanospheres during the evaporation process. As the metal is deposited through the nanosphere mask, material accumulates at the rim of the triangular shaped interstitial area. The latter shrinks due to the accumulating material until the aperture is shut and so the maximum height of the nanoprism is reached.

The geometrical parameters of the NPA corresponding to the different sphere diameters were measured by image analysis of Scanning Electron Microscopy (SEM) and Atomic Force Microscope (AFM) images and are reported in table 5.2. The linear fit of the maximum height h_{max} and the lateral width L as a function of the nanospere diameter a from figure 5.4 allows to predict the morphology that one can obtain by employing different PS nanosperes with different diameter during the NSL process. The relation found between the width and the lattice constant confirms the assumption $L = 0.3 \cdot a$ that was done in modelling the NPA in the numerical simulations in section 4.3.

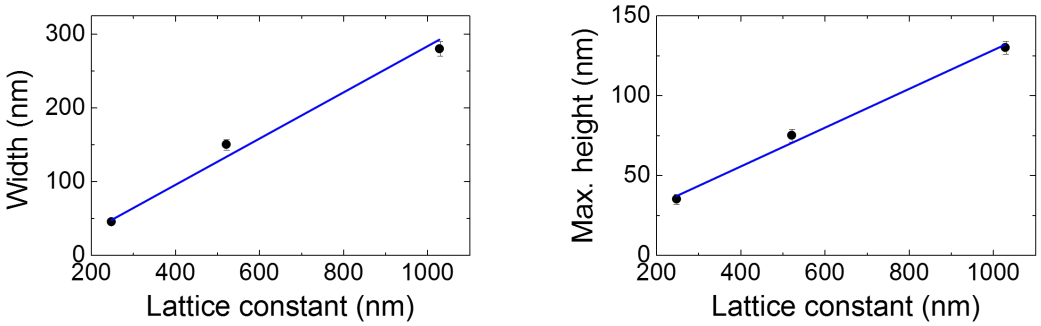

(a) $m = 0.31 \pm 0.03$, $q = -30 \pm 14$ nm **(b)** $m = 0.121 \pm 0.009$, $q = 7 \pm 5$ nm

Figure 5.4: (a) Width L and (b) maximum height h_{max} (b) of NPA as a function of the nanosphere diameter a (lattice constant).

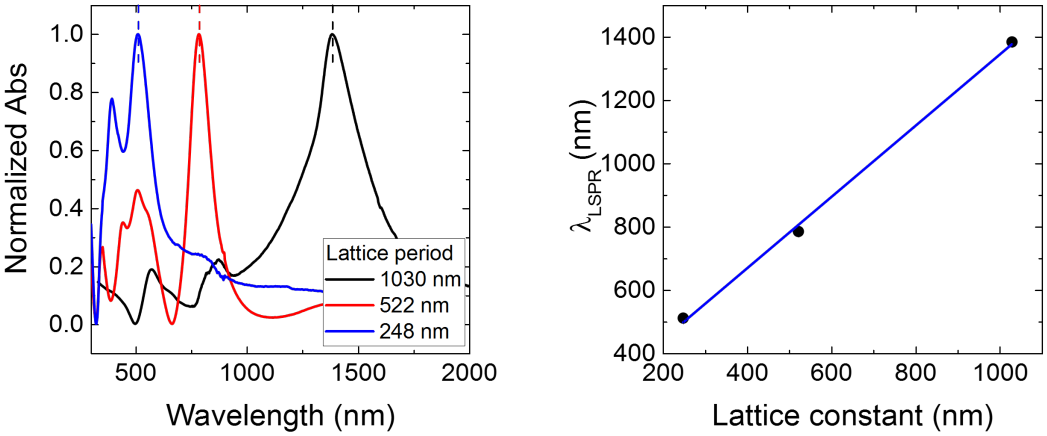

(a) **(b)**

Figure 5.5: **(a)** Absorbance spectra of NPA obtained with different nanospheres: to better highlight the dipolar LSPR peak variation the spectra are normalized in the range [0,1]. **(b)** λ_{LSPR} of spectra in (a) as a function of the lattice constant a.

The absorbance spectra of the synthesized NPAs were measured by using a JASCO V-670 spectrophotometer, that covers the range 300-2600 nm, or an Ocean Optics HR 4000 spectrometer, that covers the range 200-1100 nm. All the measurements were done at normal incidence and with unpolarized light. In figure 5.5a the spectra of the samples from figure 5.3 are presented and their dipolar LSPR peak position was plotted as a function of the lattice constant in figure 5.5b. The parameters obtained from the linear fit, $m = 1.126 \pm 0.005$ and $q = 220 \pm 30$ nm, allow to predict the LSPR wavelength of NPAs

PS diameter (nm)	width (nm)	max. height (nm)	λ_{LSPR} (nm)
248	45 ± 3	35 ± 3	510 ± 1
522	150 ± 7	75 ± 4	784 ± 1
1030	280 ± 10	130 ± 4	1384 ± 1

Table 5.2: Geometry and LSPR peak obtained by NSL with different PS nanosphere diameter.

with the maximum achievable height once the PS nanospere diameter is fixed.

The spectral position of the dipolar Localized Surface Plasmon Resonance (LSPR) peak can be determined in two ways. On one side, the centroid method performs a weighted average of the peak above a given threshold absorbance (A_{th}) and thus the peak position λ_{LSPR} is computed by:

$$\lambda_{LSPR}^{centroid} = \frac{\sum_i \lambda_i \cdot (\mathrm{A}_i - \mathrm{A}_{th})}{\sum_i (\mathrm{A}_i - \mathrm{A}_{th})} \tag{5.1}$$

where λ_i and A_i are respectively the wavelength and the corresponding absorbance.

On the other side, a fit of the data converted in a light energy/absorbance spectrum instead of the wavelength/absorbance one can be done with the Lorentzian function:

$$y(x) = y_0 + \frac{2A}{\pi} \cdot \frac{w}{4(x - x_c)^2 + w^2} \tag{5.2}$$

where x_c represents the peak position.

For the purpose of this work, plasmonic resonances in the NIR that can be investigated by live measurements were needed. By considering the good sensing properties predicted in the previous chapter and also the fact that the resonance peak could be quicky measured by the silicon-based spectrometer (Ocean Optics), the 522 nm PS nanoparticles were the ones that better suited our purposes and they were employed for the NPA synthesis.

Height variation with 522 nm PS nanospheres Once the 522 nm diameter PS nanoparticles were chosen for the NPA fabrication, the variation of the λ_{LSPR} peak position was investigated as a function of the metal height. Gold layers with different thicknesses were evaporated through the PS masks and the absorbance spectra obtained from these samples are reported in figure 5.6a. As the height increases, the λ_{LSPR} blueshifts and their relation is highlighted by the linear fit in figure 5.6b whose parameters are found to be $m = -2.8 \pm 0.1$ and $q = 1007 \pm 7\,\mathrm{nm}$.

5.1.3 Post-treatment of the NanoPrisms Array

In the 250kX zoom SEM image of a 522 nm NPA in figure 5.7, small gold nanoparticles of diameter smaller than 10 nm can be observed at the edges of the nanoprism. These nanosatellites are formed during the thermal evaporation of the metal from atoms that collide on the substrate far from the growing nanoprism thus causing the growth of nanoparticles with few nanometers diameter at the nanoprism's edges. The presence of these nanosatellites broadens the LSPR peak and a post-treatment was necessary to remove the nanosatellites and thus getting a sharper resonance.

Two different treatments are reported here: a physical one, which consists in exposing the NPA to a high concentration salt solution, and a chemical one, which consists in exposing the NPA to a gold etching solution.

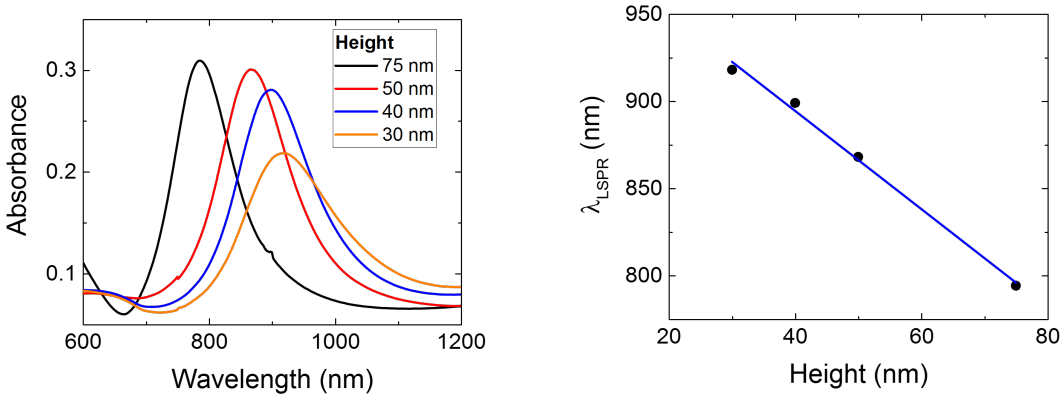

(a) (b)

Figure 5.6: **(a)** Absorbance spectra of NPA with different h. **(b)** λ_{LSPR} of 522 nm NPA as a function of the nanoprisms' height

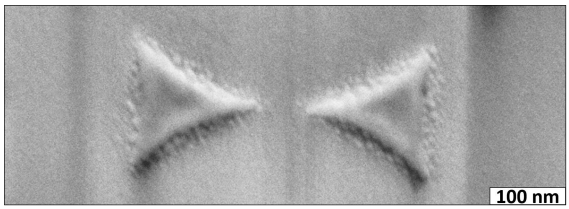

Figure 5.7: 250kX zoom SEM image of a 522 nm NPA

Physical treatment

In order to remove the nanosatellites but also to stress test the NanoPrisms Array by exposing them to solutions that will be further employed in the biosensing process, the samples were immersed in a 0.5 M NaCl saline buffer for 24 hours in a hybridization oven. The Saline Sodium Citrate physiological buffer was used for this purpose in a 3X concentration acqueous solution. The SEM image in figure 5.8a demonstrates that the nanosatellites, whose adhesion to the substrate was minimal with respect to the Cr/Au nanoprisms, were removed. Moreover, a sharper and blueshifted resonance was found after the treatment (figure 5.8b).

A second exposure of the sample to the same buffer treatment did not cause any further modification of the resonance peak. This suggested that the treatment in saline solution was self-limiting and it could be used as standard procedure for obtaining stable nanostructures with sharp resonances.

Chemical treatment

An alternative way to remove the nanosatellites around the NPA was by chemical wet etching with a Gold Etchant solution from Sigma-Aldrich, composed by Potassium Iodide (KI). Due to the high surface/volume ratio of the nanosatellites, these were etched away very quickly with respect to the nanoprisms but, nonetheless, the nanoprisms' sharp tips were slightly rounded by the etchant solution. On the contrary, the saline treament cleaned away selectively only the nanosatellites, who had a worse adhesion to the substrate.

Since the wet etching process is time dependent and the stock solution has a high etching rate, i.e. 2.8 nm/s, dilutions in Milli-Q water were done to decrease the ething rate and

thus making the process controllable and reproducible on time scales of 10-100 s. For our purposes, the stock solution was diluted 1/1000 and the samples were exposed for 1 minute followed by thorough rinsing with Milli-Q water.

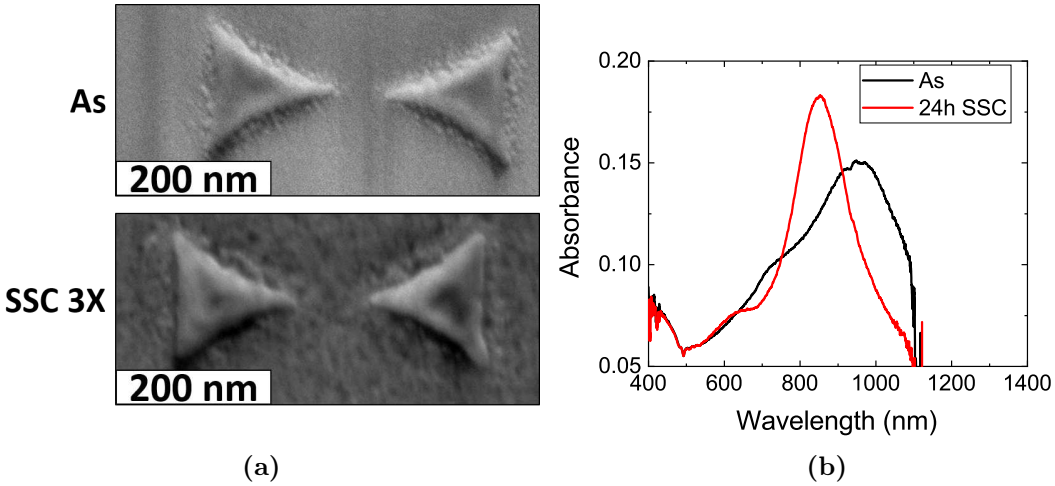

Figure 5.8: **(a)** FE-SEM image of a NPA before and after the 24 h SSC 3X treatment. The satellites around the nanostructures were removed without altering the shape of the nanoprisms. **(b)** Corresponding absorbance spectra of the NPA before and after the SSC 3X treatment.

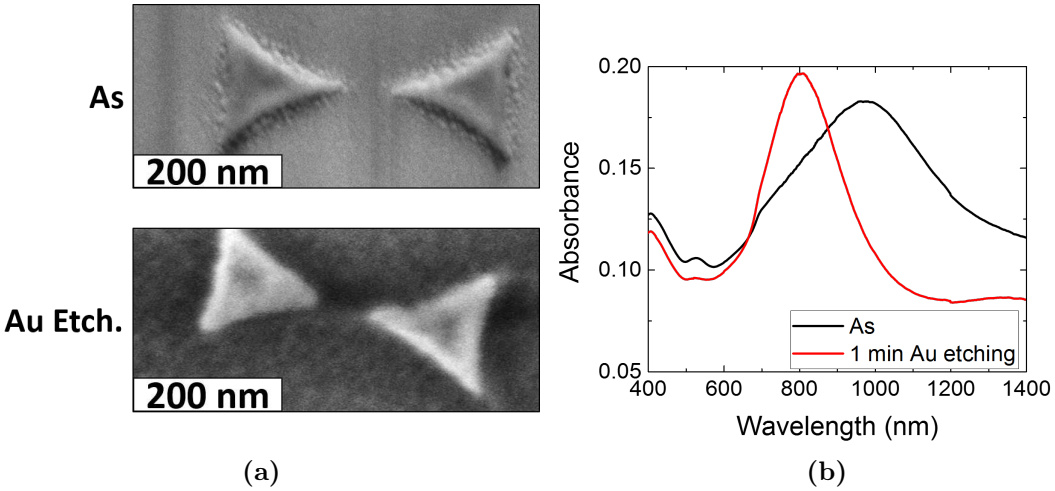

Figure 5.9: **(a)** FE-SEM image of a NPA before and after the Au etching treatment. **(b)** Corresponding absorbance spectra of the NPA before and after Au the etching treatment.

The SEM images in figure 5.9a demonstrate that the nanosatellites were removed but also the prism tips were rounded by the etching action. The resonance peak variation after the etching process can be observed in figure 5.9b. Therefore, the gold etchant treament gave a sharper and blueshifted resonance as for the saline solution treatment.

However, after the etching process the NPA samples were unstable over time. The reasonance peak continued to blueshift even after thoroughly rinsing. A gold etching cleaning process was performed on a gold nanoprism sample, without the chromium layer, in order to check if the oxidizing chromium layer was responsable for the unstability. In figure 5.10a the absorbance spectra of the treated gold nanoprism sample are reported. It is clear that even in the absence of the underlying chromium layer, the gold etchant started

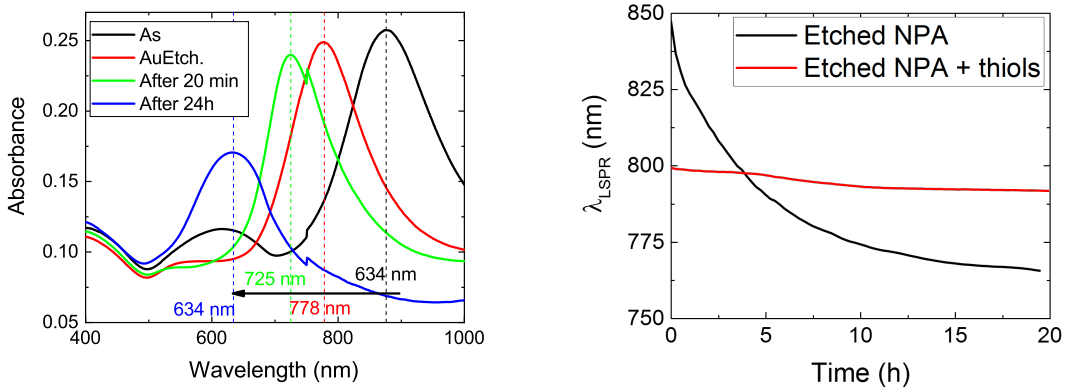

(a) (b)

Figure 5.10: (a) Absorbance spectra of a gold NPA which was etched by gold etchant solution. Blueshifts ware observed after thoroughly rinsing with Milli-Q water even for the gold particle, without the chromium layer. **(b)** λ_{LSPR} time variation for Cr/Au NPA that was exposed to gold etchant. A comparison is made with a NPA protected with an alkanethiols self-assembled layer after the etching.

an irreversible modification of the whole nanoprism morphology. The λ_{LSPR} peak position of the Cr/Au NPA etched sample was monitored for 20 h and the trend is plotted in figure 5.10b (black line). The blueshift of the resonance peak was compatible with an increase of the aspect ratio of the nanoprism due to the degradation of the tips. In order to stop the degenerative process of the etched NPAs a protective layer made by alkanethiols was self-assembled on the gold surface. The freshly etched sample was immersed for 24 h in an ethanol solution of thiols and then the LSPR peak was monitored. The stability of such a functionalized sample was achieved thanks to the covalently bound thiols on the gold surface and this is pointed out in figure 5.10b (red line). Since the self-assembling of the thiol monolayer represents also a step of the biofunctionalization protocol employed in this work, more details regarding it can be found in section 6.1.1.

5.1.4 Bulk sensitivity

The standard NPA sample that was employed in the following experiments consisted in Cr/Au NPAs with 522 nm lattice period and 2/60-75 metal thicknesses that went through one of the post-treatments introduced above. The bulk sensitivity, previously discussed, was obtained by immersing the sample in different liquids and measuring the absorbance spectra. The peak redshift that resulted from measurements in air and in glycerol is shown in figure 5.11 and thus the bulk sensitivity was computed from equation 5.3.

$$S_{\infty}^{NPA} = \frac{\Delta\lambda_{LSPR}}{\Delta n} = 170 \pm 5 \,\frac{\text{nm}}{\text{RIU}} \tag{5.3}$$

The experimental bulk sensitivity resulted smaller with respect to the simulated one ($S_{\infty} = 200 \,\frac{\text{nm}}{\text{RIU}}$).

5.1.5 Local sensitivity

The local sensitivity for the Cr/Au NPA samples was evaluated by depositing thin incremental layers of silica in order to simulate the presence of biological molecules since its

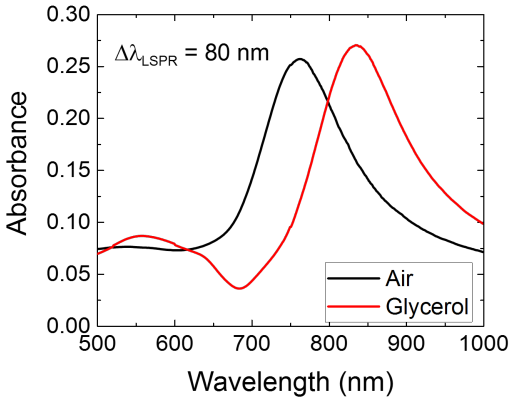

Figure 5.11: Absorbance spectra of the Cr/Au NPA measured in air (n = 1) and in glycerol (n = 1.47).

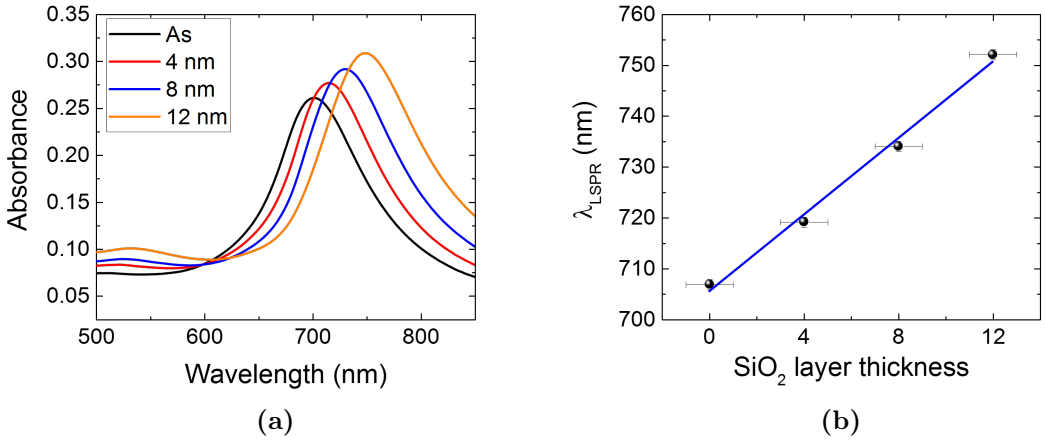

(a) **(b)**

Figure 5.12: **(a)** Absorbance spectra for increasing silica layer. **(b)** Linear fit of λ_{LSPR} against t_{SiO_2}.

refractive index $n_{SiO_2} = 1.45$ is similar to the organic molecules' one ($n \approx 1.5$). Incremental silica layers of thicknesses t_{SiO_2} of 4, 8 and 12 nm were deposited conformally on top of the nanoprisms by magnetron sputtering and the absorbance spectra at each step are reported in figure 5.12a. The resonance peak position λ_{LSPR} as a function of t_{SiO_2} is plotted in figure 5.12b and reported in table 5.3.

A linear fit yielded $m = 3.9 \pm 0.2$ and $q = 707 \pm 2$ nm and therefore the local sensitivity S_0 was computed in equation 5.4:

$$S_0 \equiv \frac{1}{\Delta n}\frac{\partial \lambda}{\partial t}\bigg|_{t=0} = \frac{m}{n_{SiO_2} - n_{Air}} = 8.8 \pm 0.4 \frac{1}{\text{RIU}} \tag{5.4}$$

t_{SiO_2} (nm)	0	4	8	12
λ_{LSPR} (nm)	707	719	734	752

Table 5.3: $\lambda_{LSPR}(t_{SiO_2})$ values. $\sigma = 1$ nm was assigned to λ_{LSPR}

The experimental local sensitivity for the Cr/Au NPA samples resulted smaller than the simulated one in section 4.3 ($S_0 = 13.6 \pm 0.5 \frac{1}{\text{RIU}}$). Since both local and bulk experimental sensitivities are smaller with respect to the simulated ones, this could be ascribed to the shape of the synthesized nanoprisms which does not match perfectly with the designed one. The edges and the tips of the synthesized nanoprisms are less sharp than the modelled ones and this might lead to a not optimal localization of the electric field around the synthesized nanoprisms. This affects especially the local sensitivity which diminishes considerably if the field enhancement decreases due to imperfections.

5.2 Ordered NanoHole Array

As for the NanoPrisms Array, the first step for the ordered NanoHole Array synthesis is the formation of the PS nanosphere self-assembled mask on a substrate. Secondly, the PS nanoparticles are exposed to a Reactive Ion Etching (RIE) process in an Ar/O_2 plasma that reduces the nanospheres diameter without altering the array order. Finally metal is deposited by magnetron sputtering and the nanospheres are removed by scotch tape peeling.

5.2.1 Reactive Ion Etching

Since the pressure, the gas flow and the power of were fixed to the values from table 3.1, time t_{RIE} was the main free parameter for the RIE process. In figure 5.13 PS monolayers etched for increasing time are presented, whereas figure 5.1 shows the close-packed mask before RIE process.

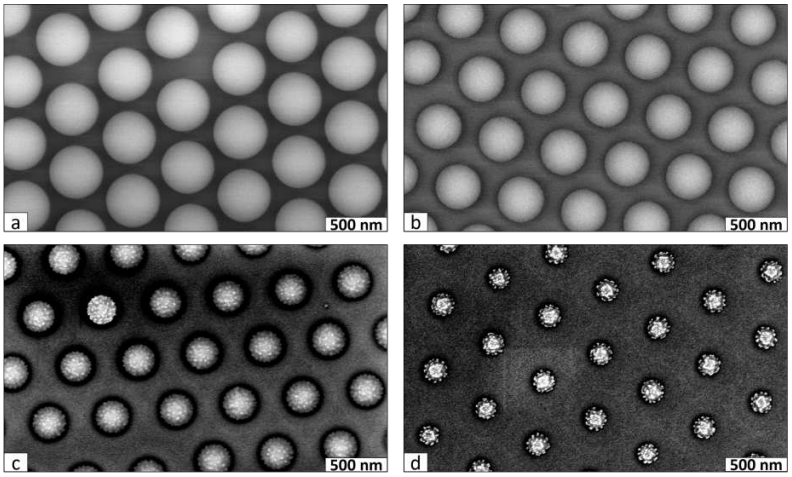

Figure 5.13: 100kX magnification FE-SEM images of 522 nm PS nanosphere masks with different RIE treatment: (a) 6 min, (b) 9 min, (c) 12 min and (d) 15 min.

The diameters of the etched nanospheres can be computed by analysis of the FE-SEM images with ImageJ software. Nanoparticles with different size went through etching processes at increasing time intervals and the etched diameter was plotted against the RIE time. Therefore, calibration curves for the etching of 340 nm, 522 nm and 1030 nm PS nanospheres were obtained by fitting the data with a parabolic function $y = b \cdot x + c \cdot x^2$ in figure 5.14 and the fit parameters are reported in table 5.4.

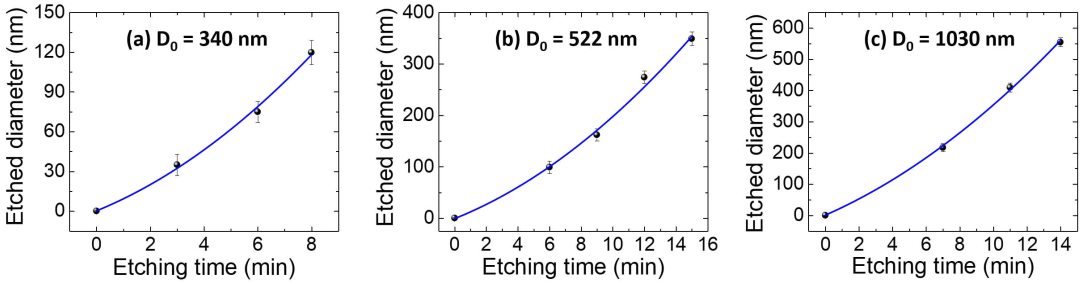

Figure 5.14: Variation of the diameter ΔD against the etching time. Data was fitted with parabolic function for different kind of PS nanoshpheres: (a) 340 nm, (b) 522 nm, (c) 1030 nm.

NP D (nm)	b (nm/min)	c(nm/min^2)
340	8.2 ± 1.7	0.8 ± 0.1
522	11.8 ± 1.6	0.9 ± 0.1
1030	22.6 ± 1.4	1.3 ± 0.1

Table 5.4: Fit parameters for different NP diameter

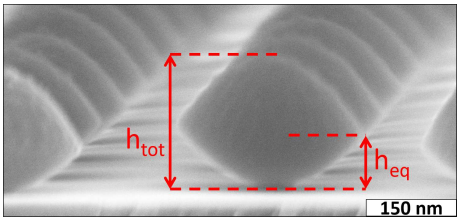

Figure 5.15: Side view of an etched nanosphere.

The shape of the spheres was not preserved during the etching process. On one side the surface roughness increased considerably for long etching processes. On the other side, the etching is not isotropic but the vertical etching rate is higher than the in-plane one, thus leading to lens-like shaped PS nanopartiles after the RIE process. This effect is clearly seen in figure 5.15 where the in-plane diameter is about 300 nm while the total and equatorial height are respectively $h_{tot} \sim 215$ nm and $h_{eq} \sim 90$ nm.

Depositing a metallic layer thicker than h_{eq} would trap the PS nanoparticle beneath thus preventing their removal. Therefore, metallic layers thinner than h_{eq} have been deposited for the ordered NanoHole Array (o-NHA) synthesis. Moreover, an excessive RIE would damage and make collapse the nanoparticles thus preventing again their liftoff after the metal deposition. Therefore the following morphological costraints of the NSL and RIE were found for a nanosphere of initial diameter a, $d \gtrsim a/2$ and $h_{eq} \lesssim a/5$.

5.2.2 Ordered NanoHole Array (NHA) synthesis and characterization

Once the etched nanospheres mask was obtained, a multilayered film was deposited by magnetron sputtering. As for the NPA, first a 2 nm Cr adhesion layer was deposited then the Au layer was added by taking into account the height limitations discussed in the previous section. Finally the nanoparticles were removed by adhesive tape peeling and sonicating in toluene solvent. Figure 5.16 shows o-NHA samples obtained with nanopartiles of diferent diameter, 340 nm, 522 nm and 1030 nm respectively.

The transmittance spectra of these samples are reported in figure 5.17. It is clear how the peak position in the transmittance spectra depends on the initial diameter of the nanosphere, and thus on the lattice constant of the ordered NanoHole Array.

The plasmonic property that the o-NHA exhibits is the extraordinary optical transmission (EOT) that consists in transmitting more light that it would be transmitted ordinary, without any plasmonic mechanism (cf. section 1.5). The ordinary transmission of lights

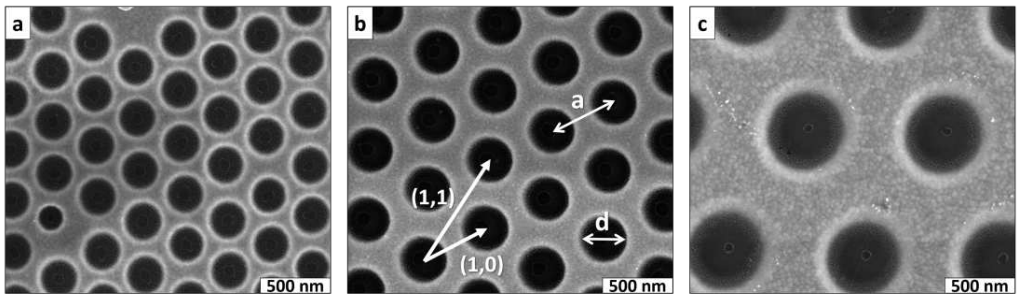

Figure 5.16: ordered NanoHole Array obtained by NSL with different nanospheres: (a) 340 nm, (b) 522 nm, (c) 1030 nm. FE-SEM images with 100 kX magnification.

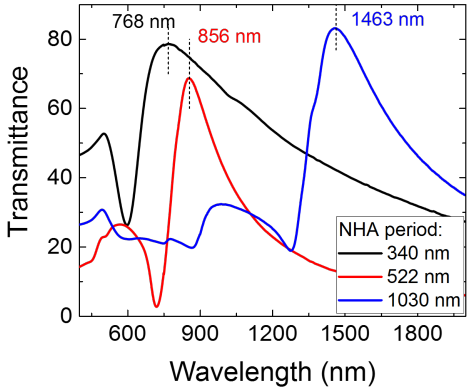

Figure 5.17: Transmittance spectra of NHA with different lattice constant a.

through a pattern of holes is given by the ratio between the in plane area covered by the holes and the total area, namely, the filling factor f. In order to point out the EOT property, the transmittance spectra can be normalized by dividing the %T values by the fillig factor:

$$\%T_{norm} = \frac{\%T}{f}$$

where f for an hexagonal array with a period and d hole diameters is given by

$$f = \frac{A_{Holes}}{A_{NHA}} = \left(\frac{d}{a}\right)^2 \frac{\pi}{2\sqrt{3}}.$$

Figure 5.18 shows the normalized transmittance spectrum of a 522 nm period and 300 nm diameter NHA where transmittance exceeds 100% around the (1,0) peak. The two main peaks in the spectrum correspond to the two main coupling modes that can occur in the NHA. The (1,0) peak correspond to the resonance coupling with the nearest neighbour hole, while the (1,1) peak corresponds to the coupling with second nearest-neighbour hole. Due to its reduced width and higher transmission maximum, the position of the (1,0) peak has been considered as the main resonance wavelength λ_{EOT} for the o-NHA.

To further stress the role of the nanohole patterning of a metallic film in order to achieve plasmonic behaviour, the transmittance spectra of metallic film, 2 nm Cr/ 70 nm Au, is reported in figure 5.19 and this shows how transmittance is negligible in the absence of the o-NHA in the Vis-NIR range and the only resonance feature is due to the cross-over between inter- and intra-band absorption in Au.

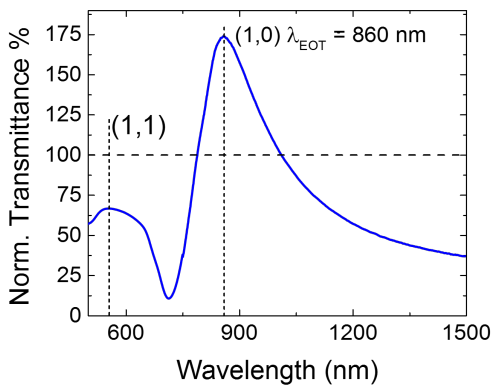

Figure 5.18: Normalized transmittance spectrum.

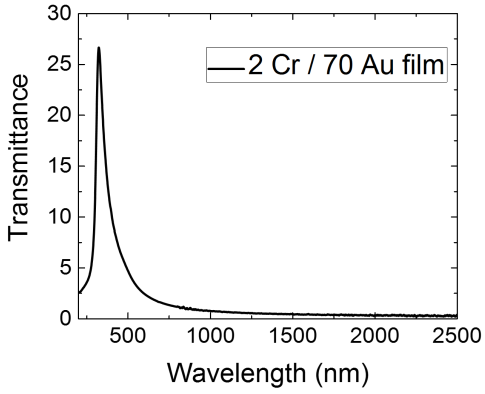

Figure 5.19: Transmittance of a Cr/Au film.

EOT peak analysis There are two ways for determining λ_{EOT} given a transmittance spectrum. The first is the centroid method, introduced previously in section 5.1.2. The second one relies on a more physical interpretation of the asymmetrical EOT transmittance peak. The transmission of light through the NHA could be interpreted as a Fano-like resonance, originating from the quantum interference between two transmission channels [109]. The first one, non resonant, is given by the ordinary transmission of the light above the nanoapertures and the second one which is driven by the resonant coupling of light with the plasmons [110, 111]. Therefore, the Fano formula for the total scattering cross section as a function of energy has been considered and conveniently rewritten. Thus, a formula for the transmittance as a function of the incident wavelength has been computed and presented in equation 5.5

$$T(\lambda) = T_0 + A\frac{q + \sigma\left(\frac{1}{\lambda} - \frac{q\cdot\sigma - \lambda_{EOT}}{q\cdot\sigma\cdot\lambda_{EOT}}\right)^2}{1 + \sigma^2\cdot\left(\frac{1}{\lambda} - \frac{q\cdot\sigma - \lambda_{EOT}}{q\cdot\sigma\cdot\lambda_{EOT}}\right)^2} \tag{5.5}$$

where, λ_{EOT} represents the point of maximum transmittance, σ determines the width of the peak and q represents the Fano parameter, which is the ratio of the amplitudes of resonant scattering to the non-resonant one.

Comparing the centroid and the Fano fit method, the second one is more advisable since it represents a global fit of the curve based on a physical interpretation of the phenomenon. Therefore, the λ_{EOT} of the transmission spectra of the NHA were obtained directly from the Fano fit function.

For the purpose of this work, the morphology of the o-NHA had to be tuned in order to achieve the best sensing performances. By taking into account the extensive investigation of the sensing properties by numerical simulations in section 4.2 the best performances are achieved with a period $a = 500$ nm, a diameter $d = 300$ nm and a height of the gold layer $t_{Au} = 70$ nm. These parameters were used as a reference for the synthesis of the o-NHA samples employed in the following experiments. Therefore, 522 nm PS nanospheres were employed for the o-NHA synthesis by etching them to a diameter down to 290-310 nm range and then Cr/Au metallic layer was sputtered up to 70 nm of Au.

Post-treatment of the o-NHA

After the metal deposition, nanosatellites were observed around the nanostructure as for the NPA. In order to clean the nanosatellites from the bottom of the nanohole, the o-NHA was immersed for 5 seconds in 1% gold etchant solution and then thoroughly rinsed in Milli-Q water. Figure 5.20 shows FE-SEM images of o-NHA before and after the gold etching treatment and it can be clearly observed that nanosatellites are removed completely. With respect to the NPA, the gold etching did no start a degenerative process of the o-NHA. This was due to it's higher stiffness with respect to the NPA, and no stabilization was needed immediatly after the cleaning.

As for the NPA, cleaning the nanosatellites around the nanostructure produced a much sharper and more intense plasmonic resonance. Figure 5.21 shows the transmittance spectra before and after the gold etchant treatment and the improvement of the EOT peak is clear. Therefore, every o-NHA employed for sensing measurements in this work was first cleaned in the gold etchant solution.

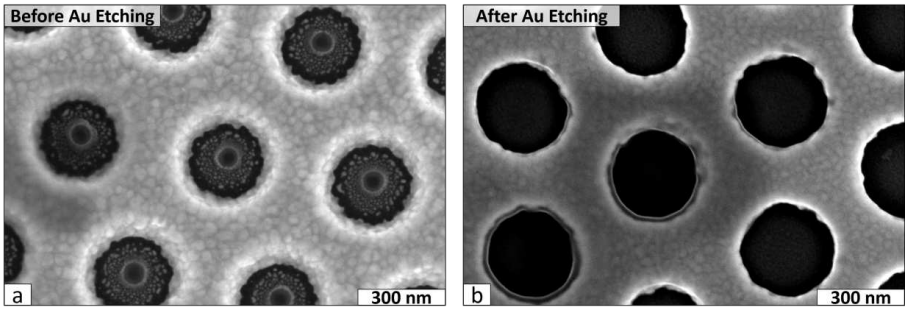

Figure 5.20: FE-SEM images of o-NHA before and after the gold etching treatment. Nanosatellites are removed completely from the bottom of the hole.

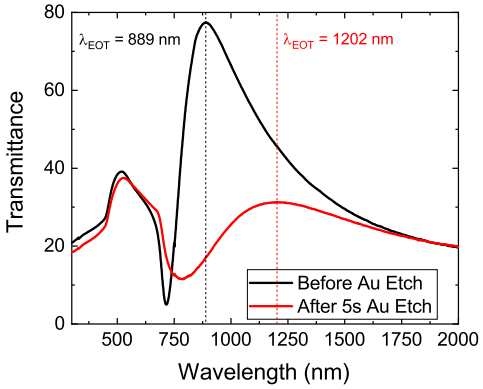

Figure 5.21: Transmission spectra of an o-NHA before and after the 5 second gold etchant cleaning.

5.2.3 Ordered NHA bulk sensitivity

The bulk sensitivity for the standard o-NHA sample was obtained by measuring the transmittance spectrum of the same sample in air ($n = 1$), in water ($n = 1.33$) and in

glycerol ($n = 1.47$). The spectra obtained for the different environments are shown in figure 5.22 whereas in table 5.5 the values of λ_{EOT} computed for each n_{env} are reported.

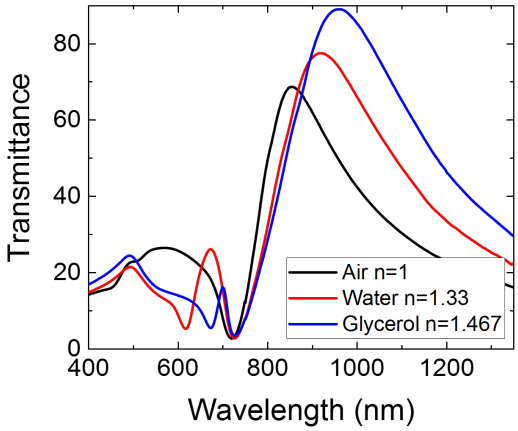

Figure 5.22: o-NHA spectra with different n_{env}.

n_{env}	λ_{EOT}
$n_{air} = 1$	857 ± 1 nm
$n_{H_2O} = 1.33$	920 ± 1 nm
$n_{gly} = 1.47$	961 ± 1 nm

Table 5.5: Computed λ_{EOT} from figure 5.22.

A linear fit of the λ_{EOT} as a function of n_{env} with $y(x) = m \cdot x + q$ returns $m = 230 \pm 25$ nm/RIU and $q = 630 \pm 40$ nm. Finally the bulk sensitivity is computed in equation 5.6 and it is in good agreement with the simulated one in the previous chapter ($S_\infty^{simulation} = 280 \pm 10 \frac{\text{nm}}{\text{RIU}}$)

$$S_\infty = m = 230 \pm 25 \frac{\text{nm}}{\text{RIU}} \tag{5.6}$$

5.2.4 Ordered NHA local sensitivity

As for the NPA, the local sensitivity S_0 was evaluated by adding thin layers of silica with increasing thicknesses in order to simulate the binding of the organic molecules. Specifically, layers of 5 nm, 15 n and 25 nm of SiO_2 were deposited by magnetron sputtering and the EOT peak λ_{EOT} was registered as a function of the increasing dielectric layer t_{SiO_2}. In figure 5.23a the transmittance spectra for different t_{SiO_2} are presented, while in figure 5.23b λ_{EOT} was plotted against t_{SiO_2} and thus fitted with a linear function $y = m \cdot x + q$.

In table 5.6 the corresponding t_{SiO_2} and λ_{EOT} are reported. The linear fit resulted in $m = 1.21 \pm 0.07$ and $q = 853 \pm 1$ nm and finally the local sensitivity S_0 is computed in equation 5.7. The resulted $S_0 = 2.7 \pm 0.2\,\text{RIU}^{-1}$ is in very good agreement with the local sensitivity previously computed by numerical simulation for a similar NHA morphology ($S_0^{simulation} = 3.1 \pm 0.1 \frac{1}{\text{RIU}}$).

$$S_0 = \frac{m}{\Delta n} = \frac{m}{n_{SiO_2} - n_{air}} = 2.7 \pm 0.2 \ \frac{1}{\text{RIU}} \tag{5.7}$$

t_{SiO_2} (nm)	0	5 ± 1	15 ± 1	25 ± 1
λ_{EOT} (nm)	854 ± 1	858 ± 1	870 ± 1	884 ± 1

Table 5.6: λ_{EOT} obtained for increasing layer silica.

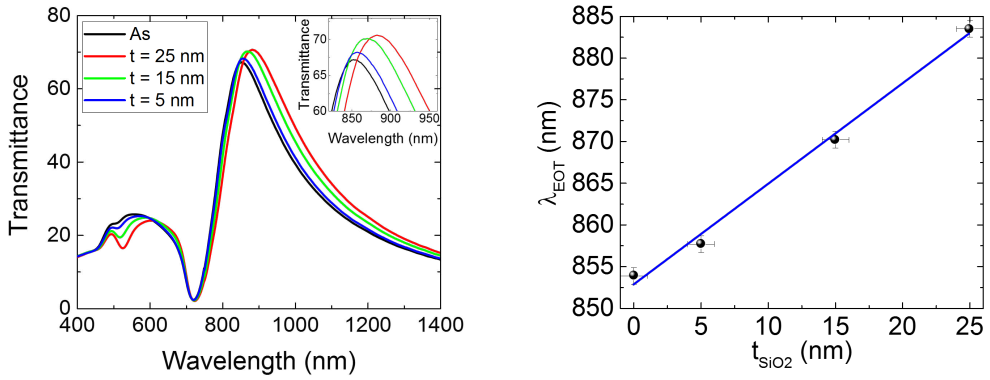

(a) (b)

Figure 5.23: **(a)** Transmittance spectra for increasing silica layer. **(b)** λ_{EOT} against the increasing silica layer t_{SiO_2}.

5.3 Disordered NanoHole Array

In order to directly compare the o-NHA standard sample with a disordered one with similar morphology, charged PS nanoparticles with a diameter of 300 nm were employed for the SCL. As previously explained in 3.2.1, the main parameter for tuning the surface coverage during the mask deposition is the nanoparticle solution. A decreasing particle concentration produces lower surface coverage whereas adding small amount of NaCl screens the Coulombian repulsion between the nanoparticle thus increasing the surface coverage.

5.3.1 Synthesis and characterization of disordered NanoHole Array (d-NHA)

Firstly, two solution with different particle concentration were used for mask formation of freshly cleaned Si or SLG substrates. After exposing the substrates to the 3 polyelectrolytes, solutions with $[NP] = 0.2\%$ w/w and $[NP] = 0.02\%$ w/w particle concentration were deposited and left to adsorbe for 15 minutes in order to reach the saturation time. Then samples were rinsed, immersed in water in a sealed container, put in oven at 120°C for one hour and finally dried with N_2 gas. The figure 5.24 shows FE-SEM images at two different magnification for both kind of samples.

It can be observed that the higher concentration produced more uniforlmy distributed nanoparticle masks whereas in the lower concentration sample disuniformities arose in the mask. The Radial Distribution Function (RDF) functions were computed for both kind of samples by analyzing 5kX magnification FE-SEM images (area $\sim 2500\,\mu m^2$) and were plotted in figure 5.25.

The two RDF plots highlight the structural differences between the two masks. The RDF of the sample with higher [NP] presented a shell structure within 1500 nm distances. The first main peak corresponds to the average distance between neighbouring nanospheres that is $r_{avg} = 520 \pm 10$ nm while the second one corresponds to the distance of the shell of the second nearest neighbor particles, $r_{2ndNN} = 1065 \pm 20\,\text{nm}$ that is about twice the r_{avg}. On the other hand, for larger distances $g(r)$ converges fastly to 1 meaning that the particles are uniforlmy distributed at large scales.

Also the 0.02% concentration RDF presented a main peak that, as expected, gives larger average distance, $r_{avg} = 635 \pm 10\,\text{nm}$. However the presence of a small peak at about 300

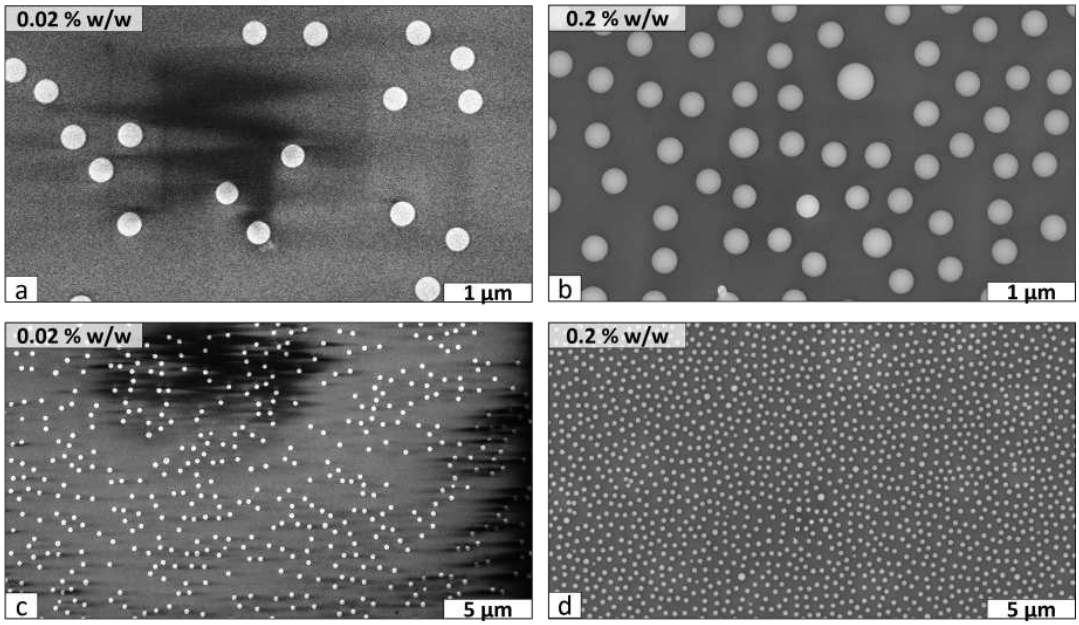

Figure 5.24: FE-SEM images of PS nanoparticle mask obtained with different concentration of the nanoparticle solution: (a) and (c) correspond to the 0.02% w/w particle solution whereas (b) and (d) correspond to the 0.2% one. A uniform dispersion was obtained with the latter while disuniformities arose with the less concentrated solution.

nm highlight the presence of some aggregated particles whereas the noisy $g(r)$ at distances $r > 2000\,\text{nm}$ can be related to a limited sampling statistics.

The surface coverages σ for the two particle concentrations have been computed from $\sigma = \frac{\text{Particles area}}{\text{Total area}}$ and the following values were obtained:

$$[NP] = 0.02\% \quad \sigma_{0.02\%} = (6.3 \pm 0.1)\% \;\Big\|\; [NP] = 0.2\% \quad \sigma_{0.2\%} = (20.8 \pm 0.3)\%$$

In order to increase the surface coverage, instead, different concentrations of NaCl were added to the 0.2% w/w nanoparticle solution. Therefore, three acqueous solutions of charged PS nanospheres were prepared respectively with 0.1 mM, 0.5 mM and 2 mM NaCl concentrations and were deposited on freshly cleaned Si and SLG substrates. Figure 5.26 shows a sample for each NaCl concentration and points out that the higher was the salt concentration the more nanoparticles aggregated.

Since the aggregation of the nanoparticles prevents good quality fabrication of the d-NHA, for their synthesis, only, the 0.1 mM NaCl particle solution and salt-less one were employed. Table 5.7 summarizes the surface coverages obtained for the particle monolayers described in this section.

Nanoparticle concentration	Surface coverage σ (%)
0.02%	6.3 ± 0.2
0.2%	20.8 ± 0.5
0.2% + 0.1mM NaCl	25 ± 1
0.2% + 0.5mM NaCl	31 ± 1
0.2 + 2mM NaCl	40 ± 2

Table 5.7: Surface coverages obtained from SCL with different nanoparticles solutions.

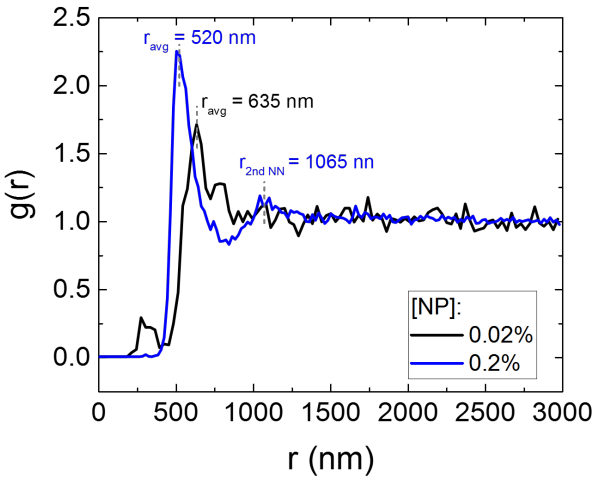

Figure 5.25: RDF of the PS mask samples from figure 5.24 computed on 5kX magnification images of $\sim 2500\,\mu m^2$ area.

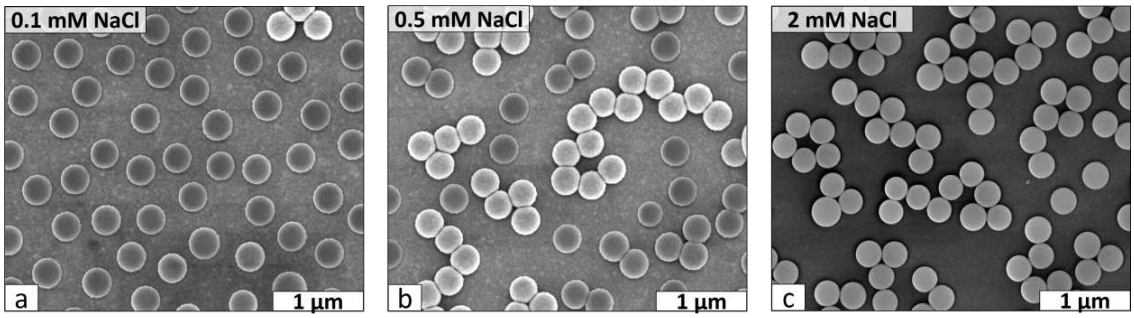

Figure 5.26: PS nanoparticle masks obtained from particles solution with different NaCl concentration.

Figure 5.27 compares the RDF computed for the 0.2% [NP] sample and the one with same [NP] but 0.1mM NaCl added. The former has an average distance $r_{ave} = 520 \pm 10\,nm$ while for the latter $r_{ave} = 480 \pm 10\,nm$ has been found. Therefore, the addition of salt results in a more packed nanoparticle monolayer though causing the aggregation of some particles.

A metallic film has been deposited by magnetron sputtering, as for the o-NHA, with thicknesses of 2 nm for Cr and 70 nm for Au. Finally, the nanospheres have been removed by adhesive tape peeling and samples have been sonicated in toluene.

Figure 5.28a shows the transmittance spectra of d-NHA obtained from the NP masks mentioned above. The small difference between the two masks observed in figure 5.27 was also confirmed by the only $\sim 30\,nm$ difference in the transmission peak position. Since no evident advantage was achieved by adding 0.1 mM NaCl to the PS particle solution, the salt-less one has been employed for the synthesis of the standard d-NHA samples.

As for the o-NHA, an additional cleaning step was performed by immersing the d-NHA samples for 5 s in 1% Gold Etchant solution in order to remove the nanosatellites at the bottom of the nanohole and thus a sharper transmittance peak was obtained. Figure 5.28b shows the transmittance peak of a d-NHA obtained with 0.2 % w/w particle solution and 2 nm Cr/ 70 nm Au metallic layer before and after the gold etchant.

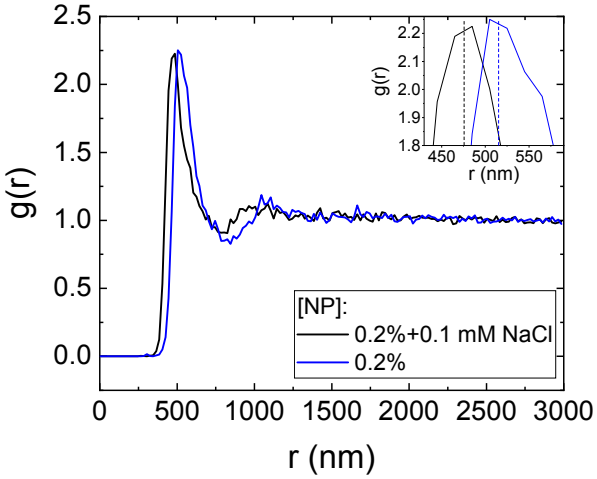

Figure 5.27: RDF comparison between the PS mask obtained with two different particle solution: [NP]=0.2% and [NP]=0.2% +0.1 mM NaCl. The former had a $r_{ave} = 520 \pm 10\,\text{nm}$ whereas the latter $r_{ave} = 480 \pm 10\,\text{nm}$.

Transmittance peak analysis The extraordinary optical transmission was defined as a light transmission mechanism that relies on the plasmonic coupling in a ordered array of nanoapertures. Figure 5.29 reports a direct comparison between the normalized spectra of an ordered and a disordered standard NHA sample. The different shape of the peak and a maximum transmittance smaller than 100% points out that the transmittance peak of the disordered samples doesn't represent an EOT phenomenon. This also stresses that long-range order is fundamental to turn on the EOT mechanism.

The presence of a transmittance peak despite the lack of long range order is, however, related to a plasmonic phenomenon that relies on Extended Surface Plasmons (E-SP) [15]. Thanks to a short range order, a weak plasmonic coupling arises between a hole and its first neighbouring holes positioned at an average distance of $r_{ave} \simeq 520\,\text{nm}$. For this reason, the previously introduced Fano-fit method has been employed also to define the spectral position λ_{max} of the transmittance peak for the d-NHA.

5.3.2 Bulk sensitivity

The bulk sensitivity of the standard d-NHA was obtained by measuring the transmittance spectrum of a sample in air ($n = 1$), in water ($n = 1.33$) and in glycerol ($n = 1.47$). Figure 5.30 shows the transmittance spectra measured in different environments while in table 5.8 the corresponding peak positions are reported. A linear fit with $y = m \cdot x + q$ of this data returns allowed to estimate the bulk sensitivity of the d-NHA

$$S_\infty = m = 200 \pm 15 \frac{\text{nm}}{\text{RIU}}.$$

5.3.3 Local sensitivity

The local sensitivity of a standard d-NHA sample was investigated by depositing conformal layers of SiO_2. Transmittance spectra were measured with different thicknesses of silica layer, specifically 6 nm, 18 nm and 31 nm, and are reported in figure 5.31a. The corresponding peak positions are listed in table 5.9 and are plotted against the silica thickness

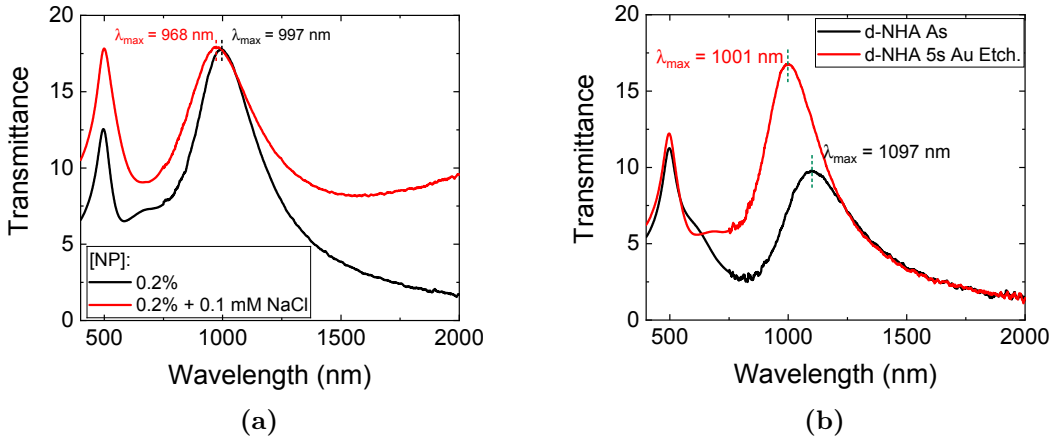

Figure 5.28: **(a)** Spectra of d-NHA obtained from 0.2% particle solution with and without the addition of NaCl. **(b)** Transmittance spectra of a d-NHA before and after the gold etchant treatment.

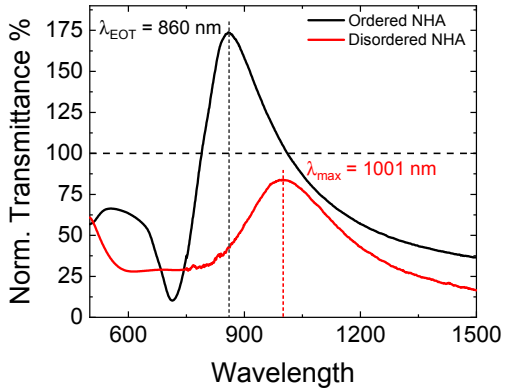

Figure 5.29: Normalized transmittance spectra of an o-NHA and a d-NHA with similar morphology (2 Cr/70 Au nm film, 290 nm diameter and hole interdistance ~ 520 nm).

in figure 5.31b. A linear fit with $y = m \cdot x + q$ of the data returned $m = 0.79 \pm 0.03$ and $q = 1093 \pm 1$ nm and thus the local sensitivity results:

$$S_0 = \frac{m}{\Delta n} = \frac{m}{n_{SiO_2} - n_{air}} = 1.76 \pm 0.07 \frac{1}{\text{RIU}} \tag{5.8}$$

t_{SiO_2} (nm)	0	6 ± 1	18 ± 1	31 ± 1
λ_{max} (nm)	1093 ± 1	1097 ± 1	1108 ± 1	1117 ± 1

Table 5.9: λ_{max} obtained for increasing SiO_2 layer thickness t_{SiO_2}.

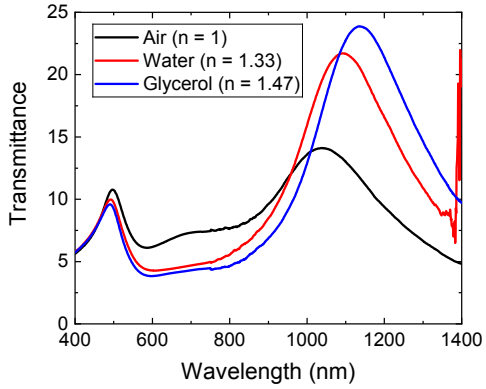

Figure 5.30: %T spectra measured in different environments.

n_{env}	λ_{max}
$n_{air} = 1$	1038 ± 1 nm
$n_{H_2O} = 1.33$	1092 ± 1 nm
$n_{gly} = 1.47$	1136 ± 1 nm

Table 5.8: λ_{max} obtained for different n_{env}.

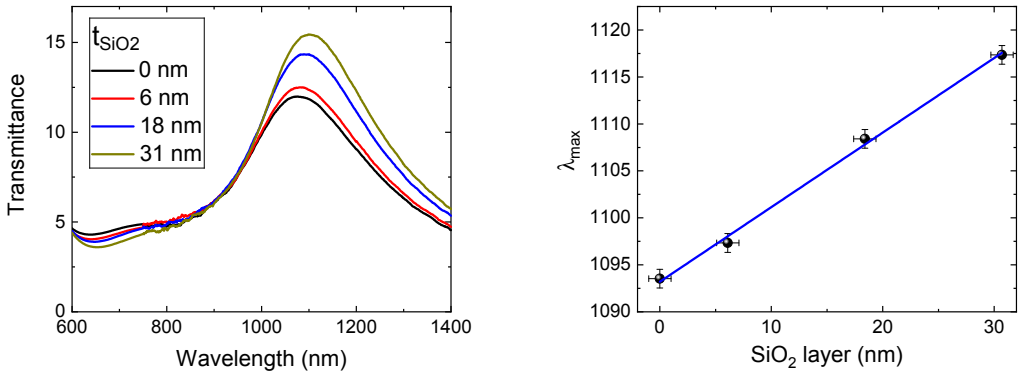

(a) **(b)**

Figure 5.31: (a) Transmittance spectra for increasing SiO_2 layer thickness t_{SiO_2}. **(b)** Linear fit of λ_{max} from (a) as a function of t_{SiO_2}.

5.4 Nanodisk array

5.4.1 Synthesis and characterization

For the NanoDisk Array (NDA) synthesis, as previously described in section 3.2.3, firstly a 100 nm thick Poly(methyl methacrylate) (PMMA) layer was spin-coated on freshly cleaned Si and SLG substrates. In order to obtain non interacting nanodisks the interdistance between the nanostructure has to be much larger than the decay length of the local electric field around the nanodisk. By taking into account the l_d obtained from FEM computations in section 4.4, the interdistance of ~ 520 nm obtained with 0.2 % w/w salt-less nanoparticle solution was large enough to produce non-interacting disks. Therefore, this solution was used for the formation of the monolayer mask on the PMMA layer.

Figure 5.32 shows a disordered mask formed on a PMMA layer and the corresponding RDF. The r_{avg} computed was slightly larger that the one for the monolayers obtained on SLG substrates and this might be due to the fact that before the deposition of the nanoparticle solution on the SLG substrate was exposed to a triple layer of polyelectrolyte solutions whereas the PMMA was exposed only to one, the Poly(diallyldimethylammonium chloride) (PDDA), as suggested by the work of Fredriksson et al. [16]. Thus, a less packed

monolayer with a 590 nm interdistance assures that interdistances are large enough for the non interacting NDA.

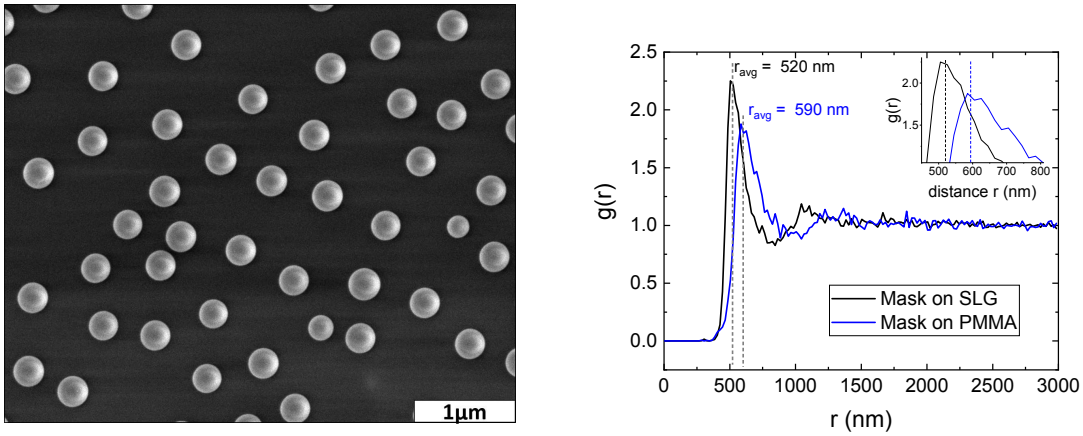

(a) (b)

Figure 5.32: (a) A disordered PS nanoparticle monolayer obtained on a PMMA substrate. **(b)** The RDF comparison between nanosphere mask obtained with the same particle solution on, respectively, a SLG and a PMMA layer. The mask on the PMMA layer results less packed thus assuring again that $r_{avg} \gg l_d$

Once the PS nanoparticle mask was formed, a 20 nm of Cr was deposited by magnetron sputtering and nanospheres were removed by adhesive tape peeling, thus obtaining the hole mask on the PMMA layer. A RIE process with Ar/O_2 plasma was performed at 7 W for 10 minutes in order to etch the PMMA inside the nanoapertures. A layer of 2 nm Cr and 70 nm Au were deposited by thermal evaporation and, finally, the NDA was obtained after the lift-off of the sacrificial layer by sonicating for 5 minutes in 50°C toluene.

Figure 5.33 shows an AFM image of an NDA and its corresponding spectrum. The NDA has a center-to-center disk interdistance of 590 nm, 70 nm total height and 250 nm diameter. Since it is an array of three-dimensionally confined nanostructures, the optical property is given by a plasmonic resonance peak in the absorbance spectrum as for the NPA that is the localized surface plasmon resonance. The position of the resonance peaks λ_{LSPR} was then monitored by the centroid method.

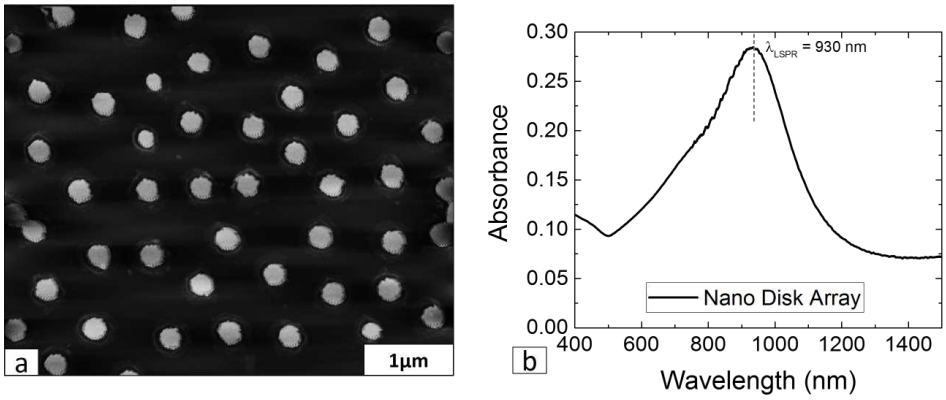

Figure 5.33: (a) AFM image of a NDA sample with 590 nm average distance, 250 ± 10 nm diameter and 70 nm total height. **(b)** The corresponding absorbance spectrum of the sample in (a).

Post-treatment of the NDA

The cleaning treament employed for the NDA was the same of the NPA one. Since gold etchant resulted too aggressive, a 24h treatment in SSC 3X solution was performend on the NDA samples in order to clean away nano-satellites around the disk as it can be observed in figure 5.34a. The corresponding spectra of the NDA sample before and after the treatment is reported in figure 5.34b and it can be observed that the cleaning treatment blueshifted the LSPR peak of about 130 nm. This treatment shifted the LSPR resonance peak in our range of interest that was 750 - 900 nm thus allowing fast optical measurements with Ocean Optics HR 4000 spectrometer.

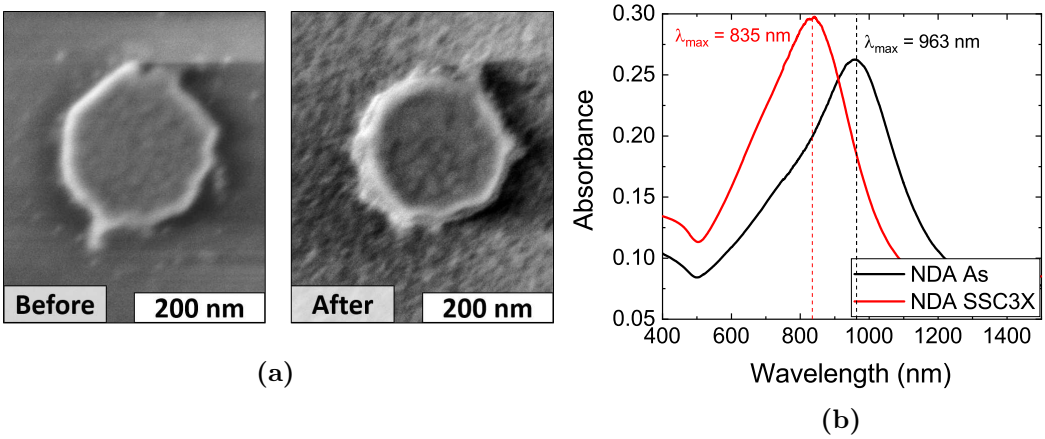

Figure 5.34: **(a)** FE-SEM images of a nanodisk before and after the 24h SSC 3X treatment. Small nanoclusters around the nanodisk were cleaned away. **(b)** Absorbance spectra before and after the cleaning.

5.4.2 Bulk sensitiviy

The bulk sensitivity of the NanoDisk Array was obtained by measuring the absorbance spectrum in air, in water and in ethanol ($n_{EtOH} = 1.36$). The measured spectra are presented in figure 5.35a and the shift $\Delta\lambda_{LSPR}$ is reported as a function of the refractive index in figure 5.35b. The bulk sensitivity is then obtained by a linear fit of the data:

$$S_\infty = 505 \pm 8 \frac{\text{nm}}{\text{RIU}}.$$

5.5 Local sensitivity

In order to compute the local sensitivity for the NDA samples increasing layers of SiO_2 were deposited by magnetron sputtering and the peak position was monitored by centroid method for different thicknesses t_{SiO_2} of $5, 9, 14, 21$ nm. The corresponding absorbance spectra are reported in figure 5.36a and the relative shift of the centroid of peak is presented as a function of t_{SiO_2} and fitted in figure 5.36b. The linear fit with $y(x) = m \cdot x + q$ returned $m = 3.5 \pm 0.1$ and $q = 0.2 \pm 1.2$ nm and so local sensitivity is:

$$S_0 = \frac{m}{\Delta n} = 7.8 \pm 0.2 \frac{1}{\text{RIU}}$$

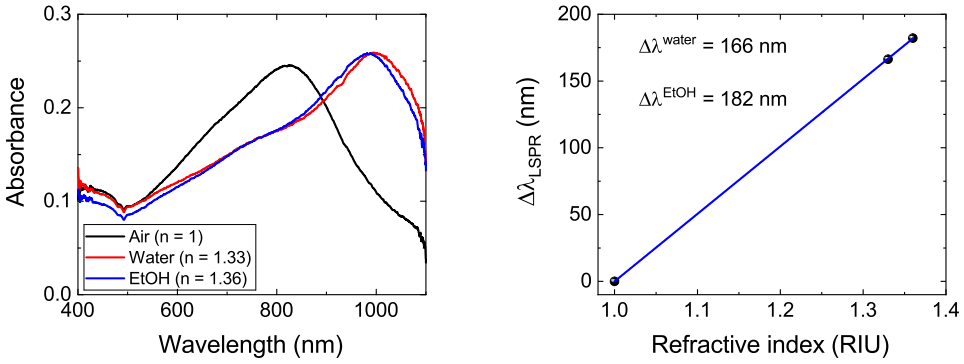

(a) (b)

Figure 5.35: (a) Absorbance spectra of NDA measured in different environments: air, water and ethanol. **(b)** The relative shift of the λ_{LSPR} from (a) as a function of n_{env}. Linear fit of the data returned $m = 505 \pm 8 \frac{\text{nm}}{\text{RIU}}$ and $q = -505 \pm 2\,\text{nm}$.

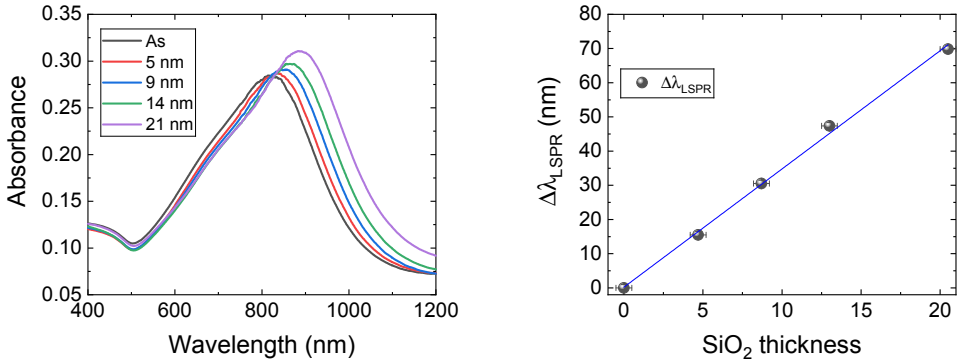

(a) (b)

Figure 5.36: (a) Absorbance spectra of NDA sample for increasing silica layer deposited above. **(b)** Centroid shift of the absorbance peak as a function of t_{SiO_2} with corresponding linear fit of the data.

5.6 Conclusions

In this chapter the synthesis of 4 kinds of nanostructures was presented, two by the Nanosphere Lithography and two by Sparse Colloidal Lithography. The optimal parameters for the synthesis of the nanostructure were chosen by taking into account the FEM simulations from the previous chapter and the request of obtaining a plasmonic resonance in a wavelength range of 750 - 900. Further cleaning steps were added to the synthesis protocol of each nanostructure in order to clean away the surrounding metallic nanoclusters that broaden the plasmonic resonances.
Once a standard morphology was defined for each nanostructure, their sensing properties were investigated by computing bulk and local sensitivities.

The samples employed for the biosensing measurements in the next chapters were synthesized accordingly to the standard samples that were defined here. In conclusion, the standard morphology and the corresponding sensing performances are here summarized.

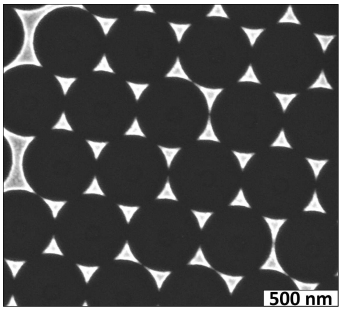

NanoPrisms Array	
Plasmonic property	LSPR
Lattice constant	522 nm
Metallic layer	2 nm Cr + 60-75 nm Au
Post-treatment	24h in SSC3X
Bulk sensitivity	170 ± 5 nm/RIU
Local sensitivity	8.8 ± 0.4 RIU^{-1}

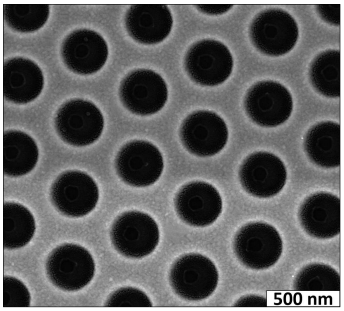

ordered NanoHole Array	
Plasmonic property	EOT
Lattice constant	522 nm
Diameter	290 - 310 nm
Metallic layer	2 nm Cr + 60-75 nm Au
Post-treatment	5s in 1% Au Etchant
Bulk sensitivity	230 ± 25 nm/RIU
Local sensitivity	2.7 ± 0.2 RIU^{-1}

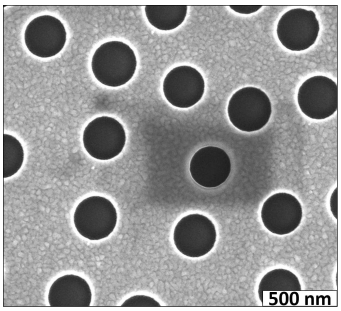

disordered NanoHole Array	
Plasmonic property	E-SP
Average interdistance	520 nm
Diameter	270 - 300 nm
Metallic layer	2 nm Cr + 60-75 nm Au
Post-treatment	5s in 1% Au Etchant
Bulk sensitivity	200 ± 15 nm/RIU
Local sensitivity	1.8 ± 0.1 RIU^{-1}

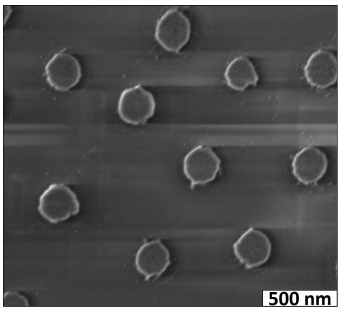

NanoDisk Array	
Plasmonic property	LSPR
Average interdistance	590 nm
Diameter	240-270 nm
Metallic layer	2 nm Cr + 60-75 nm Au
Post-treatment	24h in SSC3X
Bulk sensitivity	505 ± 8 nm/RIU
Local sensitivity	7.8 ± 0.2 RIU^{-1}

6 Biotin-Streptavidin biosensing

6.1 Biotin-Streptavidin protocol as benchmark

Once the performances of the nanostructures were investigated, as described in the previous chapter, their efficiency as biosensors was tested by exploiting a largely studied target-ligand system, that is Biotin-Streptavidin. In this work, biotin (MW = 244 Da) will be used as a biorecognition element (or bioreceptor) to detect streptavidin (SA) (MW $\sim$ 53 kDa), which will be the target. Due to their structural properties, the biotin and the streptavidin have one of the highest affinities in nature amongst the non-covalent interactions, and thus they bind together very strongly and specifically [112, 113]. Thanks to their affinity, the biotin-SA system is the most commonly used for benchmark tests of plasmonic biosensors. Since biotin cannot bind directly to the gold surface, an additional ligand-layer was added in between. The protocol employed in this work for the immobilization of the biomolecules on the gold surfaces was developed by Van Duyne et al. [114]. The functionalization protocol consisted mainly in three steps: (1) a self assembled monolayer (SAM) of two kinds of thiols was bound to the gold surface: a inert spacer thiol and an active one; (2) biotin was bound to the latter by a crosslinking reaction; (3) the functionalized nanostructure was exposed to different concentrations of streptavidin. The response of the sensor was monitored by optical measurements after each functionalization step and thus the specificity and the sensitivity of the plasmonic biosensing platforms can be investigated. A schematic representation of the Biotin-SA functionalization protocol is depicted in figure 6.1.

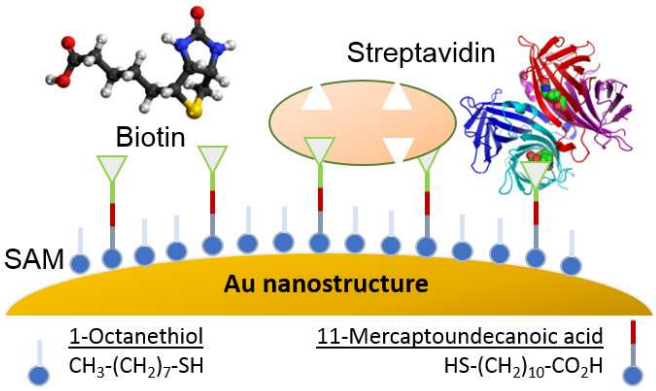

Figure 6.1: Schematic representation of the Biotin-Streptavidin functionalization protocol.

6.1.1 Thiols Self-Assembled Monolayer

The self assembled monolayer (SAM) of alkanethiols represents the most common strategy to bind biomolecules to gold surfaces. Alkanethiols, whose chemical formula is described by $HS-(CH_2)_n-X$, represents an organosulfur compound that has at the ends, respectively, an anchoring group (HS-) and a head group (-X). These molecules were widely

studied due to their spontaneously adsorption on gold surfaces that produces a strong bound between the sulfur and the gold atoms [115].

The strength of S-Au bound was deeply investigated by Xue et al. and the rupture force is reported to be $0.5 \div 1.0\,\mathrm{nN}$ [116], while the binding energy is $\sim 50\,\mathrm{kcal/mol}$ [117]. The hydrocarbon chain, of variable length, is bound at the opposite end with a terminal group that confers the specific physical and chemical properties on the alkanethiol.

In this work, alkanethiols with two different terminal groups were employed. On one side, the reactive thiol 11-Mercaptoundecanoic Acid (11-MUA) ($HS-(CH_2)_{10}-COOH$) was used to consecutively crosslink the carboxyl group with the bioreceptor. On the other side, a shorter inert thiol, 1-Octanethiol (1-OCT) ($HS-(CH_2)_7-CH_3$), was employed as a spacer and as a protection against aspecific adsorption. The latter was necessary to avoid the steric hindrance of the target protein and a 3:1 ratio of 11-MUA:1-OCT was suggested by Van Duyne's protocol [114]. Therefore, the SAM process consisted in incubating the plasmonic nanostructures in a solution of ethanol ($\geq 99.5\%$ absolute ethanol) with a 1 mM total concentration of thiols. Afterwards, samples were rinsed with ethanol and dried with N_2 flow.

6.1.2 Biotin

Biotin is a small vitamin (vitamin H) with a molecular weight (MW) of $244\,\mathrm{g/mol}$ which is present in all living cells. In order to bind biotin to the thiol SAM, an amine-derivatized biotin was used (Biotin-PEG_2-Amine from Thermo Scientific, MW = 374.5 Da). Thus, the amine group (-NH_2) allowed to covalently bind biotin to the 11-MUA by a crosslinking reaction between the -COOH group from the thiol and the -NH_2. The crosslinker agent that reacts with both functional groups thus creating the amine bond is the 1-Ethyl-3-[3-Dimethylaminopropyl]Carbodiimide hydrochloride (EDC) (from Sigma Aldrich), a catalyzer with MW = 191.7 g/mol [4]. The reaction scheme of EDC is described in figure 6.2.

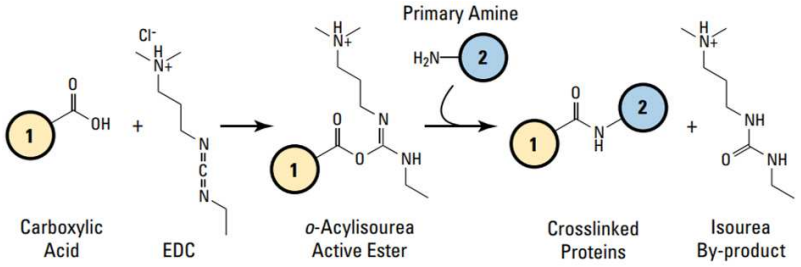

Figure 6.2: EDC crosslinking reaction scheme. In this case, molecule ① is the 11-MUA and molecule ② is the Amine-PEG_2-Biotin [4].

The buffer solution commonly employed for the crosslinking reaction is the 2-(N-Morpholino)EthaneSulfonic acid sodium salt (MES) solution with an acid pH of $4.5 \div 5$ [118]. Phosphate Buffered Saline (PBS) buffer with neutral pH, instead, was used by Van Duyne [114] but this is advisable only if the molecules to be bound are much less concentrated than the EDC.

For this reason, the MES buffer has been utilized to bind oligonucleotides to 11-MUA in the next chapter whereas PBS has been used for the experiments reported in this chapter.

The Phosphate Buffered Saline solution was prepared with one tablet of PBS (from Sigma Aldrich) diluted in 200 mL of Milli-Q water and thus a saline solution was obtained with 10 mM phosphate, 137 mM NaCl and pH 7.4.

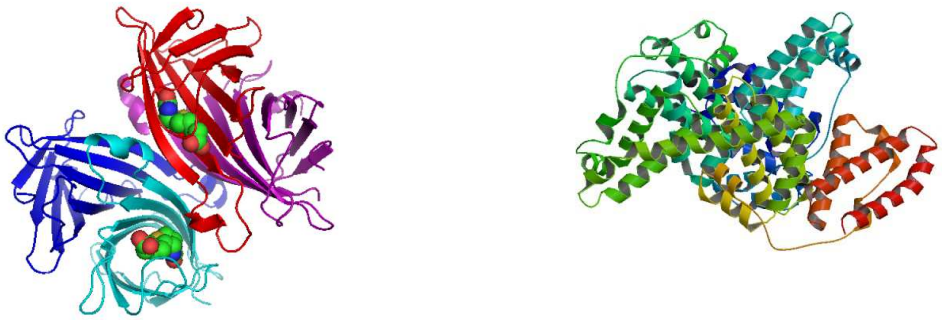

(a) Streptavidin **(b)** BSA

Figure 6.3: (a) Streptavidin protein, MW = 52.8 kDa. The four differently coloured ribbons correspond to the four identical subunits of the protein. (b) Bovine Serum Albumine protein, MW = 66.5 kDa.

The samples functionalized with the thiol layer were incubated for 2h in a PBS solution with 1mM of Biotin-PEG_2-Amine and 10mM EDC. Afterwards, the samples were rinsed first in PBS and then in Milli-Q water to remove the excess molecules and finally dried with N_2 flow.

6.1.3 Streptavidin

Streptavidin (SA) is a bacterial tetrameric protein with MW = 52.8 kDa extracted from the actinobacterium Streptomyces avidinii, with dimensions of $4.5 \times 4.5 \times 5.8\,\mathrm{nm}^3$ and a footprint area of $\sim 25\,\mathrm{nm}^2$ [119]. Since SA consists of four identical subunits, there are four equivalent binding sites able to interact with biotin with a very high affinity. Their affinity constant K_a in solution is $\sim 10^{13}\,\mathrm{M}^{-1}$ but K_a decreases when adsorption from the solution to a biotinylated surface is considered [112].

For the streptavidin binding, different parameters must be taken into account. The orientation of the bioreceptor, the steric hindrance of the target, non specific target-target or target-substrate interactions could all affect the specific and selective binding of SA to biotin. However, the optimal biotinylated layer was obtained, as described above, with the protocol of Van Duyne [114] where spacing between the biotin molecules and protection against aspecific adsoprtion of streptavidin on the gold layer were guaranteed by the 1-OCT.

The possibility of breaking the bound between biotin and SA was reported by Holmberg et al. [120] and it relies on treatments in water at elevated temperature that dissociate the two molecules without denaturing them. Thus, same biosensing platform could be used for consecutive expositions to the SA but this possibility was not exploited in this work.

In order to test the recognition of SA by the biotinylated gold nanostructures, the samples were incubated in a PBS solution with different concentrations of streptavidin ($10^{-13}\,\mathrm{M} \leq [\mathrm{SA}] \leq 10^{-5}$) for 2h to reach the binding equilibrium. Finally, samples were rinsed with PBS and Milli-Q water and then dried with N_2 flow.

The Bovine Serum Albumine (BSA), which is an ellipsoidal protein with dimensions of $4 \times 4 \times 14\,\mathrm{nm}^3$ and with molecular structure and weight similar to streptavidin (MW = 66.5 kDa) [121], was employed for selectivity tests by exposing the biotinylated samples to a $\sim 10^{-5}\,\mathrm{M}$ concentrated solution. In figure 6.3 the structures of SA and BSA are depicted.

Reagents Absolute Ethanol, 1-Octanethiol, 11-Mercaptoundecanoic acid, PBS tablets, EDC, Streptavidin and Bovine Serum Albumin were purchased from Sigma Aldrich, while Biotin-PEG_2-Amine was purchased from Thermo Scientific. All reagents were used without further purifcation. Table 6.1 summarizes the MW of the molecules that were utilized here.

11-MUA	1-OCT	Biotin-PEG_2-Amine	EDC	Streptavidin	BSA
218.36 Da	146.29 Da	374.5 Da	191.7 Da	52.8 kDa	66.5kDa

Table 6.1: MW of the molecules used in this for Biotin-Streptavidin biosensing test.

6.2 Samples for biosensing experiments

At each functionalization step of the plasmonic nanostructures, the optical spectra were acquired in order to monitor the position of the plasmonic resonance and thus the binding of molecules that leads to a change in the refractive index at the surface.

Small disuniformities in the nanoarray lead to small variations of the resonance position. Since the binding of biomolecules produces shifts of up to tenth of nanometers, it is necessary to assure the reproducibility of the measurements. More specifically, at each functionalization step the same area of the samples has to be interrogated in order to avoid false shift signals, which may occure due to the disuniformities. For this reason, and in order to take advantage of the wide nano-patterned areas that the colloidal lithograpy allows to produce (cf. figure 5.2), spots of nanoarrays were realized intead of large areas.

To do this, just before the final metal deposition, when the nanostructures were synthesized, a perforated phosphorous bronze foil with 2 mm diameter holes was put on to the substrate as showed in figure 6.4a. Therefore, 9 spots of nanostructures were obtained, as showed in figure 6.4b, and they were employed as independent biosensing platforms. The sample holders for, respectively, Jasco V670 Spectophotometer and Ocean Optics HR4000 are presented in figures 6.4c,d and permitted to center the beamlight on the spots with micrometric precision, thus ensuring the reproducibility of the optical measurements.

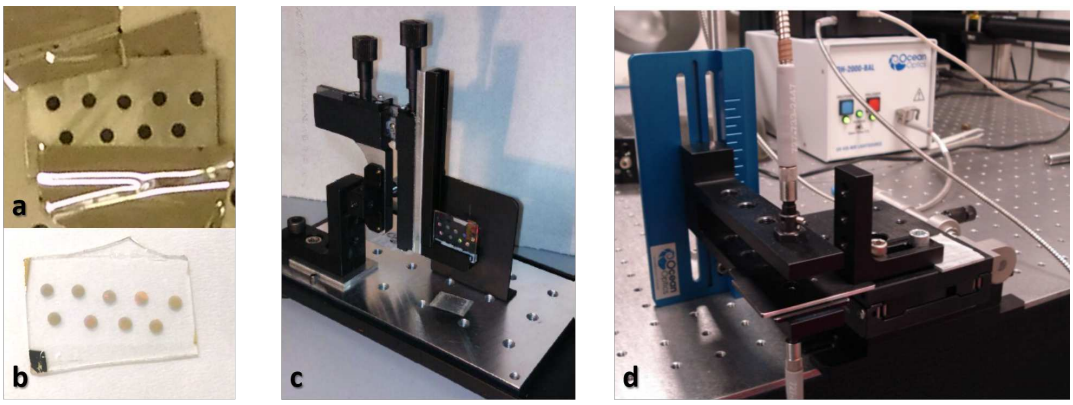

Figure 6.4: (a) A perforated phosphorous bronze foil is put on the substrates with the PS mask just before the final metal deposition. **(b)** 9 spots of with 2 mm diameter are obtained on one PS mask. **(c,d)** Sample holders, respectively, for Jasco V670 and Ocean Optics HR4000, which allow to center the incident beamlight on the spot with micrometric precision.

Thanks to the spot patterning of the substrates, each single spot of nanostructures could

be independently funtionalized by depositing droplets of 2.7 μL. The functionalization protocol is here briefly summarized:

1. a SAM of thiols was bound to the gold surfaces by immersing all the samples in a bath of ethanol with 1 mM concentration (1-OCT 3 : 1 11-MUA from Van Duyne's protocol). The samples were then rinsed with ethanol, dried with N_2 flow and then optical measurements were performed;

2. The crosslinking of biotin to 11-MUA was performed by depositing on the nanostructures' spots 2.7 μL droplets of a PBS solution with 1 mM Biotin-PEG_2-Amine and 10 mM EDC for 2h. The samples were rinsed with PBS and Milli-Q water, dried with N_2 flow and then optical spectra were acquired;

3. The biorecognition of streptavidin was performed by depositing on each nanostructures' spot 2.7 μL of PBS solution containing different concentrations of SA and thus incubating for 2h. Therefore, it was possible to deposit up to 9 different target solutions on the same sample. After rinsing in PBS and Milli-Q water and drying with N_2 flow, the optical spectrum of each spot was measured.

6.3 Extended Surface Plasmons (E-SP) based biosensors

6.3.1 Ordered NanoHole Array biosensing

The ordered NanoHole Array (o-NHA) nanostructure was firstly employed for the biosensing test with the Biotin-Streptavidin protocol described above. The o-NHA samples were synthesized as previously described in section 5.2.2 with the additional perforated foil to obtain the 2 mm diameter spots.

The samples were immersed in the thiol bath for 24h immediatly after the gold etchant cleaning, with a 1 mM thiols solution of 11-MUA:1-OCT 2:3. A single o-NHA spot exposed a total gold area of 3.08 mm^2 given by the sum of the surface on the top and inside the hole. Since the footprint of a single thiol is $\sim 0.214\,nm^2$, the total thiols bound in one spot was predicted to be $1.44 \cdot 10^{13}$ thiols/spot: $5.75 \cdot 10^{12}$ 11-MUA/spot and $8.63 \cdot 10^{12}$ 1-OCT/spot. The thiol SAM was achieved in 20 mL solution bath that gives $\sim 10^{19}$ thiols, which is clearly above the saturation computed for the gold surface.

Transmittance spectra were acquired with Jasco V670 and then the samples were functionalized with Biotin-PEG_2-Amine. A 2.7 μL droplet of 1 mM biotin solution was deposited on an o-NHA spot, and this, again, was above the saturation limit ($1.6 \cdot 10^{15}$ biotin molecules to bind with $6.3 \cdot 10^{12}$ 11-MUA molecules). Therefore, all the -COOH terminal groups were supposed to be bound to a Biotin-PEG_2-Amine bioreceptor.

Afterwards, from the stock solution of streptavidin ([SA]=$1.67 \cdot 10^{-5}$M), less concentrated solutions were prepared down to 10^{-11}M. Different spots were exposed to 2.7 μL droplets with different [SA] concentrations in order to achieve the sensing response as a function of the [SA]. As previously described, the output signal was computed by fitting the transmittance peaks with a Fano function from equation 5.5 and then evaluating the peak shift described by $\Delta\lambda_{EOT}$. Concentrations of $10^{-5} \div 10^{-6}$, that contained $10^{12} \div 10^{13}$ streptavidin molecules per droplet, are supposed to saturate all the biotin, if a 100% efficiency reaction and 1:1 biotin-streptavidin binding is supposed.

Figure 6.5 presents the transmittance spectra obtained after each functionalization step of a single spot: thiol self-assembling (red line), biotin crosslinking (blue line) and target exposure (yellow line). First, a shift of $\sim 3\,nm$ is observed after the exposure to biotin and this assures that the crosslinking reaction occured. Since the exposure to biotin was

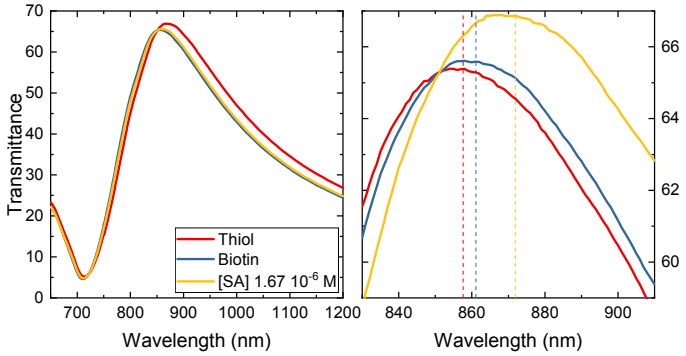

Figure 6.5: Transmittance spectra of an o-NHA spot after each functionalization step. Transmittance peaks are zoomed-in in the graph on the right panel and λ_{EOT} is indicated by vertical dashed lines: $\lambda_{EOT}^{thiol} = 858\,\text{nm}$, $\lambda_{EOT}^{biotin} = 861\,\text{nm}$, $\lambda_{EOT}^{SA} = 872\,\text{nm}$.

the same for all the spots in a sample, the average shift for the biotin binding step was calculated to be :

$$\text{BIOTIN:}\ \Delta\lambda_{EOT} = 3.3 \pm 0.6\,\text{nm}$$

In order to test the robustness of the functionalization layers and the stability of the o-NHA, after each functionalization step, multiple rinsings with Milli-Q water were performed and the λ_{EOT} was monitored. In figure 6.6 it can be observed that the washing steps did not yield a significant shift and this assesses the stability and reliability of both, the functionalization protocol and the o-NHA sample.

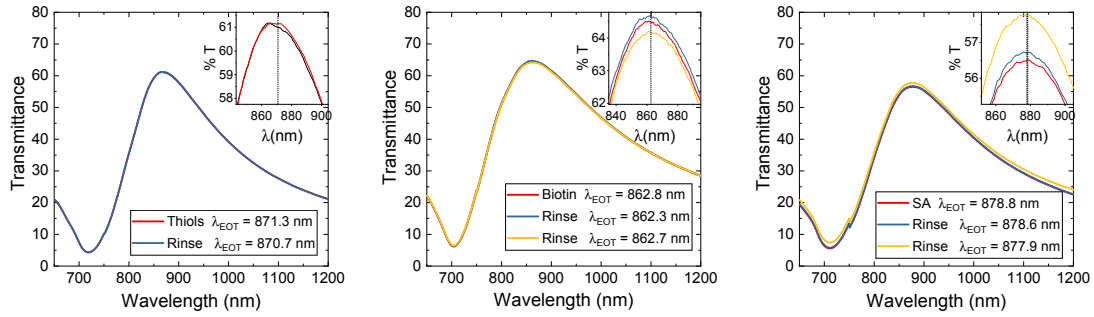

(a) Thiols **(b)** Biotin **(c)** Streptavidin

Figure 6.6: Transmittance spectra measured before and after multiple rinsings with Milli-Q water. No considerable shift was observed after the rinsings. The vertical shift in (c) is due to sample misalignment.

By monitoring the response $\Delta\lambda_{EOT}$ with exposure to different concentrations of SA, a sensing curve was obtained. This relates the extraordinary optical transmission (EOT) peak shifts to streptavidin concentration [SA] in a logaritmic scale and is depicted in figure 6.7; the corresponding data are reported in Table 6.2 . The response of the sensor was fitted with the Langmuir isotherm function from the Langmuir adsorption model [114]

$$\Delta\lambda_{EOT} = \frac{\Delta\lambda_{sat} \cdot K_a \cdot [\text{SA}]}{1 + K_a \cdot [\text{SA}]} \tag{6.1}$$

where $\Delta\lambda_{sat}$ represents the maximum output signal, that is, the maximum shift when saturation is reached, and K_a is the effective affinity constant between ligand and target.

The Langmuir fit yielded:

$$\text{LANGMUIR FIT o-NHA:} \quad \Delta\lambda_{sat} = (8.7 \pm 0.4)\,\text{nm} \quad K_a = (2.8 \pm 0.5) \cdot 10^6\,\text{M}^{-1}.$$

The $\Delta\lambda_{sat}$ is compatible with the shift produced by the addition of a dielectric layer of $\sim 5.5\,\text{nm}$ thickness and $n \sim 1.5$ on an o-NHA whose local sensitivity was previously computed in section 5.2.4.

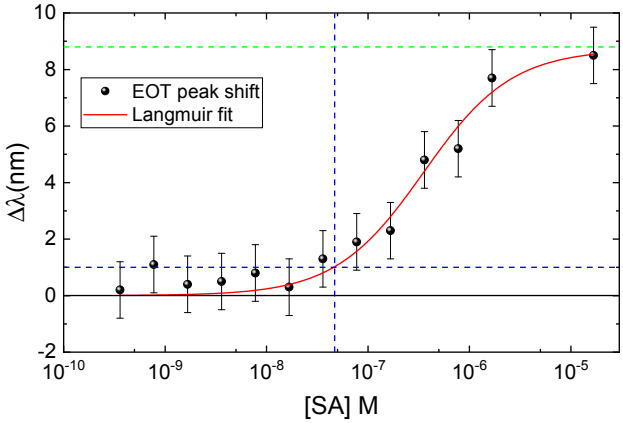

Figure 6.7: The Langmuir sensing curve. The horizontal dashed lines represent respectively the $y = \sigma_{\Delta\lambda}$ and the saturation levels while the vertical dashed line highlightes the position of the limit of detection.

[SA] (M)	SA	$\Delta\lambda_{\text{EOT}}$ (nm)	[SA] (M)	SA	$\Delta\lambda_{\text{EOT}}$ (nm)
$3.60 \cdot 10^{-10}$	$5.9 \cdot 10^{8}$	0.2	$7.75 \cdot 10^{-8}$	$1.3 \cdot 10^{11}$	1.9
$7.75 \cdot 10^{-10}$	$1.3 \cdot 10^{9}$	1.1	$1.67 \cdot 10^{-7}$	$2.7 \cdot 10^{11}$	2.3
$1.67 \cdot 10^{-9}$	$2.7 \cdot 10^{9}$	0.4	$3.60 \cdot 10^{-7}$	$5.9 \cdot 10^{11}$	4.8
$3.60 \cdot 10^{-9}$	$5.9 \cdot 10^{9}$	0.5	$7.75 \cdot 10^{-7}$	$1.3 \cdot 10^{12}$	5.2
$7.75 \cdot 10^{-9}$	$1.3 \cdot 10^{10}$	0.8	$1.67 \cdot 10^{-6}$	$2.7 \cdot 10^{12}$	7.7
$1.67 \cdot 10^{-8}$	$2.7 \cdot 10^{10}$	0.3	$1.67 \cdot 10^{-5}$	$2.7 \cdot 10^{13}$	8.5
$3.60 \cdot 10^{-8}$	$5.9 \cdot 10^{10}$	1.3			

Table 6.2: SA concentrations and the number of molecules in the functionalization droplet are reported with their corresponding peak shift. A $\sigma_{\Delta\lambda} = 1\,\text{nm}$ was considered for each shift.

From the fitted sensing curve, the limit of detection (LoD) can be computed. This represents the lowest analyte concentration that the o-NHA sensor can detect, and it can be computed as the intersection between the the Langmuir isotherm curve and $y = \sigma_{\Delta\lambda}$, where $\sigma_{\Delta\lambda}$ is the error bar given to the shift measurements. From figure 6.7, where $\sigma_{\Delta\lambda} = 1\,\text{nm}$, LoD is computed to be:

$$\text{LoD}_{o-NHA} = (4.8 \pm 0.3) \cdot 10^{-8}\,\text{M}$$

Specificity test In addition to the LoD, another fundamental characteristic of a biosensor is the specificity. This was tested by measuring a blank signal and an aspecific one. For the blank signal, a spot was exposed to the PBS solution, thus with [SA]=0. Figure 6.8a presents the spectra before and after the exposure to PBS and a $\Delta\lambda \sim 0.4\,\text{nm}$ was measured, which is null within the experimental errors (1 nm). This, on one side, further

confirmed the stability of the already bound molecules, and, on the other side, assured that no PBS buffer was deposited on the surface of the o-NHA.

The specificity was also tested by exposing the biotinylated o-NHA to a high concentration of BSA protein and the spectra, before and after, are presented in figure 6.8b. No shift was expected but a $\Delta\lambda \sim 3\,\text{nm}$ was obtained instead. Since no specific binding can occur between BSA and biotin, the aspecific signal might be due to BSA binding with the glass surface at the hole bottom.

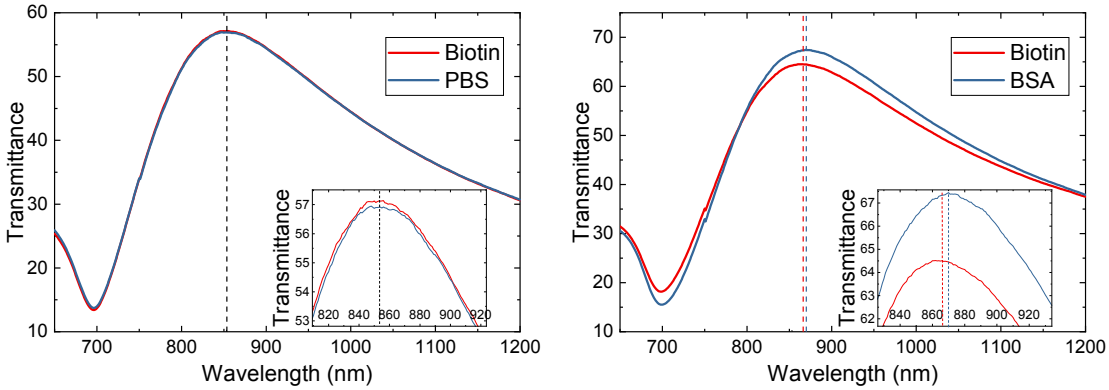

(a) Exposure to PBS **(b)** Exposure to BSA

Figure 6.8: Specificity is tested by measuring a blank signal with PBS ([SA]=0) and an aspecific signal by exposing the sample to BSA protein. No significant shift ($< 1\,\text{nm}$) was observed for PBS exposure whereas a $\Delta\lambda \sim 3.0\,\text{nm}$ signal is obtained for BSA.

6.3.2 Disordered NanoHole Array biosensing

The same protocol has been exploited to functionalize the disordered NanoHole Array (d-NHA) samples. Their synthesis and sensing performances were described in detail in section 5.3. By considering the standard disordered NanoHole Array (d-NHA) sample, which has a surface coverage of holes of ~ 0.21 - 290 nm diameter and 70 nm gold layer - the total gold surface exposed in a single spot was computed to be $\sim 3.19\,\text{mm}^2$, very similar the one estimated for the o-NHA. Thus, all the assumptions regarding the surface functionalization and saturation are still valid.

The d-NHA samples were first immersed for 24h in 2:3 11-MUA:1-OCT thiol solution, then Biotin-PEG_2-Amine was crosslinked to the surface. Finally, the biosensing response of an o-NHA was compared directly to the one of a similar, but disordered, sample by exposing a d-NHA to different concentrations of streptavidin.

The transmittance peaks were measured with Jasco V670 and the peak positions were monitored by fitting the data with the Fano function. Figure 6.9a presents the signal output of the d-NHA-based sensor for a saturation concentration of SA ([SA]=$1.67 \cdot 10^{-6}$ M). Transmittance spectra are measured before and after the exposure to SA and are depicted in figure by, respectively, the red and blue curves, and a satuation shift of $\Delta\lambda = 5.8\,\text{nm}$ is calculated. Figure 6.9b shows, instead, $\Delta\lambda$ as a function of the SA concentration and the Langmuir isotherm fit of the sensing curve; the corresponding data are reported in table 6.3. The following parameters were found for the Langmuir function from equation 6.1:

$$\text{Langmuir fit d-NHA:}\quad \Delta\lambda_{sat} = (6.0 \pm 0.9)\,\text{nm} \quad K_a = (1.8 \pm 1.0) \cdot 10^6\,\text{M}^{-1}.$$

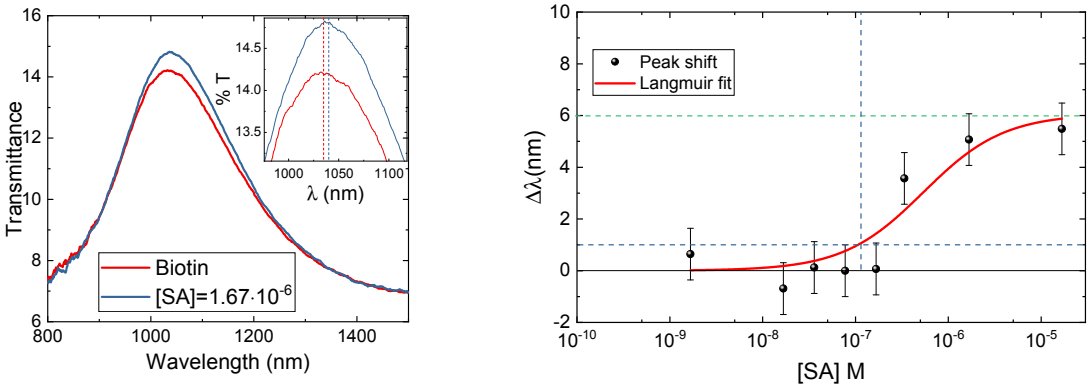

(a) Exposure to $[\mathrm{SA}] = 1.67 \cdot 10^{-6}$ M

(b) Sensing curve

Figure 6.9: (a) Optical transmittance spectra, before (red curve) and after (blue curve) exposure to a saturation concentration of SA ($[\mathrm{SA}]$=$1.67 \cdot 10^{-6}$ M), of a d-NHA; the peak shift results $\Delta\lambda = 5.8\,\mathrm{nm}$. **(b)** Sensing curve fitted with the Langmuir isotherm. The horizontal dashed lines represent respectively $y = \sigma_{\Delta\lambda}$ and the saturation level whereas the vertical line indicates the LoD.

[SA] (M)	**SA**	$\boldsymbol{\Delta\lambda_{EOT}}$ (nm)	**[SA] (M)**	**SA**	$\boldsymbol{\Delta\lambda_{EOT}}$ (nm)
$1.67 \cdot 10^{-9}$	$2.7 \cdot 10^{9}$	0.6	$1.67 \cdot 10^{-7}$	$2.7 \cdot 10^{11}$	0.1
$1.67 \cdot 10^{-8}$	$2.7 \cdot 10^{10}$	−0.7	$3.60 \cdot 10^{-7}$	$5.9 \cdot 10^{11}$	3.5
$3.60 \cdot 10^{-8}$	$5.9 \cdot 10^{10}$	0.1	$1.67 \cdot 10^{-6}$	$2.7 \cdot 10^{12}$	5.0
$7.75 \cdot 10^{-8}$	$1.3 \cdot 10^{11}$	−0.1	$1.67 \cdot 10^{-5}$	$2.7 \cdot 10^{13}$	5.8

Table 6.3: d-NHA response as a function of the SA concentration and the number of molecules in the functionalization droplet.

Finally, the LoD for the d-NHA was computed to be almost three-fold with respect to the one of o-NHA:

$$\mathrm{LoD}_{d-NHA} = (1.3 \pm 0.4) \cdot 10^{-7}\,\mathrm{M}.$$

6.3.3 Discussion

In chapter 5, the local sensitivities for the ordered and disordered NanoHole Arrays (o-NHA, d-NHA) were computed to be:

$$S_0^{\text{o-NHA}} \simeq 2.7\,\mathrm{RIU}^{-1} \qquad S_0^{\text{d-NHA}} \simeq 1.8\,\mathrm{RIU}^{-1}.$$

When the NanoHole Array (NHA) samples are exposed to the highest SA concentration and thus the gold surface is saturated, a SA layer of $\sim 5.5\,\mathrm{nm}$ thickness [122] with $n \sim 1.5$ refractive index is added conformally on the surface. Therefore, the expected saturation shift can be computed from:

$$\Delta\lambda_{sat} = S_0 \cdot \Delta n \cdot h.$$

Here, $\Delta n = 0.5$ is the refractive index variation with respect to the air, yielded by the binding of organic compounds to the surface, and $h \sim 5.5\,\mathrm{nm}$ represents the streptavidin thickness. Therefore the expected saturation shifts are, respectively:

$$\Delta\lambda_{sat,\text{d-NHA}}^{expected} \simeq 5.5 \pm 1\,\mathrm{nm} \qquad \Delta\lambda_{sat,\text{o-NHA}}^{expected} \simeq 7.5 \pm 1\,\mathrm{nm}.$$

These values resulted slightly lower than the $\Delta\lambda_{sat}$ actually obtained from the Langmuir fit and from the exposure to the highest SA concentration, but still comparable within the experimental errors. This could be due to an underestimation of the local sensitivities. When incremental silica layers were deposited for the local sensitivity investigation, the layer that was deposited on the gold surface inside the hole could have been a little thinner than the one that was measured on the top surface, due to the geometry of the deposition technique. Therefore, a thinner layer of silica on the internal gold surface, with respect to the expected one, might have leaded to a slight underestimation of the experimental local sensitivity. If the simulated local sensitivity for o-NHA $S_0 \simeq 3.1\,\mathrm{RIU}^{-1}$, where perfectly uniform silica layers were added all over the gold surface, is considered instead of the experimental one, an expected saturation shift of 8.5 nm is obtained, and this matches perfectly with the measured one.

For low concentrations, instead, both sensing curves are characterized by shift fluctuations. By considering the exposed gold surface ($\sim 3.1\,\mathrm{mm}^2$) and the footprint of SA ($\sim 25\,\mathrm{nm}^2$) the saturation number of SA molecules was computed to be $\sim 1.25 \cdot 10^{11}$, which corresponds to a concentration of $[SA] \simeq 7.7 \cdot 10^{-8}\,\mathrm{M}$. Therefore, a saturation signal should be observed by exposing a sample to droplets with concentrations down to $7.7 \cdot 10^{-8}\,\mathrm{M}$. Table 6.2 shows, instead, that the signal drops from the saturation shift for concentrations of the order of $10^{-7}\,\mathrm{M}$, where saturation was is still expected. This early drop of the shift signal suggests that not all the streptavidin molecules were delivered to the gold surface, and this is likely due to a non optimal control of the exposure of the NHA samples to the target molecules triggered by hydrophobicity issues. Indeed, when a droplet of target solution is deposited on the spot, it tends to spread also on the glass substrate around the spot, thus leading to a loss of analyte. This was due to the higher hydrophobicity of the o-NHA and d-NHA with respect to the surrounding substrate [123] and to the natural inclination of proteins to stick to the glass surface. Moreover, the hydrophobicity of the NHA may prevent the target solution from reaching the bottom rim of the hole, where the sensitivity to refractive index variations is higher due to the localization of the electric field. For these reasons, when low concentrations of target molecules are employed, analyte may not be efficiently delivered to the gold surface thus leading to the fluctuations observed in both sensing curves (cf. figures 6.7 and 6.9b).

In order to confine the functionalization droplets within the NHA spot and to avoid the aspecific binding of proteins to the glass substrate around the spot and inside the nanoholes an initial protection step might be added to the functionalization protocol. On one side Polyethylene Glycol (PEG) might be deposited on the substrate in order to prevent aspecific adsorption and increase the hydrophobicity [124, 125]. The substrate must be firstly activated by oxydizing it in a reactive plasma and then silane-terminated PEG molecules could be bound to the active glass surface. On the other side, another widely used strategy is to expose the samples to the BSA protein that was used for the specificity test. Since BSA binds strongly both to hydrophobic and hydrophilic surfaces, samples could be exposed after the biotin functionalization step to 1% solution of BSA. This would limit further aspecific bindings by blocking all the potential binding sites that lead to aspecific signals (i.e., glass, free amine groups) [126, 127]. This strategy was employed for the protection of the NanoPrisms Array (NPA) whose biosensing results will be reported in the following section.

Despite the sensing issues discussed above, it is clear from the experiments described above that E-SP based biosensors could be used to detect biomolecules. Moreover, due to the higher local sensitivity proved in the previous chapter, the ordered NanoHole Arrays resulted more suitable for biosensing applications with a limit of detection three times

smaller than the one of disordered NanoHole Arrays.

6.4 NanoPrisms Array based biosensor

In this section the biosensing results achieved with the Localized Surface Plasmon Resonance (LSPR)-based NanoPrisms Array (NPA) biosensors will be presented. The synthesis and the sensing performances were described in detail in Section 5.1. As for the ordered and disordered NHA, a perforated phosphorous bronze foil has been used during the metal evaporation to obtain spots of nanostructures with 2 mm diameter.

In order to estimate the gold area exposed by a NPA spot, the total surface of a single nanoprism was firstly computed by the analysis of AFM images and resulted to be $A_{prism} \simeq 0.019\,\mu\text{m}^2$. Since a spot includes about $2.66 \cdot 10^7$ nanoprisms, the total gold area per spot was $0.505\,\text{mm}^2$ which is 6 times smaller than the one exposed by the ordered and disordered NHA. This assured that the assumptions for the saturation concentrations of thiols and biotin were still valid. The NPA samples were functionalized, as above, at first in a 24h bath of thiols and then incubated with Biotin-PEG_2-Amine. In this case, a 1:3 11-MUA:1-OCT ratio has been employed for the thiol bath, as suggested by Van Duyne [114].

In order to prevent the target solution from binding to the substrate surrounding the nanoprisms and the spot, the protection strategy based on the exposure to a blocking agent, the BSA protein, has been employed. In detail, the biotinylated NPA samples were incubated for 1h in a bath with 1% solution of BSA in PBS buffer (1%BSA = 1 mg/mL = $1.5 \cdot 10^{-5}$ M) [85]. After rinsing with PBS and Milli-Q water and drying with N_2 flux, the samples were exposed to different concentrations of SA ($10^{-11}\,\text{M} \leq [\text{SA}] \leq 10^{-5}\,\text{M}$).

Absorbance spectra were acquired after each functionalization step with the Ocean Optics HR4000 spectrometer and the position of the LSPR peaks has been determined by fitting with the Lorentzian function.

Figure 6.10 presents the absorbance spectra of a NPA sample at the different functionalization steps before the exposure to the target solution: SAM of thiols (red line), Biotin-PEG_2-Amine (blue line) and BSA protection layer (orange line). The crosslinking of biotin to the gold surface produced a $\simeq 4.4\,\text{nm}$ shift while the exposure to the BSA protein gave a $\sim 10\,\text{nm}$ signal. The BSA signal arises from the sticking of the protein to the glass surface in proximity to the nanoprism edges. Here, the localized electric field outside the nanoprism offers a high sensitivity to refractive index variations thus revealing the sticking of BSA protein to the surrounding glass. Since these functionalization steps were common to all the NPA spots, the average corresponding shifts were computed to be:

$$\text{Biotin: } \Delta\lambda_{LSPR} = 4.1 \pm 0.4\,\text{nm} \qquad \text{BSA: } \Delta\lambda_{LSPR} = 10.0 \pm 0.9\,\text{nm}$$

Once the NPA spots were exposed to the blocking agent, they were incubated with different concentrations of the target solution and the signal output was evaluated by measuring the absorbance spectra. Figure 6.11 shows the absorbance spectra before and after incubation with two different SA solutions: a saturation concentration [SA]= $1.67 \cdot 10^{-6}$ M, which gave a $\Delta\lambda_{LSPR} = 17.8\,\text{nm}$, and [SA]= $7.90 \cdot 10^{-11}$ M, which gave null signal.

Table 6.4 lists the signal output as a function of the concentration of the target solution and of the amount of target molecules in the $2.7\,\mu$L solution droplets used for the incubation. The sensing curve was drawn in figure 6.12 and it was fitted with the Langmuir isotherm function from eq. 6.1. The following parameters were obtained:

$$\text{Langmuir fit NPA: } \Delta\lambda_{sat} = (18.3 \pm 0.3)\,\text{nm} \quad K_a = (1.26 \pm 0.07) \cdot 10^7\,\text{M}^{-1}.$$

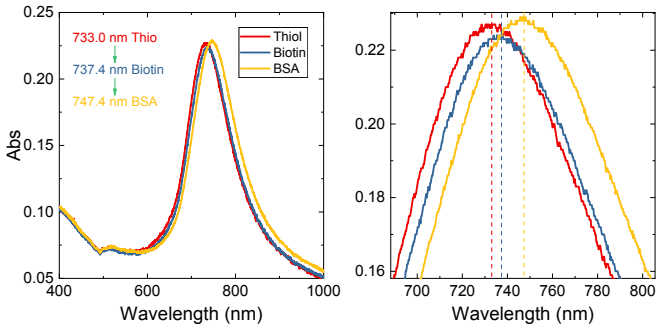

Figure 6.10: Left panel: Absorbance spectra of a spot measured after the different functionalization step. Right panel: Magnification of the absorbance maxima. The vertical dahed lines mark the spectral position of the maxima at each step: thiol (red line) $\lambda_{LSPR} = 733.0\,\text{nm}$; biotin (blue line) $\lambda_{LSPR} = 737.4\,\text{nm}$; BSA (orange line) $\lambda_{LSPR} = 747.4\,\text{nm}$.

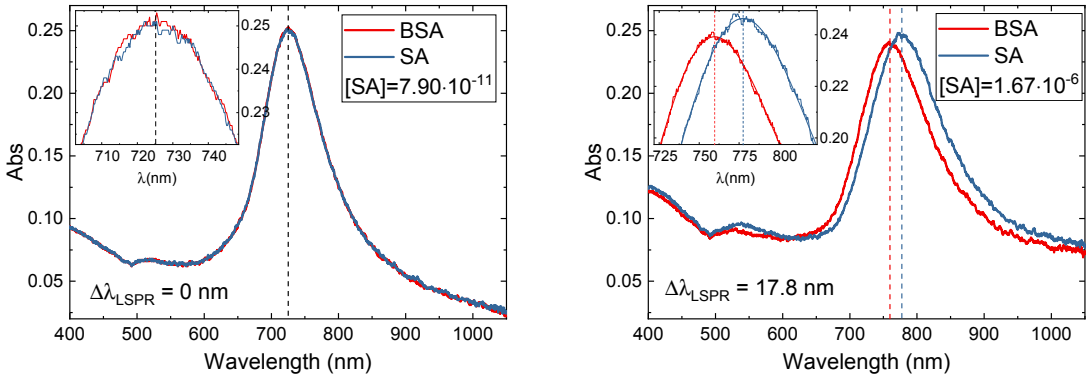

(a) **(b)**

Figure 6.11: The absorbance spectra of two spots before and after the incubation with SA solutions: (left) NPA spot was exposed to $[\text{SA}] = 7.90 \cdot 10^{-11}\,\text{M}$ and gave a 0 nm signal; (right) NPA spot was incubated with a saturation concentration of $[\text{SA}] = 1.67 \cdot 10^{-6}\,\text{M}$ and gave $\Delta\lambda_{LSPR} = 17.8\,\text{nm}$.

From the sensing curve in figure 6.12 the limit of detection for the NPA-based biosensors was computed by considering $\sigma_{\Delta\lambda} = 1\,\text{nm}$:

$$\text{LoD}_{\text{NPA}} = (4.4 \pm 0.2) \cdot 10^{-9}\,\text{M}.$$

This value is ten times smaller than the one computed for the o-NHA, thus proving the better biosensing performances of the NPA, as anticipated by the higher local sensitivity described in the previous chapter.

Specificity test A specificity test has been performed by incubating the NPA spots with a blank solution with no SA molecules (PBS buffer) and with an aspecific protein solution (BSA).

The spectra before and after exposure to the PBS buffer are reported in figure 6.13a. A very small blueshift of $-0.8\,\text{nm}$ was observed, which is compatible with 0 within the experimental errors ($\sim 1\,\text{nm}$). Figure 6.13b shows, instead, the absorbance spectra before

[SA] (M)	SA	$\Delta\lambda_{EOT}$ (nm)	[SA] (M)	SA	$\Delta\lambda_{EOT}$ (nm)
$7.90 \cdot 10^{-11}$	$1.3 \cdot 10^{8}$	0.0	$2.34 \cdot 10^{-8}$	$3.8 \cdot 10^{10}$	4.0
$1.61 \cdot 10^{-10}$	$2.6 \cdot 10^{8}$	−0.1	$4.77 \cdot 10^{-8}$	$7.8 \cdot 10^{10}$	6.8
$3.28 \cdot 10^{-10}$	$5.3 \cdot 10^{8}$	−0.3	$9.71 \cdot 10^{-8}$	$1.6 \cdot 10^{11}$	10.7
$6.68 \cdot 10^{-10}$	$1.1 \cdot 10^{9}$	−0.3	$1.92 \cdot 10^{-7}$	$3.1 \cdot 10^{11}$	12.8
$1.36 \cdot 10^{-9}$	$2.2 \cdot 10^{9}$	0.0	$4.03 \cdot 10^{-7}$	$6.6 \cdot 10^{11}$	14.5
$2.77 \cdot 10^{-9}$	$4.5 \cdot 10^{9}$	0.5	$8.20 \cdot 10^{-7}$	$1.3 \cdot 10^{12}$	17.0
$5.64 \cdot 10^{-9}$	$9.2 \cdot 10^{9}$	1.3	$1.67 \cdot 10^{-6}$	$2.7 \cdot 10^{12}$	17.8
$1.15 \cdot 10^{-8}$	$1.9 \cdot 10^{10}$	2.2	$1.67 \cdot 10^{-5}$	$2.7 \cdot 10^{13}$	18.0

Table 6.4: The NPA response is listed as a function of the SA concentration and the number of molecules in the functionalization droplet. An experimental error of $\sigma_{\Delta\lambda} = 1\,\text{nm}$ was considered for each shift.

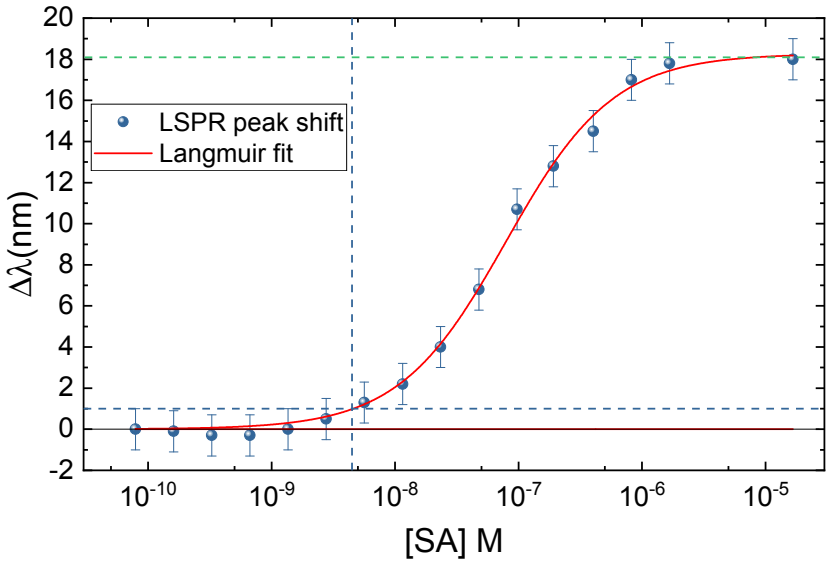

Figure 6.12: Sensing curve for the NPA. The horizontal dashed lines represent respectively the $y = \sigma_{\Delta\lambda}$ and the saturation levels. The vertical dashed line indicates the LoD.

and after the additional exposure to 1% BSA. A small redshift of 2.5 nm was observed that represents $\sim 14\%$ of the saturation signal $\Delta\lambda_{sat}$. By remembering the results for the o-NHA - $\Delta\lambda_{sat} = 8.7\,\text{nm}$ and $\Delta\lambda_{BSA} = 3.0\,\text{nm}$, which represented $\sim 35\%$ of $\Delta\lambda_{sat}$ - it is clear that the protection with the first BSA exposure reduced the ratio of the aspecific signal to the saturation one. Therefore, the BSA signal obtained for the NPA samples was still a small effect of the aspecific interaction, in agreement with the results obtained with BSA exposure in similar samples by Van Duyne's group [114].

Discussion In Chapter 5, the local sensitivity of the NPAs was computed to be $S_0^{\text{NPA}} = 8.8 \pm 0.4\,\text{RIU}^{-1}$ and thus an expected $\Delta\lambda_{sat}$ was computed by considering the adsorbed layer of streptavidin at saturation as a dielectric layer with $n = 1.5$ and thickness $t \simeq 5.5\,\text{nm}$:

$$\Delta\lambda_{sat}^{expected} \simeq 24.2 \pm 1.1\,\text{nm}.$$

The expected saturation shift is greater than the experimental one obtained with the highest SA concentration ($\Delta\lambda_{sat} \simeq 18.0 \pm 1.0\,\text{nm}$). This might be attributed to the first

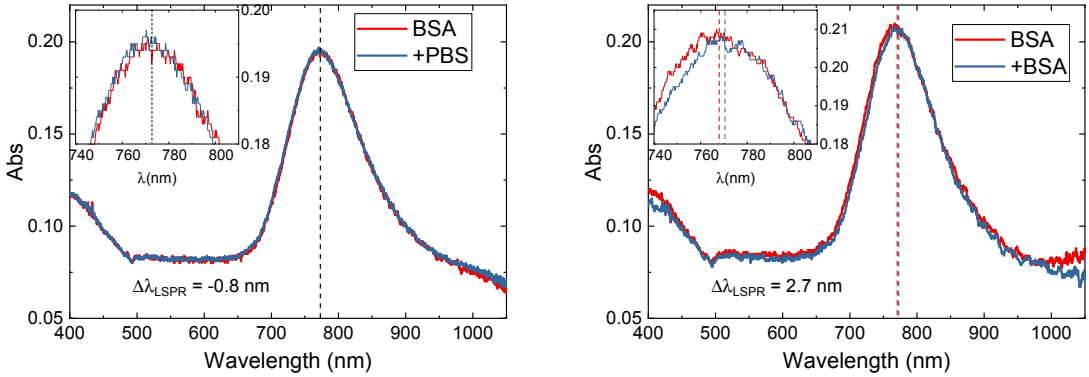

(a) PBS exposure **(b)** BSA exposure

Figure 6.13: Optical absorbance spectra of a NPA sample protected with BSA before and after expoure to (a) PBS and (b) to a BSA solution (1%). The blank signal obtained with exposure to PBS was negligible ($\sim -0.8\,\text{nm}$) while with the BSA solution a further aspecific signal of $\sim 2.5\,\text{nm}$ was obtained.

BSA exposure, where a large shift was observed. In fact, the 10 nm signal could have been produced not only by BSA sticking on the glass near the nanoprisms but, could be also due to aspecific adsorption of BSA on the biotinylated gold surface, thus blocking part of the biotin binding sites for the SA. However, this did not prevent from obtaining a clear specific signal and thus a sensing curve, suggesting that only a small part of the binding sites might have been blocked by BSA.

6.5 Conclusions

In this chapter biosensing tests were performed by employing three different plasmonic nanostructures: ordered NanoHole Arrays, disordered NanoHole Arrays and NanoPrisms Arrays. The results of the corresponding biosensing experiments are summarized in table 6.5.

	$\Delta\lambda_{sat}$ (nm)	$\Delta\lambda_{blank}$ (nm)	LoD (nM)	K_a (M^{-1})
o-NHA	8.7 ± 0.4	0.4	48 ± 3	$(2.8 \pm 0.5) \cdot 10^6$
d-NHA	6.0 ± 0.9	-	130 ± 50	$(1.8 \pm 1) \cdot 10^6$
NPA	18.3 ± 0.3	-0.8	4.4 ± 0.2	$(1.26 \pm 0.07) \cdot 10^7$

Table 6.5: Summary of the biosensing performances obtained with o-NHAs, d-NHAs and NPAs.

The limit of detection obtained for the o-NHA samples is comparable with those reported in the literature, for o-NHAs with similar lattice constant and diameter. Im ad co-workers [128] obtained a LoD of 30 nM by employing Focused Ion Beam (FIB) synthesized samples with squared lattice and 420 nm period in the intensity interrogation method for the detection of streptavidin. The 48 nM LoD obtained here with Nanosphere Lithography (NSL) synthesized o-NHA proved that the cost-effective technique represents a valid alternative for developing plasmonic biosensors. Also the LoD of NPA, which is at the state of the

art for such kind of biosensors, confirms the feasibility of synthesizing biosensing platforms with the NSL technique.

The d-NHA systems, which were synthesized by another cost-effective technique - the Sparse Colloidal Lithography (SCL) - resulted the less efficient amongst the three nanostructures demonstrating, again, that an ordered nanohole pattern enhances the plasmonic and biosensing performances with respect to a disordered one. The other nanostructure produced by SCL, that is the NanoDisk Array (NDA), has not been employed for the biosensing test. However, from the sensitivity performances reported in the previous chapter NDA is expected to be competitive with the NPA.

The affinity constants obtained from the Langmuir fit are much smaller than the value of $K_a = 10^{13}\,\mathrm{M}^{-1}$ expected for biotin-streptavidin binding in solution. On one side, K_a decreases when adsorption on a surface is considered. On the other side, the Langmuir adsorption model itself relies on the assumption that the adsorbing sites are located on a perfectly flat surface. This assumption is not fullfiled neither for the nanohole arrays nor for the nanoprism arrays and the Langmuir isotherm fit might produce an underestimation of K_a.

In order to further increase the biosensing performances of the nanostructures, the protection against biofouling could be improved. NPA samples pre-exposed to BSA gave a further signal after a second exposure and this suggested that a better protection was needed.
On one side, the aspecific binding to the biotinylated gold surface could be reduced by improving the PEGylation of the surfaces by replacing the PEG_2 in the Amine-PEG_2-Biotin molecule with a larger one, i.e., PEG_{11}, thus providing a more efficient anti-fouling effect. On the other side, the inert areas of the nanostructured samples, i.e., the glass substrate around the nanostructures or inside the nanoholes, could be better protected by a specific PEGylation functionalization with large Methoxy-PEG_n-Silane (m-PEG) molecules.

7 MicroRNA detection

The microRNA (miRNA) is a small single-stranded non-coding RNA molecule that is present both in animals and in plants and consists of $21 \div 23$ nucleotides [129]. Although miRNAs are non-coding, which means that they are not transcripted into a protein, they play an important role for the stability and the transcription of RNA [129]. More specifically miRNAs can control the gene expression and play a major role in different biological processes such as cell proliferation, differentiation and development. In the latest years, the presence of specifical miRNAs in blood has been related to different diseases and cancers [130]. Therefore, the detection of small miRNA concentrations in blood would lead to an early-diagnosis for specific diseases, like tumors, and thus to an early treatment.

In this chapter, the best-performing nanostructures were tested for the detection of a specific miRNA, the miR27a (target), which consists of 21 bases. First, the nanostructures were functionalized properly in order to bind the bioreceptor (probe), that is the complementary oligonucleotide, to the gold surface. Then, hybridization was performed by incubating the nanostructures with a target miRNA solution.

7.1 Protocol for miR-27a

The protocol employed for the miRNA experiments was adapted from the work of Biscontin et al. [131] thanks to a collaboration with their group at the Biology Department of the University of Padova. In order to conjugate the bioreceptor with the gold surface, the probe oligonucleotide has to be modified with proper reactive organic functional groups. Linkage groups such as primary amines or thiols can be incorporated within the oligonucleotide, at the 5' or 3' end, thus allowing the specific binding to different surfaces. In addition to the linkage groups, fluorescent dyes could also be linked to the other end of the probe oligonucleotide. No linkage group, instead, is necessary for the target oligonucleotide, since it hybridizes with the probe oligo and hydrogen bonds are created between the complementary nitrogenous bases (A-T and C-G). Both probe and target oligonucleotides could also be modified with standard fluorescent dyes, Cy3 or Cy5, that let to check the bindings by fluorescence measurements. The corresponding maximum excitation and emission wavelengths for both dyes are reported in table 7.1.

In this work, modified probe and target oligonucleotides were purchased from IDT Integrated DNA Technologies and a detailed list is reported in table 7.2. The oligonucleotides pellets were diluted in Milli-Q water to a stock concentration of $100\,\mu$M and stored at $-20°$C.

The sequence of the single-stranded DNA (ssDNA) consists of 21 nucleotides with a molecular weight of 6455.3 Da. The maximum length of a single nucleotide in the ssDNA configuration is ~ 1 nm so the total lenght of the bioreceptor molecule was about 20 nm. However, after the hybridization, the double helix is formed and the length approximately halves.

Dye	λ_{ex}	λ_{em}	MW (Da)
Cy3	550 nm	570 nm	767
Cy5	650 nm	670 nm	792

Table 7.1: Maximum excitation (λ_{exc}) and emission (λ_{em}) wavelengths and molecular weights of Cy3 and Cy5 dyes.

Name	5'-Sequence-3'	5'/3' mod.	MW (Da)
HS-C_6-(miR-27a Probe)	GCG GAA CTT AGC CAC TGT GAA	HS-C_6/-	6783.7
HS-C_6-(miR-27a Probe)-Cy3	GCG GAA CTT AGC CAC TGT GAA	HS-C_6/Cy3	7428.3
NH_2-C_{12}-(miR-27a Probe)	GCG GAA CTT AGC CAC TGT GAA	NH_2-C_{12}/-	6718.6
NH_2-C_{12}-(miR-27a Probe)-Cy5	GCG GAA CTT AGC CAC TGT GAA	NH_2-C_{12}/Cy5	7389.2
miR-27a Target	TTC ACA GTG GCT AAG TTC CGC	-/-	6397.2
miR-27a Target-Cy3	TTC ACA GTG GCT AAG TTC CGC	-/Cy3	7041.8

Table 7.2: Single stranded DNA oligonucleotides purchased from IDT with the corrisponding modifications at 3' and 5' ends. NH_2 and HS represent, respectively, the amine and the thiol linkage groups.

7.1.1 Probe and target miRNA functionalization

The probe oligo can be linked to the gold sufrace in two different ways: by crosslinking reactions between previously bound 11-MUA and the amine-modified oligo or by self-assembling of the thiol-modified oligo directly on the gold surface.

Amine-modified probe The linking protocol for the amine-modified probe was adapted from the work of Biscontin et al. [131]. The first step represented the deposition of a SAM of a 1:3 11-MUA:1-OCT thiols and this step was largely described in section 6.1.1. Once the freshly thiolated nanostructures were obtained, the crosslinking reaction was performed as follows:

- the probe solution was prepared with 4 μM of NH_2-C_{12}-(miR-27a probe) and 0.5 μg/mL of fresh EDC in a 0.1 M MES buffer;
- the sample was incubated for 30 minutes in a bath of the probe solution;
- the rinsing was performed by dipping consecutively in 0.1M MES, 0.02X TWEEN, 0.1X SDS and Milli-Q water;
- finally, the sample was dried in a centrifuge.

Thiol-modified probe The thiol-modified oligonucleotides could be directly self-assembled on the gold surface and the protocol was adapted from the work of Joshi [80]. The freshly synthesized nanostructured samples were immersed for 24 h in a 1:1 PBS 1X solution with 4 μM HS-C_6-(miR-27a probe) and 4 μM 1-OCT as a spacer. Finally, the samples were rinsed with Milli-Q water to clean the excess molecules and dried with a centrifuge.

Target hybridization Once the probe oligonucleotides were bound to the surface of the nanostructures, the samples were exposed to the target oligo solution. This was prepared

in a Saline Sodium Citrate (SSC) 3X buffer with 2 μM of miRNA from the stock solution. A gasket glass slide was used to incubate the functionalized nanostructures with the target for 16 h at 37°C in a hybridization oven.

After incubation, the samples were rinsed in buffer solutions with decreasing concentration (SSC 3X, SSC 1X and SSC 0.5X) since the direct exposure to Milli-Q water would lead to the dissociation of the two oligonucleotides.

The affinity constant K_a of the binding between two complementar nucleotides is $K_a \approx 3 \cdot 10^4\,\mathrm{M}^{-1}$. Therefore, for the interaction between the 21 nucleotides long target and probe it resulted $K_a \approx 6.3 \cdot 10^5\,\mathrm{M}^{-1}$, which was much smaller than the value $K_a \approx 10^{13}\,\mathrm{M}^{-1}$ reported for the biotin-streptavidin complex.

7.2 NPA biosensor for miR-27a

7.2.1 Probe binding

The spotted samples of NPAs were synthesized as described in the previous chapter, treated with gold etchant (cf. section 5.1.3) and immersed, immediately after, in a 1:3 11-MUA:1-OCT thiol solution in ethanol for 24h (cf. section 6.1.1). Then, the crosslinking protocol was employed to bind the probe oligonucleotide to the thiolated NPA sample. All the oligonucleotide functionalizations were done inside gasket slides for hybridization chambers from Agilent (cf. figure 7.1a). Since all the 9 spots were contained in one chamber, the total exposed gold surface was $9 \times 0.505 \approx 4.5\,\mathrm{mm}^2$ and thus the total 11-MUA thiols were $5.3 \cdot 10^{12}$ (total thiols $\sim 2.12 \cdot 10^{13}$). A 170 μL droplet of the 4 μM probe solution was dropped in the chamber in order to cover all the spots. This amount of probe solution contained $\sim 4.1 \cdot 10^{14}$ probe oligonucleotides and was enough to saturate all the 11-MUA thiols. After the 30 minutes crosslinking reaction and the rinsing steps, absorbance spectra were measured with the Ocean Optics HR4000 spectrometer.

Figure 7.1b presents the absorbance spectrum before the crosslinking reaction, after the probe binding and after an additional rinsing in Milli-Q water. A redshift is observed after the probe binding and this confirmed that the crosslinking reaction was successful. Moreover, since no further shift occured after the second rinse in Milli-Q water, this demonstrated the stability of the bound probe oligos. The average redshift for the probe binding was obtained by taking into account all the NPA spots and it was computed to be:

$$\Delta\lambda_{LSPR}^{probe} = 13.7 \pm 1.2\,\mathrm{nm}$$

The binding of the probe was also checked by functionalizing a NPA sample with the dyed probe, NH_2-C_{12}-(miR-27a probe)-Cy5 instead of NH_2-C_{12}-(miR-27a probe). Thus, fluorescence measurements were performed to confirm the binding of the dyed probe. Fluorescence spectra of the sample were acquired with Fluoromax spectrofluorometer (Horiba) and figure 7.2a points out that the dyed probe crosslinked successfully with the NPA, whereas no signal was observed when the surrounding glass was investigated. The specific binding of the probe on the NPA sample was also confirmed by the fluorescence microscopy picture in figure 7.2b and it can be observed that the fluorescence signal occured only within the spot boundaries.

7.2.2 Target hybridization

Finally, the hybridization was performed in a chamber with 170 μL, with 2 μM of target miRNA in SSC 3X. After rinsing in SSC 3X, SSC 1X and SSC 0.5X, the sample was

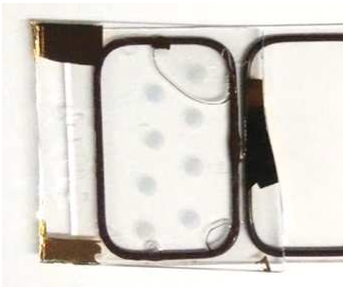

(a) Incubation chamber

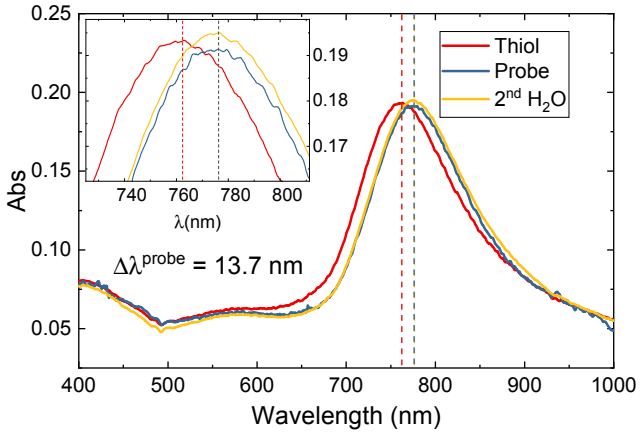

(b) Probe crosslinking

Figure 7.1: **(a)** The chamber employed for all the oligonucleotides functionalizations. **(b)** Absorbance spectra before and after the crosslinking reaction are reported. The inset is a close-up view of the LSPR peak: the vertical dashed lines show the redshift of the peak at each step. A subsequent Milli-Q water rinsing yielded no shift thus proving the stability of the sample: $\lambda_{thiols} = 762.4\,\text{nm}$, $\lambda_{probe} = 776.2\,\text{nm}$, $\lambda_{rinse} = 776.4\,\text{nm}$.

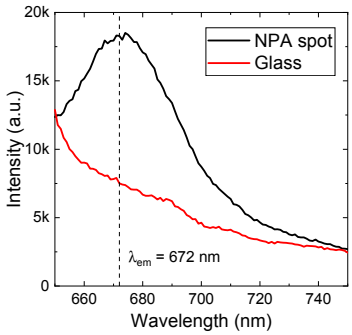

(a)

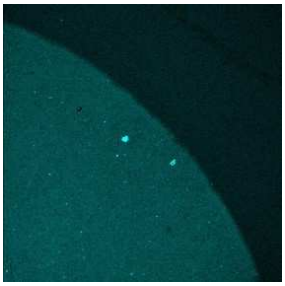

(b)

Figure 7.2: **(a)** Fluorescence spectra measured with Fluoromax spectrofluorometer. **(b)** Fluorescence microscope image of a spot and the surrounding glass.

centrifuged and the absorbance spectra were measured. Two similar samples, produced together in the same thermal evaporation process and functionalized with the probe oligo, were processed simultaneously: one was incubate with the target solution whereas the other was exposed to the SSC 3X buffer in order to perform a blank hybridization. For these experiments, the oligonucleotides with the fluorescent dyes were employed.

In figure 7.3a the measurements for the target hybridization are reported. A redshift of $\sim 14\,\text{nm}$ was observed for the crosslinking step whereas a large blueshift of $\sim -32\,\text{nm}$ was obtained after the hybridization process. The spectra for the blank hybridization with SSC 3X buffer are shown in figure 7.3b. A similar peak shift of $\sim 12\,\text{nm}$ was obtained after the probe binding while a larger blueshift was observed after the blank hybridization: $\sim -48\,\text{nm}$. By taking into account the response from different spots of NPA, the average shifts for the two hybridizations were computed to be:

$$\text{TARGET: } \Delta\lambda_{LSPR} = -32 \pm 2\,\text{nm} \qquad \text{BLANK(SSC 3X): } \Delta\lambda_{LSPR} = -50 \pm 3\,\text{nm}$$

In order to check the presence of the oligonucleotides, fluorescence measurements were

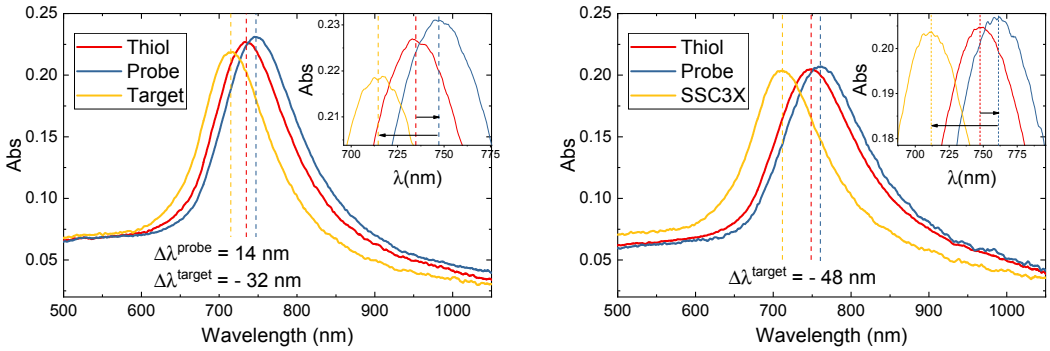

(a) Target hybridization **(b)** Blank hybr. w/ SSC 3X

Figure 7.3: **(a)** Target hybridization: thiolated sample (red), probe crosslinking (blue) and target hybridization (yellow). A redshift of $\sim 14\,\text{nm}$ was observed after the binding of the probe oligo whereas a large blueshift of $\sim -32\,\text{nm}$ was measured, instead, after the hybridization. **(b)** Blank hybridization in SSC 3X: thiolated sample (red), probe (blue) and SSC 3X (yellow) exposure. A similar shift of $\sim 12\,\text{nm}$ was obtained for the probe binding whereas a $-48\,\text{nm}$ blueshift was found for the blank hybridization.

performed and are reported in figure 7.4. Figure 7.4a presents the fluorescence spectra of Cy5 before and after the target exposure and evidences that the probe oligo was stable during the hybridization process. Figure 7.4b reports the fluorescence spectra of the samples that were exposed to, respectively, target and buffer solution for the hybridization. The Cy3 signal was observed only for the sample exposed to the target oligo and this confirmed that the hybridization between probe and target oligos was successful. Finally, figure 7.4c shows the fluorescence spectra of the two samples after thoroughly rinsing with Milli-Q water. The absence of Cy3 signal suggested that the rinsing in ultrapure water leaded to the dissociation of the double-stranded DNA, thus removing the target oligo and its fluorescent dye.

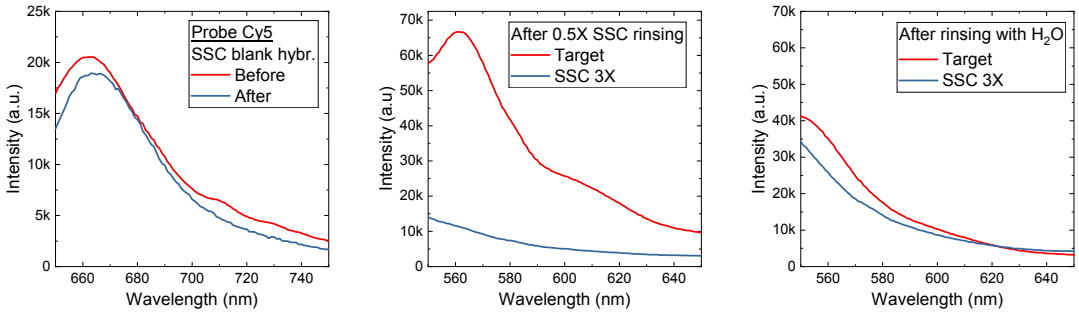

(a) Probe **(b)** Target **(c)** H_2O rinse

Figure 7.4: **(a)** Fluorescence spectra of the Cy5 dye, which confirmed the presence of the probe before and after the hybridization process. **(b)** Fluorescence spectra of the samples exposed to blank and target solution. The presence of the signal of the Cy3 dye confirmed the hybridization between probe and target. **(c)** Fluorescence spectra of the same samples after thoroughly rinsing with Milli-Q water. No Cy3 signal was detected.

In order to compare the response of the NPA samples with another plasmonic nanostructure, a NHA went through the same functionalization protocol: thiol SAM, crosslinking

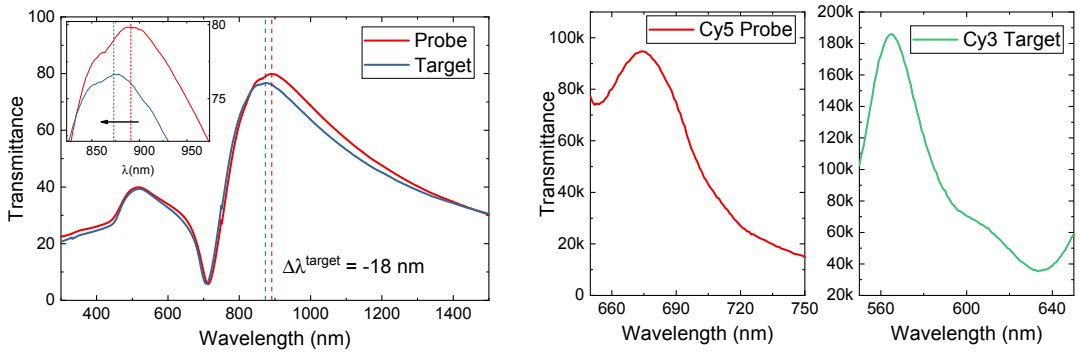

(a) Target exposure **(b)** Fluorescence spectra of Cy5 and Cy3

Figure 7.5: (a) Transmittance spectra of a NHA sample before and after the hybridization process. A blueshift was confirmed as for the NPA.**(b)** Fluorescence spectra of the Cy5 (probe) and Cy3 (target), confirming that both crosslinking and hybridization were successful.

reaction for the probe and finally hybridization with target solution. From the transmittance spectra in figure 7.5a, it can be observed that also in the case of the NHA sample a blueshift was obtained after the hybridization process ($\Delta\lambda_{EOT}^{target} \sim -18\,\text{nm}$). Nevertheless, both probe and target were detected by fluorescence measurements, as shown in figure 7.5b.

On one side, the binding of the probe oligo was confirmed both by the redshift of the absorbance spectra of the samples and by the fluorescence measurements of the samples where probe with Cy5 was employed. On the other side the hybridization process leaded to large blueshifts but the presence of the Cy3 signal suggested that binding of the target to the probe oligonucleotide occurerd.

The blank hybridization of the NPA sample leaded to a blueshift of $-50\,\text{nm}$ and this was probably due to the removal of the nanosatellites around the nanoprism caused by the high concentration saline solution, as previously described in section 5.1.3. Therefore the $-32\,\text{nm}$ shift obtained for the sample that went through the target hybridization could be interpretated as the the combination of the action of SSC 3X ($\sim -50\,\text{nm}$) and the double-stranded DNA formation ($\sim +18\,\text{nm}$). In order to avoid the large blueshifts, two ways were pursued to improve the functionalization protocol, as described in the followig sections: on one side, the samples went through a SSC 3X pre-treatment and on the other side the protocol from Joshi [80] was employed.

7.3 Protocol improvements

7.3.1 NPA pre-treatment in SSC 3X

The first way to improve the functionalization protocol was to perform a physical cleaning pre-treatment instead of using the gold etchant (cf. section 5.1.3). Therefore, the freshly synthesized NPA samples were incubated with SSC 3X solution for 24h at 40° C in a hybridization oven. As reported in section 5.1.3, this treatment removed the nanosatellites around the nanostructures, yielding a sharper resonance and it also stabilised the NPA samples for the further treatments. After the SSC 3X treatment, the sample went through the standard protocol for the miR-27a functionalization: SAM of thiols, crosslinking of the probe and then target hybridization.

In figure 7.6a the absorbance spectra of a NPA spot after each functionalization step

are reported. The probe crosslinking yielded a redshift of $\sim 13.9\,\text{nm}$, thus confirming the binding of the bioreceptor. This was compatible with the shift observed previously for the probe functionalization. The average redshift for crosslinking reaction was then evaluated to be:

$$\text{PROBE: } \Delta\lambda_{LSPR} = 13 \pm 1\,\text{nm}$$

The hybridization step, instead, produced a large redshift of the LSPR peak, as shown in figure 7.6a; the average redshift was computed to be:

$$\text{TARGET: } \Delta\lambda_{LSPR} = 33 \pm 3\,\text{nm}.$$

Since the target oligo has a similar molecular weight as the probe, the shift after the hybridization process was expected to be similar to the one yielded by the probe linking. Therefore, the larger shift obtained might be due to residual salt deposited on the NPA after the hybridization and the centrifuge drying. This might have yielded a $\Delta\lambda_{LSPR}$ contribution that adds to the redshift caused by the target hybridization.

A sample exposed to the target oligonucleotide was then rinsed in Milli-Q water twice and the absorbance spectra are reported in figure 7.7. The sample was first dipped for 10 seconds in Milli-Q water: the LSPR peak blueshifted of $-21\,\text{nm}$ but it still has a 10 nm redshift with respect to the probe peak. The sample was then immersed for 1 minute in Milli-Q water and a further $-4\,\text{nm}$ blueshift was observed, thus showing a net 6 nm redshift with respect to the probe position. Since a couple of seconds of rinsing with Milli-Q water are enough for dissolving the residual salt, it is clear that the remaining 10 nm redshift was due to the binding of the target oligo. This value is comparable with the redshift for the probe binding. However, the double-stranded DNA molecule tends to dissociate when immersed in a very low salt concentration buffer and this justifies the further blueshift after the second and longer exposure to Millli-Q water.

In order to avoid any fouling signal due to the salt residuals from the buffer, the rinsing protocol should be improved or a less concentrated buffer could be used for the hybridization. In the next section an alternative protocol which employes PBS 1X will be presented.

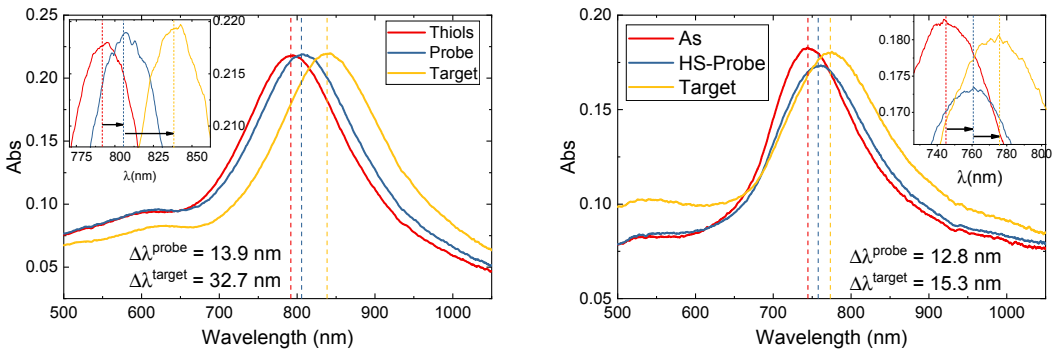

(a) SSC pre-treatment **(b)** HS-probe

Figure 7.6: (a) Functionalization after SSC 3X pre-treatment: thiols (red), probe (blue) and target (yellow). At each functionalization step a redshift was observed. **(b)** Functionalization with thiolated probe: as (red), HS-probe (blue) and harget hybridization (yellow). Redshifts were observed at each functionalization step.

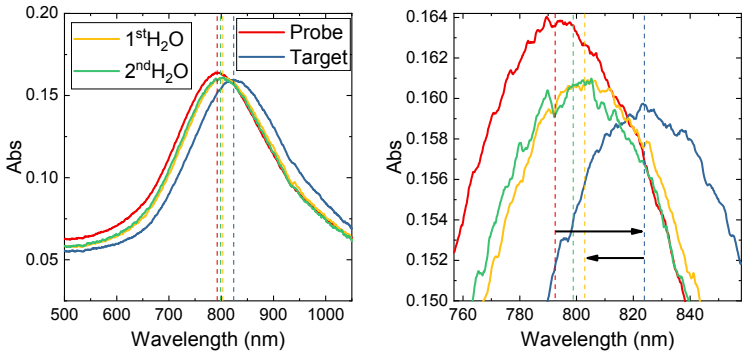

Figure 7.7: Absorbance spectra after water rinsings of the NPA samples exposed to target oligonucleotide: probe $\lambda_{LSPR} = 792\,\text{nm}$ (red), target $\lambda_{LSPR} = 824\,\text{nm}$ (blue), first water dipping $\lambda_{LSPR} = 803\,\text{nm}$ (yellow) and second water rinsing $\lambda_{LSPR} = 799\,\text{nm}$ (green).

7.3.2 Thiolated probe and PBS hybridization

The thiolated probe offered an alternative way for linking the oligonucleotides to the gold surface. Thanks to the sulfur group, the probe could bind to the gold surface and create a self-assembled monolayer as reported in the work of Joshi [80]. Therefore, freshly synthesized and cleaned NPA samples were incubated for 24h in a hybridization chamber with 170 μL PBS 1X thiol solution: 1:1 4 μM of HS-miR-27a and 4 μM of 1-OCT. After rinsing with H_2O, the absorbance spectra were acquired and, finally, the hybridization was performed by incubating the samples in a 2 μM target solution for 16h in the oven. The sample was then rinsed in PBS 1X and PBS 0.5X, centrifuged and then measured.

Figure 7.6b reports the absorbance spectra at each functionalization step. A $\sim 12.8\,\text{nm}$ redshift was observed for the self-assembling of the probe and this confirmes that the thiolated oligonucleotide successfully bind to the gold surface. The average shift was computed, and it resulted compatible with the one obtained with the amine crosslinking protocol (section 7.3.1). Indeed, the same shift was expected since the variation of the molecular weight due to the different terminal groups was very small (cf. table 7.2).

$$\text{Probe:}\ \Delta\lambda_{LSPR} = 12 \pm 2\,\text{nm}$$

A redshift of $\sim 15\,\text{nm}$ was obtained, instead, after the exposure to the target solution thus confirming that the hybridization of the double-stranded DNA occured (fig. 7.6b). The average redshift obtained for the target step was computed to be:

$$\text{Target:}\ \Delta\lambda_{LSPR} = 15 \pm 1\,\text{nm}$$

As expected, this shift was comparable with the one due to the probe oligo binding and it confirmes that the 33 nm redshift obtained by hybridization in SSC 3X was due to a combination of target binding signal and salt residuals.

7.4 Conclusions

In this chapter two different protocols were employed to bind probe oligonucleotides to the gold surface of NPA samples. On one side the amine terminated oligo reacted with the previously bound SAM of 11-MUA thiols. On the other side, thiol terminated oligos were directly bound to the gold surface. Since the terminal modifications of the oligonucleotide

sequence had a small molecular weight with respect to the single-stranded DNA sequence itself, similar redshifts of the absorbance peaks were reported for the two different protocols. Water rinsings and fluorescence measurements confirmed also the binding and the stability of the probe bioreceptors. The weighted average was computed and thus the redshift obtained after binding the probe ssDNA was:

$$\text{Probe ssDNA}: \quad \Delta\lambda_{LSPR} = 13 \pm 1\,\text{nm}$$

The hybridization step, which consisted in the specific binding between complementary single-stranded DNA sequences, resulted more challenging. A saline buffer was needed in order to allow the formation of the hydrogen bonds between complementary nitrogenous bases and the two protocols employed two different buffers, 3X Saline Sodium Citrate and 1X Phosphate Buffered Saline.

A large blueshift was obtained after the hybridization in 3X SSC buffer of a NPA that was cleaned with a gold etchant solution. To avoid this, a blank hybridization with SSC 3X buffer was performed as a pre-treatment for the NPA samples instead of using the gold etchant (cf. section 5.1.3). Positive shifts were then observed by exposing a NPA sample to the target solution. However, the 33 nm shift was much larger than the expected one and this might be due to the saline residuals deposited on the NPA sample during the 16h hybridization process with the target oligo in the SSC 3X buffer. Rinsing with Milli-Q water would dissolve and remove the residual salt, but an excessive exposure to ultrapure water leads also to the dissociation of the double-stranded DNA.

The PBS 1X buffer, which has a smaller salt concentration ($[\text{NaCl}]_{PBS1X} = 137\,\text{mM}$, $[\text{NaCl}]_{SSC3X} = 450\,\text{mM}$), was employed as a hybridization buffer and no residual salt was evident after the rinsing in PBS 1X and PBS 0.5X, and the centrifuge drying. Therefore, a redshift comparable with the one of the probe oligonucleotide was measured thus suggesting that hybridization was successful even with the thiol terminated oligonucleotides.

When exposed to solutions with low cation concentration the dissociation constant of the double-stranded DNA increases and the target oligo detaches from the probe in order to reach a new equilibrium. The percentage of bound target at a specific temperature (in this case room temperature, 25° C) is highly dependend on the salt concentration [132]. The computed hybridized fraction for the PBS 1X and SSC 3X was $\sim 94\%$ and it starts to considerably decrease when Na^+ concentration drops below $\sim 10\,\text{mM}$.

In conclusion, the NPA samples were stabilized for the mir-27a and successfully functionalised with the probe oligo. The shift signals described above suggested also that the hybridization process between probe and target oligonucleotides was successful. However, the hybridization protocol should be improved with particular attention to the rinsing steps. In order to better point out the shift due to the double-stranded DNA formation, the residual salt artifacts should be eliminated. To this aim, proper dilutions of the saline buffers should be investigated in order reach a compromise between removing salt residuals without dissociating the target-probe complex.

Nevertheless, it has been demonstrated that the NPA samples are suitable for oligonucleotides detection since a large shift of the LSPR peak was observed for the binding of the probe and the target molecules. Once the proper rinsing protocol is achieved, the NPA samples could be hybridized with target solution below the saturation level in order to investigate the response of the biosensor as a function of the target concentration and thus determine the limit of detection, which for microRNA is expected to be in the picomolar range [80].

Conclusions

In this work four kinds of nanostructures have been studied in detail: ordered NanoHole Arrays (o-NHA), disordered NanoHole Arrays (d-NHA), NanoPrisms Arrays (NPA) and NanoDisk Arrays (NDA). Their optical properties and sensing performances were investigated by numerical computation and by experimental measurements.

From numerical simulations, the NPA resulted the best-performing nanostructure in therms of local sensitivity, which is the fundamental property that determines the biosensing performances. This is due to the nanoprism's sharp vertices, where the highest electric field enhancement occurs, thus leading to a high sensitivity to dielectric function variations. The expected local sensitivity for the NPA was $S_0^{NPA} = 13.6 \pm 0.5\,\mathrm{RIU}^{-1}$ whereas for the NDA and o-NHA we obtained, respectively, $S_0^{NDA} = 11.8 \pm 0.4\,\mathrm{RIU}^{-1}$ and $S_0^{o-NHA} = 3.1 \pm 0.1\,\mathrm{RIU}^{-1}$.

The possibility of realizing these nanostructures in a cost-effective way and with a high-throughput technique has been also proved. It has been shown that both Nanosphere Lithography and Sparse Colloidal Lithography represent powerful and reliable techiques to produce, respectively, ordered and disordered nanostructures by exploiting the self-assembled monolayers of uncharged and charged polystyrene nanospheres as deposition masks. It has been proved also that such techniques allowed to finely control the morphology of the nanostructures and thus the plasmonic properties, by varying different fabrication parameters.

Once the standard samples were nanofabricated, their performances as transducers for dielectric variations were investigated by evaluating their experimental local sensitivities and these were found to be slightly smaller than the simulated ones. These small differences were acribed to imperfections of the synthesized samples with respect to the designed ones. However, NPA still yielded the highest sensitivity $S_0^{NPA} = 8.8 \pm 0.4\,\mathrm{RIU}^{-1}$ but NDA resulted to have a comparable sensitivity, $S_0^{NDA} = 7.8 \pm 0.2\,\mathrm{RIU}^{-1}$. Much lower sensitivities were obtained for the nanohole arrays, $S_0^{o-NHA} = 2.7 \pm 0.2\,\mathrm{RIU}^{-1}$ and $S_0^{d-NHA} = 1.8 \pm 0.1\,\mathrm{RIU}^{-1}$. This shows that LSPR-based biosensors result more suitable for very small dielectric variations at the interface and their good performances are due to the short-decay distance of the localized electric field.

The biotin-streptavidin complex has been exploited for biosensing tests with the plasmonic nanostructures. The ability to reveal the binding events between biotin, as receptor, and streptavidin, as analyte, using solutions with different concentrations of streptavidin, has been investigated. By monitoring the spectral shifts at different analyte concentrations, the sensing curves of the output signal as a function of the concentration were computed. Three out of the four nanostructures were tested and the following limit of detections were obtained: $\mathrm{LoD_{NPA}} = 4.4 \pm 0.2$ nM, $\mathrm{LoD_{o-NHA}} = 48 \pm 3$ nM, $\mathrm{LoD_{d-NHA}} = 125 \pm 40$ nM. Concerning the o-NHA and the d-NHA, the sensing curves presented shift fluctuations at low concentrations and these were imputed to the lack of an anti-fouling protection and to hydrophobicity issues that caused a not efficient delivery of the target molecules to the gold surface. The data fluctuations yielded large errors in fitting the sensing curve with the Langmuir model and thus in evaluating the limit of detection. A blocking agent, the BSA, has been adsorbed on the NPA samples to avoid the aspecific bindings. Therefore, smoother results were obtained with NPA and the BSA protection reduced the aspecific

signal from 37% to 14% of the saturation signal. However, this suggested that a better protection could be further achieved.

In order to reach a lower limit of detection, other protection schemes could be invetigated. On one side a protection layer could be specifically adsorbed on the glass substrate by silanization with mPEG-Silane molecules instead of the BSA passivation. On the other side, larger PEG molecules in the Amine-PEG_2-Biotin bioreceptor could be employed in order to improve the protection of the gold surface and thus reduce the anti-fouling effect.

The best performing plasmonic nanostructure (i.e., the NPA) has been employed also for the detection of a specific miRNA molecule, the miR-27a. The miRNA molecules are a non-coding oligonucleotides that represent biomarkers for specific diseases; complementary single stranded oligonucleotides were used, respectively, as probe and target. First, a pretreatment of the NPA samples in a saline solution (SSC 3X) has been performed in order to stabilize the nanostructures for the further functionalization steps. Subsequently, the probe oligo has been successfully bound to the gold surfaces with two different linking groups, amine and thiol. The binding of the probe yielded an average redshift of $\Delta\lambda_{probe} = 13 \pm 1$ nm and it was also confirmed by fluorescence measurements. Finally the hybridization with a $2\,\mu$M target solution has been carried out and the formation of the double stranded DNA molecule has been confirmed by the fluorescence measurements. A shift similar to the probe one has been reported but an improvement of the rinsing protocol after hybridization in the highly saline solution is needed in order to avoid artifacts due to the residual salt and to better resolve the spectral shift caused by the specific binding.

Nevertheless, it has been demonstrated that the NPA samples are suitable for oligonucleotides detection. Due to their similar local sensitivity, also NDA could be exploited for the miRNA detection. Once the hybridization protocol is improved, LoD in picomolar range is expected to be reached with NDA and NPA samples. The nanohole array samples, instead, due to their larger decay length, could be exploited for the detection of larger analytes such as viruses or bacteria.

Bibliography

[1] P.B. Johnson and R.W. Christy. Optical constants of the noble metals. *Phys. Rev. B*, 6(12):4370–4379, 1972. (Cited on pages xv, 8, and 9).

[2] T. W. Ebbesen, H. J. Lezec, H. F. Ghaemi, T. Thio, and P. A. Wolff. *Nature*, 391(6668):667–669, feb 1998. (Cited on pages xv, 2, 18, and 20).

[3] J.N. Anker, W.P. Hall, O. Lyandres, N.C. Shah, J. Zhao, and R.P. Van Duyne. Biosensing with plasmonic nanosensors. *Nature materials*, 7(6):442–453, 2008. (Cited on pages xv, 18, 23, and 28).

[4] *Thermo Scientific Crosslinkers Technical Handbook*. Thermo Fisher Scientific Inc, 2009. (Cited on pages xix and 86).

[5] Min Gu, Qiming Zhang, and Simone Lamon. Nanomaterials for optical data storage. *Nature Reviews Materials*, 1(12), oct 2016. (Cited on page 1).

[6] Surbhi Lal, Stephan Link, and Naomi J. Halas. Nano-optics from sensing to waveguiding. *Nature Photonics*, 1(11):641–648, nov 2007. (Cited on page 1).

[7] Sarah Unser, Ian Bruzas, Jie He, and Laura Sagle. Localized surface plasmon resonance biosensing: Current challenges and approaches. *Sensors*, 15(7):15684–15716, jul 2015. (Cited on page 1).

[8] Pranveer Singh. SPR biosensors: Historical perspectives and current challenges. *Sensors and Actuators B: Chemical*, 229:110–130, jun 2016. (Cited on pages 1 and 2).

[9] J M Pitarke, V M Silkin, E V Chulkov, and P M Echenique. Theory of surface plasmons and surface-plasmon polaritons. *Reports on Progress in Physics*, 70(1):1, 2007. (Cited on page 1).

[10] Gerardo A. Lopez, M.-Carmen Estevez, Maria Soler, and Laura M. Lechuga. Recent advances in nanoplasmonic biosensors: applications and lab-on-a-chip integration. *Nanophotonics*, 6(1):123–136, aug 2016. (Cited on page 2).

[11] Abhijit Biswas, Ilker S. Bayer, Alexandru S. Biris, Tao Wang, Enkeleda Dervishi, and Franz Faupel. Advances in top–down and bottom–up surface nanofabrication: Techniques, applications & future prospects. *Advances in Colloid and Interface Science*, 170(1-2):2–27, jan 2012. (Cited on page 2).

[12] Nicolas Vogel, Markus Retsch, Charles-André Fustin, Aranzazu del Campo, and Ulrich Jonas. Advances in colloidal assembly: The design of structure and hierarchy in two and three dimensions. *Chemical Reviews*, 115(13):6265–6311, jun 2015. (Cited on page 2).

[13] John C. Hulteen. Nanosphere lithography: A materials general fabrication process for periodic particle array surfaces. *Journal of Vacuum Science & Technology A: Vacuum, Surfaces, and Films*, 13(3):1553, may 1995. (Cited on pages 2 and 32).

[14] C. L. Haynes and R. P. Van Duyne. Nanosphere lithography: A versatile nanofabrication tool for studies of Size-Dependent nanoparticle optics. *The Journal of Physical Chemistry B*, 105(24):5599–5611, June 2001. (Cited on pages 2, 32, and 33).

[15] Thomas H. Reilly, Robert C. Tenent, Teresa M. Barnes, Kathy L. Rowlen, and Jao van de Lagemaat. Controlling the optical properties of plasmonic disordered nanohole silver films. *ACS Nano*, 4(2):615–624, 2010. PMID: 20112934. (Cited on pages 2, 21, 41, 42, 60, and 78).

[16] H. Fredriksson, Y. Alaverdyan, A. Dmitriev, C. Langhammer, D.?S. Sutherland, M. Zäch, and B. Kasemo. Holemask colloidal lithography. *Advanced Materials*, 19(23):4297–4302. (Cited on pages 2, 43, and 80).

[17] Stefan A. Mayer. *Plasmonics: Fundamentals and Applications*. Springer, 2007. (Cited on page 5).

[18] T. Kashiwa and I. Fukai. A treatment by the FD-TD method of the dispersive characteristics associated with electronic polarization. *Microwave and Optical Technology Letters*, 3(6):203–205, 1990. (Cited on page 8).

[19] Alexandre Vial, Anne-Sophie Grimault, Demetrio Macías, Dominique Barchiesi, and Marc Lamy de la Chapelle. Improved analytical fit of gold dispersion: Application to the modeling of extinction spectra with a finite-difference time-domain method. *Phys. Rev. B*, 71:085416, Feb 2005. (Cited on page 9).

[20] F. Hao and P. Nordlander. Efficient dielectric function for FDTD simulation of the optical properties of silver and gold nanoparticles. *Chemical Physics Letters*, 446:115–118, September 2007. (Cited on page 9).

[21] E. Gazzola, L. Brigo, G. Zacco, P. Zilio, G. Ruffato, G. Brusatin, and F. Romanato. Coupled spp modes on 1d plasmonic gratings in conical mounting. *Plasmonics*, 9(4):867–876, 2014. (Cited on page 15).

[22] Filippo Romanato, Lee Kwang Hong, Husen Kartasasmita Kang, Chee Cheong Wong, Zong Yun, and Wolfgang Knoll. Azimuthal dispersion and energy mode condensation of grating-coupled surface plasmon polaritons. *Phys. Rev. B*, 77:245435, Jun 2008. (Cited on page 15).

[23] Gustav Mie. Beiträge zur optik trüber medien, speziell kolloidaler metallösungen. *Ann. Phys.*, 330(3):377–445, 1908. (Cited on pages 16, 17, and 45).

[24] R. Gans. Evaporation-induced self-assembly of gold nanoparticles into a highly organized two-dimensional array. *Annalen der Physik*, 47:270–284, 1915. (Cited on page 16).

[25] Craig F. Bohren and Donald R. Huffman, editors. *Absorption and Scattering of Light by Small Particles*. Wiley-VCH Verlag GmbH, apr 1998. (Cited on page 17).

[26] Hitoshi Kuwata, Hiroharu Tamaru, Kunio Esumi, and Kenjiro Miyano. Resonant light scattering from metal nanoparticles: Practical analysis beyond rayleigh approximation. *Applied Physics Letters*, 83(22):4625–4627, dec 2003. (Cited on page 17).

[27] M. Meier and A. Wokaun. Enhanced fields on large metal particles: dynamic depolarization. *Optics Letters*, 8(11):581, nov 1983. (Cited on page 17).

[28] Gayatri K. Joshi, Phillip J. McClory, Barry B. Muhoberac, Amar Kumbhar, Kimberly A. Smith, and Rajesh Sardar. Designing efficient localized surface plasmon resonance-based sensing platforms: Optimization of sensor response by controlling the edge length of gold nanoprisms. *The Journal of Physical Chemistry C*, 116(39):20990–21000, sep 2012. (Cited on pages 18 and 29).

[29] Fathima S. Ameer, Shilpa Varahagiri, Donald W. Benza, Daniel R. Willett, Yimei Wen, Fenglin Wang, George Chumanov, and Jeffrey N. Anker. Tuning localized surface plasmon resonance wavelengths of silver nanoparticles by mechanical deformation. *The Journal of Physical Chemistry C*, 120(37):20886–20895, jun 2016. (Cited on page 18).

[30] Panos Patsalas, Nikolaos Kalfagiannis, and Spyros Kassavetis. Optical properties and plasmonic performance of titanium nitride. *Materials*, 8(6):3128–3154, may 2015. (Cited on page 18).

[31] Gururaj V. Naik, Vladimir M. Shalaev, and Alexandra Boltasseva. Alternative plasmonic materials: Beyond gold and silver. *Advanced Materials*, 25(24):3264–3294, may 2013. (Cited on pages 18 and 28).

[32] H. A. Bethe. Theory of diffraction by small holes. *Phys. Rev.*, 66:163–182, Oct 1944. (Cited on page 18).

[33] Evgeny Popov, Michel Nevière, Philippe Boyer, and Nicolas Bonod. Light transmission through a subwavelength hole. *Optics Communications*, 255(4-6):338–348, nov 2005. (Cited on page 19).

[34] F. J. Garcia-Vidal, T. W. Ebbesen, and L. Kuipers. Light passing through subwavelength apertures. *Rev. Mod. Phys.*, 82(1):729–787, March 2010. (Cited on page 19).

[35] Shih-Hui Chang, Stephen Gray, and George Schatz. Surface plasmon generation and light transmission by isolated nanoholes and arrays of nanoholes in thin metal films. *Opt. Express*, 13(8):3150–3165, April 2005. (Cited on page 19).

[36] H. F. Ghaemi, Tineke Thio, D. E. Grupp, T. W. Ebbesen, and H. J. Lezec. Surface plasmons enhance optical transmission through subwavelength holes. *Phys. Rev. B*, 58(11):6779–6782, September 1998. (Cited on page 19).

[37] C. Genet and T. W. Ebbesen. Light in tiny holes. *Nature*, 445(7123):39–46, jan 2007. (Cited on page 19).

[38] Hua Cao and Ajay Nahata. Influence of aperture shape on the transmission properties of a periodic array of subwavelength apertures. *Opt. Express*, 12(16):3664–3672, 2004. (Cited on page 21).

[39] A Degiron and T W Ebbesen. The role of localized surface plasmon modes in the enhanced transmission of periodic subwavelength apertures. *Journal of Optics A: Pure and Applied Optics*, 7(2):S90–S96, jan 2005. (Cited on page 21).

[40] L. Yin, V. K. Vlasko-Vlasov, A. Rydh, J. Pearson, U. Welp, S.-H. Chang, S. K. Gray, G. C. Schatz, D. B. Brown, and C. W. Kimball. Surface plasmons at single nanoholes in au films. *Applied Physics Letters*, 85(3):467–469, jul 2004. (Cited on page 21).

[41] D. De Rossi. *Sensori per misure biomediche*. Collana di ingegneria biomedica. Pàtron, 2004. (Cited on page 23).

[42] Dipti Rani, Vivek Pachauri, and Sven Ingebrandt. Silicon nanowire field-effect biosensors. In *Springer Series on Chemical Sensors and Biosensors*, pages 27–57. Springer International Publishing, 2018. (Cited on page 23).

[43] Xuan P. A. Gao, Gengfeng Zheng, and Charles M. Lieber. Subthreshold regime has the optimal sensitivity for nanowire FET biosensors. *Nano Letters*, 10(2):547–552, feb 2010. (Cited on page 23).

[44] Ricardo F. Aroca. Plasmon enhanced spectroscopy. *Phys. Chem. Chem. Phys.*, 15:5355–5363, 2013. (Cited on page 23).

[45] Heather K. Hunt and Andrea M. Armani. Label-free biological and chemical sensors. *Nanoscale*, 2(9):1544, 2010. (Cited on page 23).

[46] Bo Liedberg, Claes Nylander, and Ingemar Lunström. Surface plasmon resonance for gas detection and biosensing. *Sensors and Actuators*, 4:299–304, jan 1983. (Cited on page 24).

[47] Jirí Homola. Surface plasmon resonance sensors for detection of chemical and biological species. *Chemical Reviews*, 108, 2008. (Cited on pages 24 and 25).

[48] Jiří Homola. *Surface plasmon resonance based sensors*. Springer, Berlin New York, 2006. (Cited on page 24).

[49] www.biacore.com. *Biacore T100 Instrument Handbook*. 2005. (Cited on page 25).

[50] Hoang Nguyen, Jeho Park, Sebyung Kang, and Moonil Kim. Surface plasmon resonance: A versatile technique for biosensor applications. *Sensors*, 15(5):10481–10510, may 2015. (Cited on page 25).

[51] B. Sepúlveda, A. Calle, L. M. Lechuga, and G. Armelles. Highly sensitive detection of biomolecules with the magneto-optic surface-plasmon-resonance sensor. *Optics Letters*, 31(8):1085, apr 2006. (Cited on page 26).

[52] Bryce P. Nelson, Timothy E. Grimsrud, Mark R. Liles, Robert M. Goodman, and Robert M. Corn. Surface plasmon resonance imaging measurements of DNA and RNA hybridization adsorption onto DNA microarrays. *Analytical Chemistry*, 73(1):1–7, jan 2001. (Cited on page 26).

[53] Jennifer S. Shumaker-Parry, M. Hadi Zareie, Ruedi Aebersold, and Charles T. Campbell. Microspotting streptavidin and double-stranded DNA arrays on gold for high-throughput studies of protein-DNA interactions by surface plasmon resonance microscopy. *Analytical Chemistry*, 76(4):918–929, feb 2004. (Cited on page 26).

[54] M PILIARIK, H VAISOCHEROVA, and J HOMOLA. Towards parallelized surface plasmon resonance sensor platform for sensitive detection of oligonucleotides. *Sensors and Actuators B: Chemical*, 121(1):187–193, jan 2007. (Cited on page 26).

[55] Jakub Dostálek, Hana Vaisocherová, and Jiří Homola. Multichannel surface plasmon resonance biosensor with wavelength division multiplexing. *Sensors and Actuators B: Chemical*, 108(1-2):758–764, jul 2005. (Cited on page 26).

[56] G.G. Nenninger, P. Tobiška, J. Homola, and S.S. Yee. Long-range surface plasmons for high-resolution surface plasmon resonance sensors. *Sensors and Actuators B: Chemical*, 74(1-3):145–151, apr 2001. (Cited on page 26).

[57] Radan Slavík and Jiří Homola. Ultrahigh resolution long range surface plasmon-based sensor. *Sensors and Actuators B: Chemical*, 123(1):10–12, apr 2007. (Cited on page 26).

[58] Anna Meneghello, Agnese Antognoli, Agnese Sonato, Gabriele Zacco, Gianluca Ruffato, Erica Cretaio, and Filippo Romanato. Label-free efficient and accurate detection of cystic fibrosis causing mutations using an azimuthally rotated gc-spr platform. *Analytical Chemistry*, 86(23):11773–11781, 2014. PMID: 25359284. (Cited on page 26).

[59] Andreas B. Dahlin. Sensing applications based on plasmonic nanopores: The hole story. *Analyst*, 140:4748–4759, 2015. (Cited on page 27).

[60] Reuven Gordon, David Sinton, Karen L. Kavanagh, and Alexandre G. Brolo. A new generation of sensors based on extraordinary optical transmission. *Accounts of Chemical Research*, 41(8):1049–1057, 2008. PMID: 18605739. (Cited on page 27).

[61] Alexandre G. Brolo, Reuven Gordon, Brian Leathem, and Karen L. Kavanagh. Surface plasmon sensor based on the enhanced light transmission through arrays of nanoholes in gold films. *Langmuir*, 20(12):4813–4815, jun 2004. (Cited on page 27).

[62] Johny P. Monteiro, Leandro B. Carneiro, Mohammad M. Rahman, Alexandre G. Brolo, Marcos J.L. Santos, Jacqueline Ferreira, and Emerson M. Girotto. Effect of periodicity on the performance of surface plasmon resonance sensors based on subwavelength nanohole arrays. *Sensors and Actuators B: Chemical*, 178:366–370, mar 2013. (Cited on page 27).

[63] Arif E Cetin, Ahmet F Coskun, Betty C Galarreta, Min Huang, David Herman, Aydogan Ozcan, and Hatice Altug. Handheld high-throughput plasmonic biosensor using computational on-chip imaging. *Light: Science & Applications*, 3(1):e122–e122, jan 2014. (Cited on page 27).

[64] Jayson L. Briscoe, Sang-Yeon Cho, and Igal Brener. Part-per-trillion level detection of microcystin-LR using a periodic nanostructure. *IEEE Sensors J.*, 15(3):1366–1371, mar 2015. (Cited on page 27).

[65] Peipei Jia, Hao Jiang, Jayshri Sabarinathan, and Jun Yang. Plasmonic nanohole array sensors fabricated by template transfer with improved optical performance. *Nanotechnology*, 24(19):195501, apr 2013. (Cited on page 27).

[66] Sang-Yeon Cho, J.L. Briscoe, I.A. Hansen, J.K. Smith, Yoomi Chang, and I. Brener. Label-free plasmonic immunosensing for plasmodium in a whole blood lysate. *Sensors Journal, IEEE*, 14(5):1399–1404, May 2014. (Cited on page 27).

[67] Fatemeh Eftekhari, Carlos Escobedo, Jacqueline Ferreira, Xiaobo Duan, Emerson M. Girotto, Alexandre G. Brolo, Reuven Gordon, and David Sinton. Nanoholes as nanochannels: Flow-through plasmonic sensing. *Analytical Chemistry*, 81(11):4308–4311, jun 2009. (Cited on page 27).

[68] Ahmet Ali Yanik, Min Huang, Alp Artar, Tsung-Yao Chang, and Hatice Altug. Integrated nanoplasmonic-nanofluidic biosensors with targeted delivery of analytes. *Appl. Phys. Lett.*, 96(2):021101, 2010. (Cited on page 27).

[69] Jian Zhang, Mehrdad Irannejad, Mustafa Yavuz, and Bo Cui. Gold nanohole array with sub-1 nm roughness by annealing for sensitivity enhancement of extraordinary optical transmission biosensor. *Nanoscale Research Letters*, 10(1), may 2015. (Cited on page 27).

[70] Víctor Canalejas-Tejero, Sonia Herranz, Alyssa Bellingham, María Cruz Moreno-Bondi, and Carlos Angulo Barrios. Passivated aluminum nanohole arrays for label-free biosensing applications. *ACS Applied Materials & Interfaces*, 6(2):1005–1010, dec 2013. (Cited on page 28).

[71] Peng Zheng, Scott K. Cushing, Savan Suri, and Nianqiang Wu. Tailoring plasmonic properties of gold nanohole arrays for surface-enhanced raman scattering. *Phys. Chem. Chem. Phys.*, 17(33):21211–21219, 2015. (Cited on pages 28 and 35).

[72] Katherine A. Willets and Richard P. Van Duyne. Localized surface plasmon resonance spectroscopy and sensing. *Annual Review of Physical Chemistry*, 58(1):267–297, may 2007. (Cited on pages 28 and 30).

[73] Barbora Špačková, Piotr Wrobel, Markéta Bocková, and Jiří Homola. Optical biosensors based on plasmonic nanostructures: A review. *Proceedings of the IEEE*, 104(12):2380–2408, dec 2016. (Cited on page 29).

[74] Amanda J. Haes and Richard P. Van Duyne. A unified view of propagating and localized surface plasmon resonance biosensors. *Analytical and Bioanalytical Chemistry*, 379(7-8):920–930, jul 2004. (Cited on page 29).

[75] Tim Stakenborg and Liesbet Lagae. Gold nanoring as a sensitive plasmonic biosensor for on-chip DNA detection. *Applied Physics Letters*, 100(17):173114, apr 2012. (Cited on page 29).

[76] F. J. Rodríguez-Fortuño, M. Martínez-Marco, B. Tomás-Navarro, R. Ortuño, J. Martí, A. Martínez, and P. J. Rodríguez-Cantó. Highly-sensitive chemical detection in the infrared regime using plasmonic gold nanocrosses. *Applied Physics Letters*, 98(13):133118, mar 2011. (Cited on page 29).

[77] Srujan K. Dondapati, Tapan K. Sau, Calin Hrelescu, Thomas A. Klar, Fernando D. Stefani, and Jochen Feldmann. Label-free biosensing based on single gold nanostars as plasmonic transducers. *ACS Nano*, 4(11):6318–6322, oct 2010. (Cited on page 29).

[78] Valentina Russo, Niccolo' Michieli, Tiziana Cesca, Carlo Scian, Davide Silvestri, Margherita Morpurgo, and Giovanni Mattei. Gold–silver alloy semi-nanoshell arrays for label-free plasmonic biosensors. *Nanoscale*, 9(28):10117–10125, 2017. (Cited on page 29).

[79] Nicolò Maccaferri, Keith E. Gregorczyk, Thales V. A. G. de Oliveira, Mikko Kataja, Sebastiaan van Dijken, Zhaleh Pirzadeh, Alexandre Dmitriev, Johan Åkerman, Mato Knez, and Paolo Vavassori. Ultrasensitive and label-free molecular-level detection enabled by light phase control in magnetoplasmonic nanoantennas. *Nature Communications*, 6(1), feb 2015. (Cited on page 29).

[80] Gayatri K. Joshi, Samantha Deitz-McElyea, Merrell Johnson, Sonali Mali, Murray Korc, and Rajesh Sardar. Highly specific plasmonic biosensors for ultrasensitive MicroRNA detection in plasma from pancreatic cancer patients. *Nano Letters*, 14(12):6955–6963, nov 2014. (Cited on pages 29, 30, 102, 106, 108, and 109).

[81] Srdjan S. Aćimović, Maria A. Ortega, Vanesa Sanz, Johann Berthelot, Jose L. Garcia-Cordero, Jan Renger, Sebastian J. Maerkl, Mark P. Kreuzer, and Romain Quidant. LSPR chip for parallel, rapid, and sensitive detection of cancer markers in serum. *Nano Letters*, 14(5):2636–2641, apr 2014. (Cited on page 29).

[82] Joana Rafaela Lara Guerreiro, Maj Frederiksen, Vladimir E. Bochenkov, Victor De Freitas, Maria Goreti Ferreira Sales, and Duncan Steward Sutherland. Multifunctional biosensor based on localized surface plasmon resonance for monitoring small molecule–protein interaction. *ACS Nano*, 8(8):7958–7967, jul 2014. (Cited on page 29).

[83] Hannu Häkkinen. The gold–sulfur interface at the nanoscale. *Nature Chemistry*, 4(6):443–455, jun 2012. (Cited on page 30).

[84] Arkady A. Karyakin, Galina V. Presnova, Maya Yu. Rubtsova, and Alexey M. Egorov. Oriented immobilization of antibodies onto the gold surfaces via their native thiol groups. *Analytical Chemistry*, 72(16):3805–3811, aug 2000. (Cited on page 30).

[85] Manuela Oliverio, Sara Perotto, Gabriele C. Messina, Laura Lovato, and Francesco De Angelis. Chemical functionalization of plasmonic surface biosensors: A tutorial review on issues, strategies, and costs. *ACS Applied Materials & Interfaces*, 9(35):29394–29411, aug 2017. (Cited on pages 30 and 95).

[86] H. W. Deckman. Natural lithography. *Appl. Phys. Lett.*, 41(4):377, 1982. (Cited on page 31).

[87] J. Rybczynski, U. Ebels, and M. Giersig. Large-scale, 2D arrays of magnetic nanoparticles. *Colloids and Surfaces A: Physicochemical and Engineering Aspects*, 219(1-3):1–6, 2003. (Cited on page 32).

[88] Günter Schatz. Self-assembled nanospheres : An exciting playground. *Acta Physica Polonica A*, 115(2):431–434, 2009. (Cited on page 32).

[89] B. J. Y. Tan, C. H. Sow, T. S. Koh, K. C. Chin, A. T. S. Wee, and C. K. Ong. Fabrication of size-tunable gold nanoparticles array with nanosphere lithography, reactive ion etching, and thermal annealing. *The Journal of Physical Chemistry B*, 109(22):11100–11109, 2005. PMID: 16852354. (Cited on page 33).

[90] Stephen M. Rossnagel, William D. Westwood, and Jerome J. Cuomo. *Handbook of Plasma Processing Technology: Fundamental, Etching, Deposition and Surface Interactions (Materials Science and Process Technology)*. William Andrew, 1991. (Cited on page 34).

[91] Si Hoon Lee, Kyle C. Bantz, Nathan C. Lindquist, Sang-Hyun Oh, and Christy L. Haynes. Self-assembled plasmonic nanohole arrays. *Langmuir*, 25(23):13685–13693, dec 2009. (Cited on page 35).

[92] D. M. Mattox. *Handbook of physical vapor deposition (PVD) processing*. William Andrew Elsevier Science distributor, Norwich, N.Y. Oxford, 2010. (Cited on page 37).

[93] Per Hanarp, Duncan S Sutherland, Julie Gold, and Bengt Kasemo. Control of nanoparticle film structure for colloidal lithography. *Colloids and Surfaces A: Physicochemical and Engineering Aspects*, 214(1):23 – 36, 2003. (Cited on page 40).

[94] Stephan T. Dubas and Joseph B. Schlenoff. Factors controlling the growth of polyelectrolyte multilayers. *Macromolecules*, 32(24):8153–8160, 1999. (Cited on page 41).

[95] Christopher A. Johnson and Abraham M. Lenhoff. Adsorption of charged latex particles on mica studied by atomic force microscopy. *Journal of Colloid and Interface Science*, 179(2):587 – 599, 1996. (Cited on page 41).

[96] Zbigniew Adamczyk, Barbara Siwek, Maria Zembala, and Peter Belouschek. Kinetics of localized adsorption of colloid particles. *Advances in Colloid and Interface Science*, 48:151 – 280, 1994. (Cited on page 42).

[97] Jens Feder. Random sequential adsorption. *Journal of Theoretical Biology*, 87(2):237 – 254, 1980. (Cited on page 42).

[98] Juliane Junesch, Takumi Sannomiya, and Andreas B. Dahlin. Optical properties of nanohole arrays in metal–dielectric double films prepared by mask-on-metal colloidal lithography. *ACS Nano*, 6(11):10405–10415, oct 2012. (Cited on page 42).

[99] Christoph Langhammer, Elin M. Larsson, Vladimir P. Zhdanov, and Igor Zorić. Asymmetric hysteresis in nanoscopic single-metal hydrides: Palladium nanorings. *The Journal of Physical Chemistry C*, 116(40):21201–21207, oct 2012. (Cited on page 43).

[100] Jun Zhao, Bettina Frank, Frank Neubrech, Chunjie Zhang, Paul V. Braun, and Harald Giessen. Hole-mask colloidal nanolithography combined with tilted-angle-rotation evaporation: A versatile method for fabrication of low-cost and large-area complex plasmonic nanostructures and metamaterials. *Beilstein Journal of Nanotechnology*, 5:577–586, 2014. (Cited on page 43).

[101] Svetlana Syrenova, Carl Wadell, and Christoph Langhammer. Shrinking-hole colloidal lithography: Self-aligned nanofabrication of complex plasmonic nanoantennas. *Nano Letters*, 14(5):2655–2663, 2014. PMID: 24697350. (Cited on page 43).

[102] James A. Lock and Gérard Gouesbet. Generalized lorenzmie theory and applications. *Journal of Quantitative Spectroscopy and Radiative Transfer*, 110(11):800 – 807, 2009. Light Scattering: Mie and More Commemorating 100 years of Mie's 1908 publication. (Cited on page 45).

[103] G. Pellegrini and G. Mattei. High-performance magneto-optic surface plasmon resonance sensor design: An optimization approach. *Plasmonics*, 9(6):1457–1462, aug 2014. (Cited on page 45).

[104] Charalambos C. Katsidis and Dimitrios I. Siapkas. General transfer-matrix method for optical multilayer systems with coherent, partially coherent, and incoherent interference. *Applied Optics*, 41(19):3978, jul 2002. (Cited on page 45).

[105] Peter P. Silvester and Ronald L. Ferrari. Preface to the third edition. In *Finite elements for electrical engineers*, pages xvii–xvii. Cambridge University Press. (Cited on page 45).

[106] Björn C.P. Sturmberg, Kokou B. Dossou, Felix J. Lawrence, Christopher G. Poulton, Ross C. McPhedran, C. Martijn de Sterke, and Lindsay C. Botten. EMUstack: An open source route to insightful electromagnetic computation via the bloch mode scattering matrix method. *Computer Physics Communications*, 202:276–286, may 2016. (Cited on page 45).

[107] Kokou B. Dossou, Lindsay C. Botten, Ara A. Asatryan, Björn C. P. Sturmberg, Michael A. Byrne, Christopher G. Poulton, Ross C. McPhedran, and C. Martijn de Sterke. Modal formulation for diffraction by absorbing photonic crystal slabs. *Journal of the Optical Society of America A*, 29(5):817, apr 2012. (Cited on page 45).

[108] Niccolò Michieli, Boris Kalinic, Carlo Scian, Tiziana Cesca, and Giovanni Mattei. Optimal geometric parameters of ordered arrays of nanoprisms for enhanced sensitivity in localized plasmon based sensors. *Biosensors and Bioelectronics*, 65:346–353, mar 2015. (Cited on page 53).

[109] Andrey E. Miroshnichenko, Sergej Flach, and Yuri S. Kivshar. Fano resonances in nanoscale structures. *Rev. Mod. Phys.*, 82:2257–2298, Aug 2010. (Cited on page 72).

[110] Michaël Sarrazin, Jean-Pol Vigneron, and Jean-Marie Vigoureux. Role of wood anomalies in optical properties of thin metallic films with a bidimensional array of subwavelength holes. *Phys. Rev. B*, 67:085415, Feb 2003. (Cited on page 72).

[111] C Genet, M.P van Exter, and J.P Woerdman. Fano-type interpretation of red shifts and red tails in hole array transmission spectra. *Optics Communications*, 225(4-6):331–336, oct 2003. (Cited on page 72).

[112] Víctor H. Pérez-Luna, Michael J. O'Brien, Kimberly A. Opperman, Philip D. Hampton, Gabriel P. López, Lisa A. Klumb, and Patrick S. Stayton. Molecular recognition between genetically engineered streptavidin and surface-bound biotin. *Journal of the American Chemical Society*, 121(27):6469–6478, jul 1999. (Cited on pages 85 and 87).

[113] Linda S. Jung, Kjell E. Nelson, P. S. Stayton, and Charles T. Campbell. Binding and dissociation kinetics of wild-type and mutant streptavidins on mixed biotin-containing alkylthiolate monolayers. *Langmuir*, 16(24):9421–9432, nov 2000. (Cited on page 85).

[114] Amanda J. Haes, , and Richard P. Van Duyne. A nanoscale optical biosensor: Sensitivity and selectivity of an approach based on the localized surface plasmon resonance spectroscopy of triangular silver nanoparticles. *Journal of the American Chemical Society*, 124(35):10596–10604, 2002. PMID: 12197762. (Cited on pages 85, 86, 87, 90, 95, and 97).

[115] Carl S. Weisbecker, Margaret V. Merritt, and George M. Whitesides. Molecular self-assembly of aliphatic thiols on gold colloids. *Langmuir*, 12(16):3763–3772, jan 1996. (Cited on page 86).

[116] Yurui Xue, Xun Li, Hongbin Li, and Wenke Zhang. Quantifying thiol–gold interactions towards the efficient strength control. *Nature Communications*, 5(1), jul 2014. (Cited on page 86).

[117] C. Vericat, M. E. Vela, G. Benitez, P. Carro, and R. C. Salvarezza. Self-assembled monolayers of thiols and dithiols on gold: new challenges for a well-known system. *Chemical Society Reviews*, 39(5):1805, 2010. (Cited on page 86).

[118] *Thermo Scientific Avidi Technical Handbook*. Thermo Fisher Scientific Inc, 2009. (Cited on page 86).

[119] J. Spinke, M. Liley, F.-J. Schmitt, H.-J. Guder, L. Angermaier, and W. Knoll. Molecular recognition at self-assembled monolayers: Optimization of surface functionalization. *The Journal of Chemical Physics*, 99(9):7012–7019, nov 1993. (Cited on page 87).

[120] Anders Holmberg, Anna Blomstergren, Olof Nord, Morten Lukacs, Joakim Lundeberg, and Mathias Uhlén. The biotin-streptavidin interaction can be reversibly broken using water at elevated temperatures. *ELECTROPHORESIS*, 26(3):501–510, feb 2005. (Cited on page 87).

[121] Khin Moh Moh Aung, Xinning Ho, and Xiaodi Su. DNA assembly on streptavidin modified surface: A study using quartz crystal microbalance with dissipation or resistance measurements. *Sensors and Actuators B: Chemical*, 131(2):371–378, may 2008. (Cited on page 87).

[122] Chun lai Ren, Daniel Carvajal, Kenneth R. Shull, and Igal Szleifer. Streptavidin-biotin binding in the presence of a polymer spacer. a theoretical description. *Langmuir*, 25(20):12283–12292, oct 2009. (Cited on page 93).

[123] Mamdouh E. Abdelsalam, Philip N. Bartlett, Timothy Kelf, and Jeremy Baumberg. Wetting of regularly structured gold surfaces. *Langmuir*, 21(5):1753–1757, mar 2005. (Cited on page 94).

[124] Gregory M. Harbers, Kazunori Emoto, Charles Greef, Steven W. Metzger, Heather N. Woodward, James J. Mascali, David W. Grainger, and Michael J. Lochhead. Functionalized poly(ethylene glycol)-based bioassay surface chemistry that facilitates bioimmobilization and inhibits nonspecific protein, bacterial, and mammalian cell adhesion. *Chemistry of Materials*, 19(18):4405–4414, sep 2007. (Cited on page 94).

[125] Seongbong Jo and Kinam Park. Surface modification using silanated poly(ethylene glycol)s. *Biomaterials*, 21(6):605–616, mar 2000. (Cited on page 94).

[126] Maria Soler, M.-Carmen Estevez, Mar Alvarez, Marinus Otte, Borja Sepulveda, and Laura Lechuga. Direct detection of protein biomarkers in human fluids using site-specific antibody immobilization strategies. *Sensors*, 14(2):2239–2258, jan 2014. (Cited on page 94).

[127] Y. L. Jeyachandran, E. Mielczarski, B. Rai, and J. A. Mielczarski. Quantitative and qualitative evaluation of adsorption/desorption of bovine serum albumin on hydrophilic and hydrophobic surfaces. *Langmuir*, 25(19):11614–11620, oct 2009. (Cited on page 94).

[128] Hyungsoon Im, Antoine Lesuffleur, Nathan C. Lindquist, and Sang-Hyun Oh. Plasmonic nanoholes in a multichannel microarray format for parallel kinetic assays and differential sensing. *Analytical Chemistry*, 81(8):2854–2859, apr 2009. (Cited on page 98).

[129] David P Bartel. Microrna: Genomics, biogenesis, mechanism, and function. *Cell*, 116(2):281 – 297, 2004. (Cited on page 101).

[130] Haifeng Dong, Jianping Lei, Lin Ding, Yongqiang Wen, Huangxian Ju, and Xueji Zhang. Microrna: Function, detection, and bioanalysis. *Chemical Reviews*, 113(8):6207–6233, 2013. PMID: 23697835. (Cited on page 101).

[131] Alberto Biscontin, Silvia Casara, Stefano Cagnin, Lucia Tombolan, Angelo Rosolen, Gerolamo Lanfranchi, and Cristiano De Pittà. New miRNA labeling method for bead-based quantification. *BMC Molecular Biology*, 11(1):44, 2010. (Cited on pages 101 and 102).

[132] J. Fuchs, J.-B. Fiche, A. Buhot, R. Calemczuk, and T. Livache. Salt concentration effects on equilibrium melting curves from DNA microarrays. *Biophysical Journal*, 99(6):1886–1895, sep 2010. (Cited on page 109).